HARVARD UNIVERSITY
Graduate School of Arts and Sciences

THESIS ACCEPTANCE CERTIFICATE

The undersigned, appointed by the

Division

Department *Physics*

Committee *Robert Westervelt, Frans Spaepen,*
Efthimios Kaxiras

have examined a thesis entitled

Control and Manipulation of Magnetic Nanoparticles and Cold Atoms Using Micro-electromagnets

presented by *Chungsok Lee*

candidate for the degree of Doctor of Philosphy and hereby certify that it is worthy of acceptance.

Signature..

Typed name Robert Westervelt, Chair

Signature..

Typed name Frans Spaepen

Signature..

Typed name Efthimios Kaxiras

Date September 6, 2002

Control and Manipulation of Magnetic Nanoparticles and Cold Atoms using Micro-electromagnets

A thesis presented

by

Chungsok Lee

to
The Department of Physics
in partial fulfillment of the requirements
for the degree of
Doctor of Philosophy
In the subject of

Physics

Harvard University
Cambridge, Massachusetts
September 2002

UMI Number: 3067410

ProQuest Information and Learning Company
300 North Zeeb Road
P.O. Box 1346
Ann Arbor, MI 48106-1346

ABSTRACT

We have developed micro-electromagnets to control and manipulate both ultra cold neutral atoms in vacuum and magnetic nanoparticles in a fluid. The design and fabrication of these micro-electromagnets are described. We then demonstrate the manipulation of atoms, magnetic nanoparticles, and magnetotactic bacteria using these micro-electromagnets. This thesis consists of two main parts: atom manipulation using planar micro-electromagnet guides, and magnetic particle manipulation using various multi-layer micro-electromagnets.

We have designed, fabricated and experimentally demonstrated a micro-electromagnet to guide atoms above a substrate. Micro-electromagnet guides consist of current carrying wires microfabricated on a flat substrate to produce two-dimensional magnetic field minimum that can control the trajectories of cold neutral atoms. Micro-electromagnets can produce magnetic field magnitudes to 0.1 T with field gradients to $|\nabla B| \sim 10^4$ T/cm because high currents can be applied to microfabricated wires with current densities up to $5 \times 10^7 \mathrm{A/cm}^2$. Magnetic field calculations show that the structure of a micro-electromagnet needs to be carefully designed to optimize the loading of atoms into the micro-electromagnet. Experimental results are discussed that demonstrate the guiding of atoms. We discuss the design of new micro- and nano-electromagnets that may be used as beam splitter and interferometer for atoms.

We have also demonstrated the ability of micro-electromagnets to trap, move and assemble magnetic nanoparticles and magnetotactic bacteria in a fluid above a substrate at room temperature. Two types of micro-electromagnets, a ring trap and a matrix, have been fabricated. The ring trap is a single circular Au wire with a smooth insulating layer on top. A ring trap has been demonstrated to trap magnetic particles and magnetotactic bacteria at fixed positions. The matrix consists of two arrays of lithographically patterned Au wires, separated by an insulating layer with a smooth insulating layer on top. By controlling the currents through individual wires, the matrix can produce single or multiple peaks in the magnetic field magnitude that can be continuously moved across the surface to any position, with spatial resolution much less than the wire spacing. Using a matrix, we have trapped and moved magnetic particles and magnetotactic bacteria over the surface. We have also rotated magnetic particles above a fixed position in microscopic region utilizing time-dependent current control. Possibilities to manipulate single nanoparticles using nano-electromagnets are discussed.

ACKNOWLEDGMENTS

I have been fortunate to be around exceptional and wonderful people during my graduate studies at Harvard. I would like to take this opportunity to say thank you to all the people who have helped this work come true:

To my mentor, Prof. Robert Westervelt, for giving me the opportunity to work in his group, for giving me freedom to choose my own research directions, for always being there when the help is most needed, and for providing us the workplace that we can create, work freely and support each other. I am not hesitant to say that I have worked in the best group possible that one can imagine. To Prof. Frans Spaepen and Prof. Eric Heller for being on my committee. To Prof. Tim Kaxiras for being on my defense committee in such a short notice.

Special thanks to current group members, Brian Leroy, Ian Chan, Ania Bleszynski and Parisa Fallahi for their enthusiasm for the work, stimulating discussions, and support to make my time at Harvard enjoyable. Many thanks go to the group members, who are now alumni: Mark Topinka, David Duncan and Lester Chen for their shared experiences, useful guidance and help, and to Marija Drndic, whom I learned so much about the micro-electromagnet project and for being a great person to work with. To undergraduate students Vincent Chu and Alfreda Purdon, who devoted their summer working with us on micro-electromagnet project. I also would like to thank Kathy Aidala and Andy Vidan, who joined our group recently, for reinforcing my enthusiasm. Special thanks go to Hakho Lee who worked with me for the last few years on the micro-electromagnet experiments, for his knowledge, creativity, stimulating discussions, hard work and for being a great friend during my PhD work.

To Prof. Mara Prentiss and her student Nynke Dekker for our fruitful work together on atom guiding experiment. To Prof. Mike Tinkham and his research group members including Jeanie Lau, Dolores Bozovic, Nina Markovic, Alexey Bezryadin, Mark Bockrath and Sergio Valenzuela for making the second floor of the McKay Lab a lively and friendly place to be. To Prof. Michael Nahum and his students Joe Oswald, Philip Fisher and Joel Ullum for helping me get started in my first years at Harvard.

Special thanks to Yuan Lu for his expertise and help with scanning electron microscopes and new Raith, and to Steve Shepard for his knowledge and help with fabrication. To Nooli Jeon from Prof. Whitesides group for helpful discussions and help with taking photos with microscope. To Louis DeFeo and his machine shop people for machining many parts needed for my experiments.

To my dear family: my mom, my dad and my sister, Miyoung, who have supported me so much during both good times and hard times, for believing in me and giving me unconditional support and love. To my parents in law who I have known for a few years, always encouraging and supporting me, and for letting their lovely daughter to marry me. To my wife, Seonjin, for her love and support, whom I spent last three years of my life with. It was difficult time for both of us, and I thank you for being here with me. I am so grateful to have someone like you to share this experience.

It would have been impossible to come to this point of my life without all your help and I would like to say "Thank you".

TABLE OF CONTENTS

LIST OF FIGURES

Chapter 1

INTRODUCTION

This Thesis presents the manipulation of both cold neutral atoms in a ultra high vacuum and magnetic nanoparticles in a fluid using micro-electromagnets. The micro-electromagnets consist of current carrying wires microfabricated on the surface of a substrate. Micro-electromagnets are versatile devices that can manipulate any objects that have magnetic moment.

The Thesis consists of two main parts: atom manipulation and magnetic particle manipulation using micro-electromagnets. Although two topics are related, we present them separately because each topic has different goals: integrated atom optics to quantum computation, and nanoparticle assembly to custom-built nanostructures. Chapter 3 describes how planar micro-electromagnets are used to guide atoms above a substrate. Chapters 4, 5 and 6 describe the magnetic particle manipulation using multi-layer micro-electromagnets.

1.1. Micro-Electromagnets for Manipulation of Neutral Atoms

Our group started working on micro-electromagnets as we started collaboration with Prof. Prentiss group at Harvard in order to manipulate atoms using micron sized devices. With atoms cooled down to less than 100 μK using laser and magnetic field [Metcalf H., van der Straten P., 1994], micro-electromagnets have played an important role providing as new tools in the field of atom optics as these devices can be building blocks of integrated atom circuit elements, such as mirrors, guides, traps, lenses and interferometer for atoms [See review article in: Hinds E.A., Hughes I.G., 1999]. Using micro-electromagnets, the manipulation of atoms on a chip can be realized.

Micro-electromagnets provide flexibility and versatility to manipulate atoms on a chip, and may open possibilities ranging from integrated atom circuits to quantum dots in vacuum for quantum computation systems. Because the wavelength of an atom increases as the temperature of the atom is reduced, it may be possible to study the quantum transport of cold atoms using devices with the size comparable to the wavelength of the atoms. With contemporary fabrication techniques, micro-electromagnets can be fabricated with size approaching the wavelength of cold atoms. It has been theoretically suggested that the conductance of atoms flow through a tightly confining micro-electromagnet guide constriction can be quantized in units of λ^2/π, where λ^2 is the de Broglie wavelength of the incoming atoms [Thywissen J.H. *et al.*, 1999]. This is analogous to quantized electron flow through quantum point contacts [Van Wees B.J. *et al.*, 1988].

Magnetic field profiles produced by micro-electromagnets can be tailored to fit particular atom manipulation, and many magnetic field profiles can be created by changing wire configurations. Following devices have been experimentally demonstrated to manipulate cold atoms using current carrying wires patterned on a chip: mirrors [Drndic M. *et al.*, 1998; Johnson K.S. *et al.*, 1998; Drndic M. *et al.*, 1999; Cognet L. *et al.*, 1999], traps [Reichel J. *et al.*, 1999], guides [Dekker N.H. *et al.*, 2000; Mueller D. *et al.*, 1999], beam splitters [Denschlag J. *et al.*, 1999]. The possibility of entangling neutral atoms for quantum computation has been discussed [Drndic M. *et al.*, 2000]. Bose Einstein Condensation (BEC) of atoms has been demonstrated using a miniaturized current carrying surface trap [Hansel W. *et al.*, 2001; Ott H. *et al.*, 2001].

1.2. Micro-Electromagnets for Manipulation of Magnetic Nanoparticles

In addition to manipulating atoms, the applications of micro-electromagnets can be extended to control and manipulate magnetic nanoparticles. With the advances in nanoparticle synthesis, there has been increasing interest in developing instrumentations to manipulate these particles. For example, atomic force microscope has been demonstrated to move or drag particles around on a surface, and optical tweezers and magnetic tweezers have been used to control the location of particles in a fluid.

Until now, following methods have been experimentally employed as a way of manipulating particles. Optical tweezers have been used to trap and manipulate small particles [Ashkin A. *et al.*, 1986], bacteria [Ashkin A. and Dziedzic J.M., 1987] and cells [Ashkin A. *et al.*, 1987]. Mechanical properties of DNA attached to a magnetic microsphere have been studied using magnetic tweezers experimental setup [Haber C. and Wirtz D., 2000]. Magnetic field gradient produced by magnetic tweezers allows controlling the magnetic bead motion. DNA was studied by monitoring the motion of the bead. Scanning probe version of a magnetic manipulator has been used to trap and move magnetic beads [Barbic M. *et al*, 2001]. Manipulation of micron sized magnetic particles is performed by integrating a microcoil to a soft ferromagnetic microtip. The tip produces the magnetic field gradient and magnetic particles follow the motion of the tip.

It would be a challenge, but at the same time a great achievement to be able to assemble nanoparticles in any structure we wish, and to construct custom-designed structures from these particles. The manipulation of nanoparticles is not limited only to magnetic particles, but can be extended to many other interesting particles by chemically attaching magnetic particles to objects like semiconductor crystals or nanotubes. The ability to manipulate magnetic particles can be also important in biological and biomedical applications, for example to separate, manipulate and study cells and DNA that are attached to magnetic particles, in micron or nanometer range. Controlled experiments with biological systems including cells, microorganisms, DNA and proteins can be carried out by inserting or attaching magnetic particles to those entities. Furthermore, the whole experiments can be automated and miniaturized, realizing "micro-Total Analysis systems"(μ-TAS) on a single chip [*Micro Total Analysis Systems*, 1994 & 1998]. With these goals in mind, we have developed micro-electromagnets as a novel way of micro-manipulating magnetic nanoparticles.

Micro-electromagnets have advantages to be used in assembly of nanoparticles and manipulation of biological samples: (1) Dynamic magnetic field profiles can be created by changing the current distributions on the wires. (2) Magnetic field peaks can be generated and individually moved continuously over the surface with spatial resolution much less than the wire spacing. (3) Two or more magnetic field peaks can be generated simultaneously and can be moved independently. (4) Micro-electromagnets are integrated devices on a chip, where optical tweezers [Ashkin A. *et al.*, 1986] and magnetic tweezers [Haber C. and Wirtz D., 2000] require sophisticated and massive setup to operate. These features will be discussed in more detail later in Chapter 4.

1.3. Overview of The Thesis

Chapter 2 describes the fabrication procedure, thermal and electrical properties, and magnetic field profiles of micro-electromagnets that are used in the manipulation of both cold neutral atoms and magnetic nanoparticles. Both planar and multi-layer micro-electromagnets are presented, which include micro-electromagnet guides for atoms, a ring trap and a matrix for magnetic particles. The section on fabrication illustrates different techniques for constructing devices: planar structures for atom manipulation vs. multi-layer structures with insulating layers for magnetic particle manipulation, optical lithography and electroplating technique for structures with wire size bigger than 1 μm vs. electron-beam lithography for structures with wire size smaller than 1 μm. The maximum allowable current on a micro-fabricated wire is discussed.

Chapter 3 presents the manipulation of cold neutral atoms using micro-electromagnet guides. The physical principles behind the neutral atom manipulation using micro-electromagnets are presented first. We describe many types of micro-electromagnet guides, and illustrate how to design a micro-electromagnet to optimize the guiding of atoms. Experimental setup and methods to guide atoms using a micro-electromagnet are described. The experimental results are presented that demonstrated the guiding of atoms. We propose a new nano-electromagnet beam splitter/interferometer for atoms by utilizing time-dependent feature of the device.

Chapter 4 presents multi-layer micro-electromagnets that position and move magnetic nanoparticles in a fluid above a substrate at room temperature. Three types of micro-electromagnets, a ring trap, an array of traps, and a matrix, are introduced and experimentally demonstrated to manipulate magnetic particles. The operating principle and magnetic field profiles of each micro-electromagnet are described in detail.

Chapter 5 presents how multi-layer micro-electromagnets can be used to control and manipulate biological organisms. As an example, experimental demonstration is shown to trap and move magnetotactic bacteria using micro-electromagnets that are presented in Chapter 4. The versatility of micro-electromagnets comes from the fact that they can manipulate magnetically tagged objects without physical barriers or channels. The ability to move magnetic particles may lead to a new technology to manipulate and control biological systems. Controlled experiments with biological systems including cells, microorganisms, DNA and proteins can be carried out by inserting or attaching magnetic particles to those entities.

Chapter 6 describes the experiments to manipulate single Co nanoparticles using nano-electromagnets. This work is currently ongoing in collaborative efforts between our group and Prof. Bawendi's group in MIT. We describe three aspects of the proposed experiment: magnetic nanoparticles, nano-electromagnets, and experimental setup.

Finally, chapter 7 concludes the Thesis with a synopsis of the key results. We discuss the potential future experiments.

Chapter 2

FABRICATION, PROPERTIES AND MAGNETIC FIELD PROFILES OF MICRO-ELECTROMAGNETS

This chapter describes the fabrication, thermal and electrical properties, and the magnetic field profiles of micro-electromagnets. The micro-electromagnets control and manipulate both cold neutral atoms in ultra high vacuum and magnetic nanoparticles on a chip at room temperature. Micro-electromagnets consist of single or multiple layer(s) of lithographically patterned current carrying Au wires with set of insulating layers that separate these wires.

Micro-electromagnets are fabricated using two different methods depending on the smallest wire size. Optical lithography followed by electroplating is performed to fabricate wire size larger than few microns, and electron-beam (e-beam) lithography, without an electroplating step, is used to fabricate wire size smaller than a micron. Both single and multi-layer micro-electromagnets were fabricated. Single layer micro-electromagnets have been used to manipulate cold neutral atoms in vacuum, and multi-layer micro-electromagnets have been used to control the location of magnetic nanoparticles in fluids at room temperature. Current densities up to 10^8 A/cm^2 were achieved with micro-electromagnets, which produce high magnetic fields to $B \sim 0.1$ T with high field gradients to $|\nabla B| \sim 10^5$ T/m [Drndic M. *et al.*, 1998]. We have experimentally investigated Au, Cu and Ag wires on sapphire and silicon substrates and

Nb wires on silicon substrates. The best results were obtained with Au, for which we achieved the highest current densities [Drndic M. PhD Thesis, 2000].

In this Chapter, we describe the properties and fabrication procedures of micro-electromagnets that are used to control and manipulate cold neutral atoms (section 2.1) and magnetic nanoparticles (section 2.2) fabricated using optical lithography technique. We then discuss the properties and fabrication procedures of nano-electromagnets for the manipulation of cold neutral atoms (section 2.3) and magnetic nanoparticles (section 2.4) fabricated using electron-beam lithography. Section 2.5 discusses the maximum current capacity that can be permitted on the wires we have fabricated.

2.1. Micro-Electromagnets for Cold Neutral Atoms

Micro-electromagnets for the purpose of manipulating neutral atoms were fabricated on either sapphire or silicon substrates using optical lithography and electroplating. Wire size of micro-electromagnets designed and constructed range from wire width $w = 3$ μm up to $w = 100$ μm, depending on the applications and the experiments: traps ($w = 3$ μm), mirrors ($w = 3, 10, 50$ μm), guides ($w = 50, 100$ μm), and three-dimensional (3D) micro-electromagnets ($w = 10$ μm). The choice of substrates is important because micro-electromagnets heat up during operation. Efficient heat removal through the substrates is critical to prevent device failure. Sapphire is chosen for its high thermal conductivity and electrically low conducting properties. The transparency of sapphire is also useful as laser beam can pass through the substrate to probe and detect the atoms.

Typical fabrication process for the micro-electromagnets is illustrated in Fig. 2.1. Micro-electromagnets are fabricated in the cleanroom on the second floor of Gordon McKay building. The detailed fabrication recipe is as follows:

(1) Prior to fabrication, sapphire substrates are ultrasonically cleaned in TCE (Trichloroethylene), acetone and methanol for 10 minutes each.

(2) Substrates are blown dry with nitrogen gas and placed on a hot plate at temperature of 105 °C for 10 minutes to dry off residual solvents.

(3) Primer and photoresist are spun on the substrate consecutively for 30 s at 5000 rpm (revolution per minute). A primer is spun on first as it enhances the adhesion of the photoresist on substrates. Type 1813 photoresist is used, which gives about 1 μm thickness at 5000 rpm.

(4) The substrate is placed on a hot plate at temperature of 105 °C for 3 1/2 minutes to dry off solvents and to thermally link the resist.

(5) The substrate is then exposed to UV for 6 s using Karl Suss mask aligner through a laser patterned hard mask[1]. The patterns are drawn using Freehand software and sent to a company called Advance Reproductions, where the patterns are generated on a 3 by 3 inches glass mask with chrome on one side.

(6) The substrate is placed in a developer (351 developer for 1800 series photoresist) for 60 s and rinsed with running water for about 15 s.

(7) Each substrate is carefully checked under optical microscope for defects.

(8) Cleanly developed substrates are evaporated with metals. For metal evaporation, Cr and Au are deposited using a new thermal evaporator on the

---

[1] The pattern on the mask is drawn using one of the drawing softwares in our lab and sent to the company called "Advance reproductions", 100 Flagship Drive, North Andover, MA 01845. Tel. 978-685-2911. The smallest size of the line that can be generated is 3 microns.

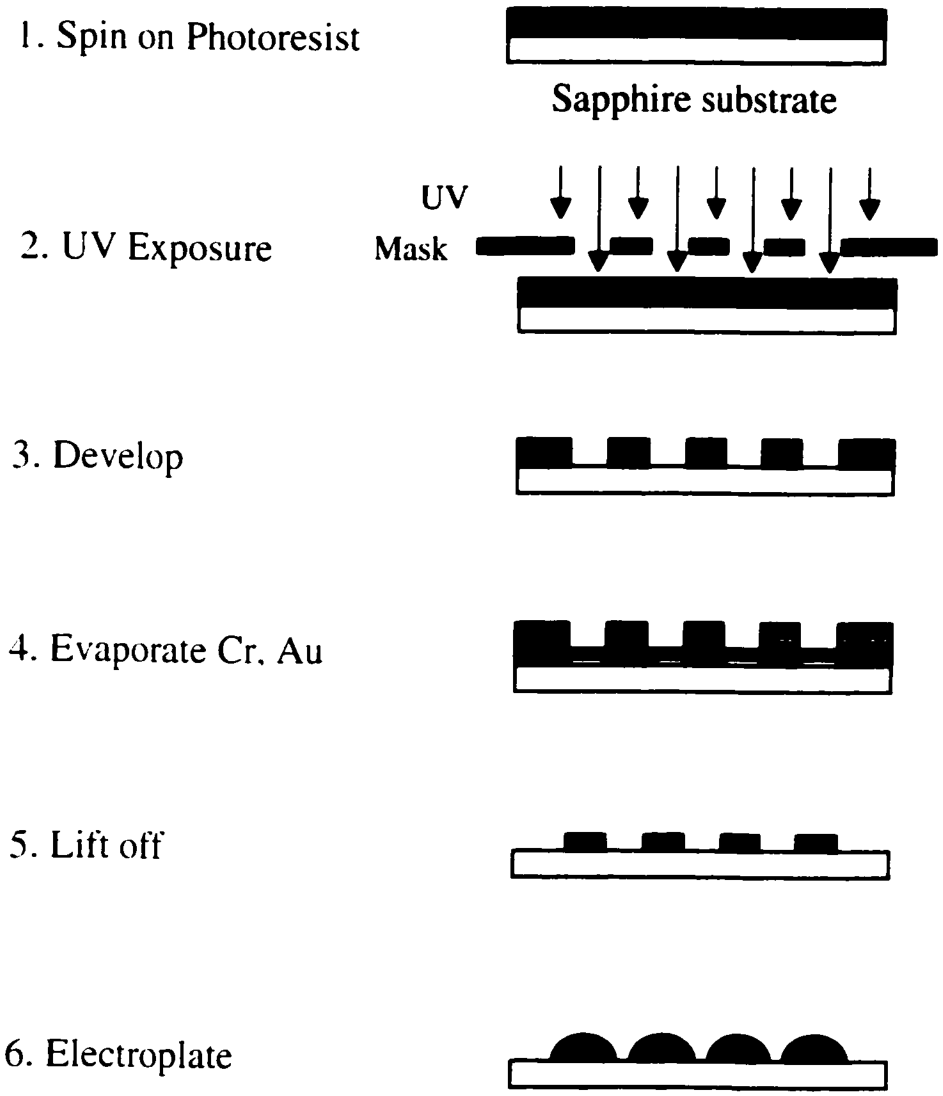

Figure 2.1. Schematic diagrams of fabrication process: three main steps are optical lithography, metal evaporation and electroplating.

2nd floor in McKay. With the evaporator chamber pumped down to the vacuum of 2 x 10^{-7} Torr, 50 Å of Cr is first deposited at a rate of 1 Å /s as an adhesion layer. A layer of Au is then evaporated for thickness of 800 Å at a rate of 3 Å /s.

(9) After metal evaporation, the substrate is placed in acetone for a few hours to lift off the photoresist. Au is lifted off in few hours in most cases, but it could take an overnight sometimes. If they don't lift off easily, slight sonication can help the lift off process.

Evaporated Au wires have small cross sectional area and resistances in the kΩ range. In order to reduce the resistance of each wire and to thicken the cross sectional area, Au wires are electroplated in Au plating solution. Electroplating is done under the fume hood in the sample preparation room (Room 213) in our group. The detailed recipe for electroplating is as follows:

(1) Au wires are connected to Cu leads through In contacts; thin In wires are cut into small pieces and they are made in contact with wires under optical microscope. Cu leads are then connected to the In contacts and the connection between Au wires and Cu leads are made.

(2) The Au wires, connected as cathode, are immersed into the Au plating solution, which is a pH ≈ 7, sulfite bath (TG 25E) commercially available from *Technic Inc*[2]. The bath contains ~3% $Na_3Au(SO_3)_2$, ~8% Na_2SO_3, and the solution is heated to 60 °C in a beaker on a hot plate. Prior to electroplating, Au plating solution needs to be filtered through fine filters with

---

[2] Technic Gold 25E (ready to use) with 1/4 ounce of Au per quart of solution. Technic Inc., Providence, RI 02940. Tel. 401-781-6100. Other gold solutions are available such as the neutral immersion 24Kt Au bath (Oromerse Br) for electroless plating of Ag, Cu, Ni, Fe, Pb, solder, brass, etc.

pore sizes less than 1 μm to block any particles and to ensure good quality of the plating solution. Au wires are connected to the negative terminal (cathode) and the plating solution is connected to the positive terminal (anode) of the current supply. To obtain smooth surfaces, plating is done at low currents (~ 0.1 mA) with stirring of the solution using a magnetic bar. The anode is a thin Pt foil (high purity, available from *Alfa Aesar*[3]) with area 1 x 1 cm^2.

Figure 2.2 shows the micrographs of a micro-electromagnet atom guide, which is designed to guide cold neutral atoms from one position to another. It consists of lithographically patterned four current carrying wires fabricated on a sapphire substrate. The micrograph of whole device is shown in Fig. 2.2(a). Although the device has 1.6 cm x 1 cm area, including eight pads where Cu leads are connected, actual atom guiding area is only few hundred square microns as it will be shown in the calculation later. Initially patterned wires are connected as it can be seen on the top corners in Fig. 2.2(a). This enables us to connect only one Cu lead through the device when electroplating, which allows uniform plating of Au over all the wires because uniform current is supplied through all the wires. After electroplating, the connected regions are scratched off so that each wire can be connected to individual current supply.

Figure 2.2(b) shows the central region of the device after Au evaporation. After evaporation, the resistance of each wire is $R \cong 128\ \Omega$, and each wire has width $w = 100\ \mu m$ and height $h = 80$ nm. The center-to-center spacing between adjacent wires

---

[3] AlfaAesar, Ward Hill, MA 01835, Tel. 800-343-0660. http://www.alfa.com.

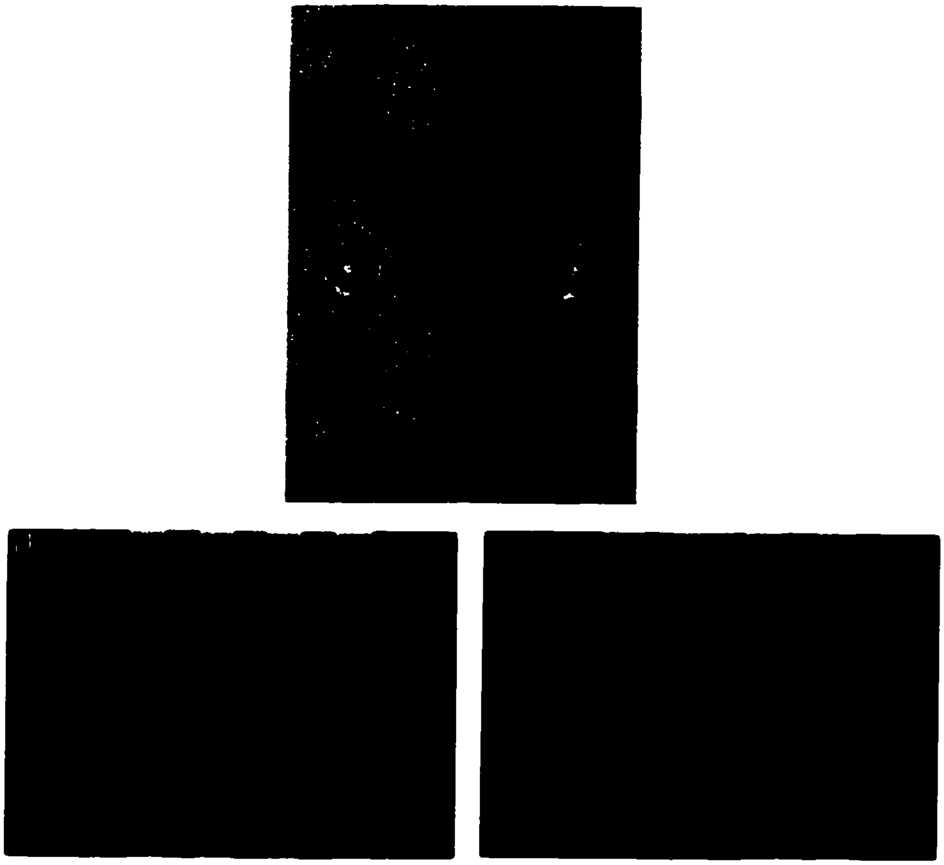

Figure 2.2. (a) A micrograph of a micro-electromagnet guide after Au evaporation. (b) Close up of the device shown in (a) after Au evaporation. Each wire has width of 100 μm, height of 80 nm and the resistance of 128 Ω. (c) Close up of the device shown in (a) after electroplating in Au solution. Wires have grown and each wire now has width of 120 μm, height of 10 μm and the resistance of 1 Ω. The device is designed to move cold neutral atoms from one position to another. It consists of lithographically patterned four current carrying wires fabricated on a sapphire substrate.

is 200 μm. After electroplating for a few hours, both width and height of the wires are increased as shown in Fig. 2.2(c). Each wire then has width w = 120 μm and height h = 10 μm, and the resistance of each wire goes down to $R \cong 1\ \Omega$. The measured value of resistance agrees very well with the calculated resistance $R = \rho l/wh$, where ρ is the electrical resistivity of Au and l is the length of a wire. This hundred-fold decrease in wire resistance allows high current to pass through the wires without generating much heat.

The durability and current capacity for the wires shown in Fig.2.2(c) were tested at temperature T = 120 K by pulsing a current through each wire. The resistance of each wire goes down to $R \cong 0.5\ \Omega$ at T=120 K. The I-V graph shown in Fig. 2.3 is an actual data where current was pulsed for a duty cycle of 140 ms for every 4 s in constant current mode for more than 10 min. Current was slowly ramped up and current I = 10.5 A was achieved without failure of the wire. We stopped ramping up the current at this point as slight heating of the wire was observed, which was indicated by the increase in wire resistance. Resistance increase shown in graph indicates the temperature increase on a wire. Temperature rise on a wire can be estimated using a relation, $R = R_0[1+\alpha(T-T_0)]$, where R, T and R_0, T_0 are final and initial resistance and temperature respectively, and α is temperature coefficient. For Au, $\alpha = 3.4\times10^{-3}$ °C^{-1}. The wire temperature goes from 120 K to 135 K during this short purse for the current amount of 10.5 A.

Other micro-electromagnets also have been designed, fabricated and experimented, which included mirrors, focusing mirrors and traps for atoms. The fabrication process is essentially the same for all the planar micro-electromagnets we have constructed in our group.

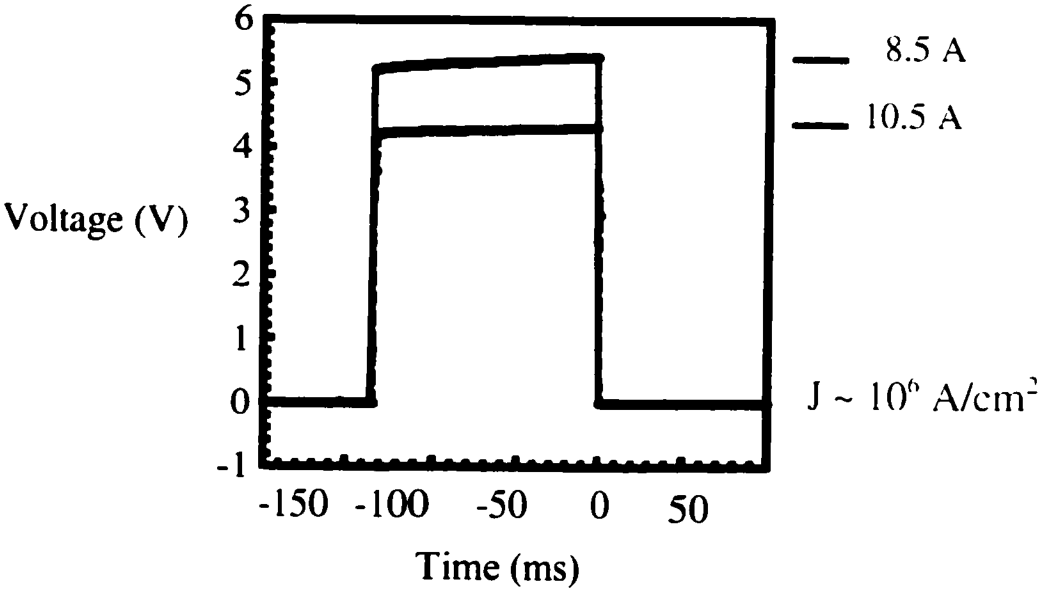

Figure 2.3. I-V graph of a wire for a micro-electromagnet shown in Fig. 2.2. The current was pulsed for a duty cycle of 140 ms for every 4 s in constant current mode for more than 10 min. Current was slowly ramped up and current I = 10.5 A was achieved without failure of the wire. Slight heating of the wire is observed, which is indicated by the increase in wire resistance. The wire temperature goes from 120 K to 135 K during this short purse for the current amount of 10.5 A.

2.2. Multi-layer Micro-Electromagnets for the Control and Manipulation of Magnetic Nanoparticles

In this section, we describe the fabrication and properties of multi-layer micro-electromagnets we have developed for the control and manipulation of magnetic nanoparticles. We have demonstrated three micro-electromagnets for the purpose of manipulating magnetic nanoparticles. These micro-electromagnets are shown in Fig. 2.4 as well as the calculated magnetic field profiles for each device. A ring trap shown in Fig. 2.4(a) consists of a single circular pattern conductor with an insulating layer spun on top. It has wire width $w = 10\ \mu m$, wire height $h = 3\ \mu m$, radius $r = 35\ \mu m$ and thickness of an insulating layer $t = 30\ \mu m$. A ring trap produces maximum magnetic field peak in the center of the circular pattern wire on the surface of an insulator plane. The magnetic field peak is calculated and shown in Fig 2.4(b)

Figure 2.4(c) shows a micro-electromagnet matrix, which is designed to trap and move magnetic nanoparticles. The matrix consists of two layers of current-carrying Au wires, separated by an insulating layer, with an additional layer spun on top. For the matrix shown in Fig. 2.4(c), each wire has width $w = 10\ \mu m$, height $h = 3\ \mu m$ and resistance $R = 10\ \Omega$. The center-to center spacing between adjacent wires is 20 μm. Many magnetic field profiles can be created using this device by changing the current distributions in the wires because each wire is connected to individual current supply. For the demonstrations to follow in Chapter 4, a matrix consisting of 7x7 wires was used for particle manipulation. We have used 14 home-built bipolar current supplies to power the device, with each wire connected to a current supply. Amount of current through

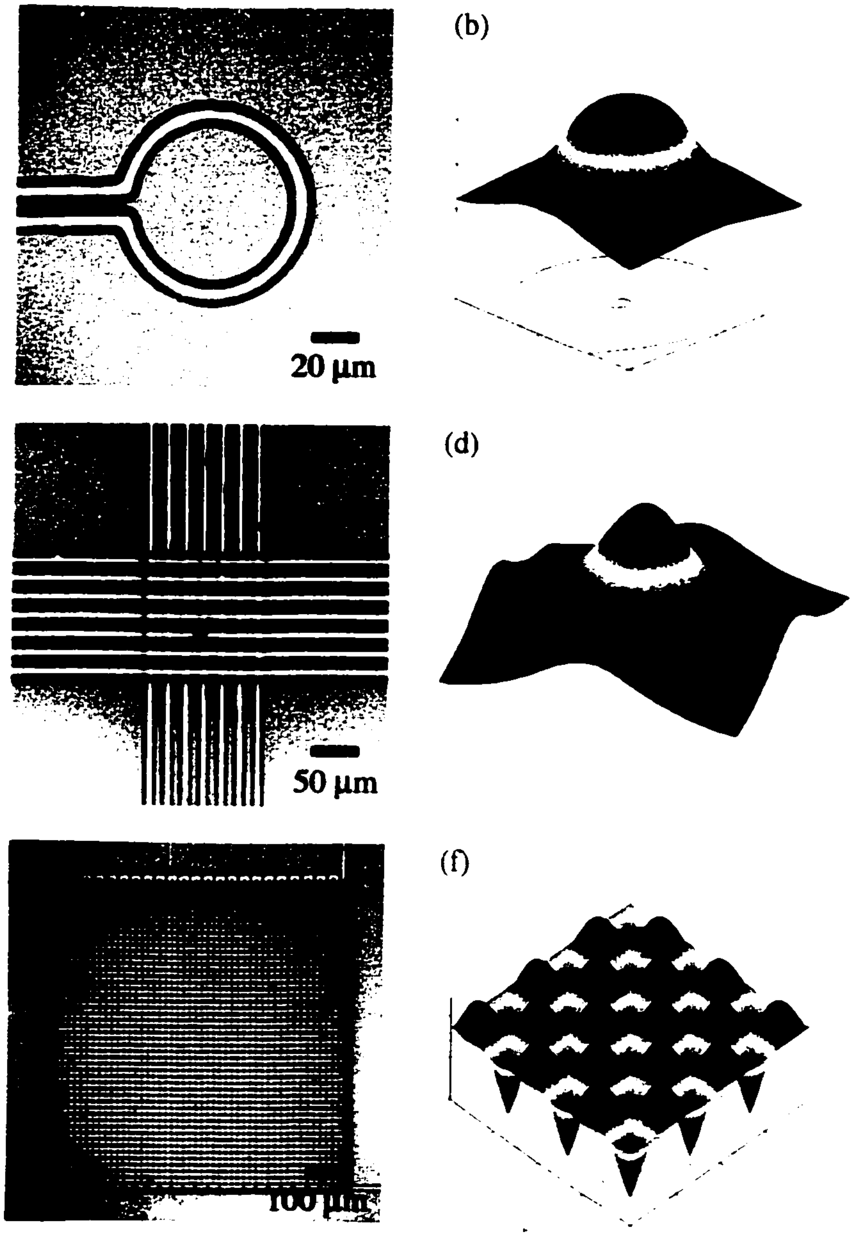

Figure 2.4. (a) Micrograph of a fabricated ring trap. A wire has a width of 10 μm, height of 3 μm. (b) Computed magnetic field magnitude for the ring trap shown in (a). (c) Micrograph of a fabricated matrix (7x7 wires). The matrix consists of two layers of current carrying conductors with two layers of insulators. Each wire has width of 10 μm, height of 3 μm, and center-to-center spacing between wires is 20 μm. (d) Computed magnetic field profile with 2x2 wires. (e) Micrograph of a micro-electromagnet, which produces an array of periodic magnetic field peaks. It consists of two serpentine pattern wires stacked up perpendicular to each other separated by an insulating layer with another insulating layer on top. Each wire has width of 10 μm, height of 3 μm, and center-to-center spacing between wires is 20 μm. (f) Computed magnetic field profile produced by the device for $i_1 = i_2 = 0.1$ A. $B_{max} = 20$ G with $\nabla B = 1$ G/μm is produced.

each wire is controlled by a computer, as the amount of output current is linearly proportional to the voltage outputted by the computer. The magnetic field peak shown in Fig. 2.4(d) was calculated using a 2x2 matrix.

A micro-electromagnet shown in Fig. 2.4(e) has similar structure as the matrix. It consists of two sets of current carrying serpentine pattern wires separated by an insulating layer with another insulating layer on top. However, unlike the matrix, all the wires are connected and the same amount of current flows through all the wires. A single layer of serpentine pattern wires was investigated earlier by [Zabow G. *et al.*, 1999]. It produces magnetic field magnitude that decays exponentially away from the surface, but sinusoidally across it. Using this property, this device, which is commonly referred as an atom mirror, was used to deflect [Drndic M. *et al.*, 1998; Johnson K.S. *et al.*, 1998] and reflect ultra cold atoms [Drndic M. *et al.*, 1999; Cognet L. *et al.*, 1999]. When two of these serpentine pattern wires are stacked up perpendicularly as shown in Fig. 2.4(e), it produces magnetic field pattern that has array of pockets near the surface as shown in Fig. 2.4(f). The magnitude of magnetic fields produced by the device near the surface can be expressed as

$$|B| \propto 1 + Sin(\frac{\pi x}{a}) \cdot Sin(\frac{\pi y}{a}),$$

where a is the center-to-center spacing between adjacent wires. As a result, series of successive maxima and minima of magnetic field magnitudes are produced on a two-dimensional surface, with the spacing between two nearest maxima (or minima) of $\sqrt{2}a$.

The fabrication steps to make multi-layer micro-electromagnets is essentially the same as described in section 2.1, where lithographically defined patterns were constructed as a first layer of wires on sapphire substrates. In this section, we describe multi-layer micro-electromagnets that have been fabricated using optical lithography. Devices can be patterned using either optical or e-beam lithography; example will be described in the next section. Fabrication process of multi-layer micro-electromagnets involves applying a thin layer of insulating layer between wires and another insulating layer on top.

Polyimides were used as insulating layers. Polyimides exhibit an exceptional combination of thermal stability (> 500 °C), mechanical toughness and chemical resistance. They also provide an excellent planarization of the underlying surface. Polyimides have[4] thermal conductivity ~ 4 x 10^{-5} cal/(cm s °C), specific heat 0.6 cal/(g °C), electrical resistivity > 10^{16} Ωcm, refractive index 1.7, and dielectric breakdown field > 2 x 10^{4} V/cm. Different kinds of polyimides are commercially available[4]. We used both regular and photosensitive polyimides as insulating layers.

For a ring trap shown in Fig. 2.4(a), regular polyimide type PI 2556 from HD Microsystems was used. For multi-layer structures shown in Figs. 2.4(c) and 2.4(e), photosensitive polyimide type PI 2729 was used because parts of the insulating layer had to be patterned. Photosensitive polyimides can be easily patterned by conventional optical lithography and they are frequently used when the insulating layers need to be patterned. The PI 2729 polyimide gives optimal thickness range for the devices shown in Figs. 2.4(c) and 2.4(e). Using different kinds of polyimides, its thickness can range from 1 μm up to tens of μm.

---

[4] Available from HD Microsystems (enterprise of Dupont Electronics and Hitachi Chemical), Wilmington, DE 19880. Tel. 800-346-5656. http://www.hdmicrosystems.com.

Schematic diagrams of fabrication process for micro-electromagnets are shown in Fig. 2.5 and detailed recipe is described in following. For a ring trap:

(1) As before, first layer of current carrying wire patterns are defined using optical lithography, where a thin layer of photoresist is spun on and exposed to UV.

(2) A layer of Au conductor is evaporated and electroplated as described in section 2.1.

(3) We then spin on regular polyimide PI 2556 for 5 s at 500 rpm followed by 30 s at 4000 rpm.

(4) The substrate is thermally cured on a hot plate for following duration: 120 °C for 30 min, then ramp up to final temperature of 260 °C at 2 °C/min, keep at 260 °C for 60 min, then ramp down to 20 °C at 2 °C/min. It can be also cured inside convectional oven, but higher final temperature is needed. Thermal curing removes any residual solvents and completes the adhesion process. Final thickness of insulating layer after thermal curing is about 30 μm.

(5) Once polyimide layer is thermally cured, Cu leads are attached in the same way that was described in section 2.1.

For micro-electromagnets with multi-layers of conductors as shown in Figs. 2.4(c) and 2.4(e), both photosensitive polyimide PI 2729 and regular polyimide were used as insulating layers because the first layer of insulator needed to be patterned. The recipe for fabricating multi-layer micro-electromagnets is as follows.

(1) After a first layer of Au conductor is patterned and evaporated, photosensitive polyimide is spun on for 5 s at 500 rpm followed by 30 s at 5000 rpm.

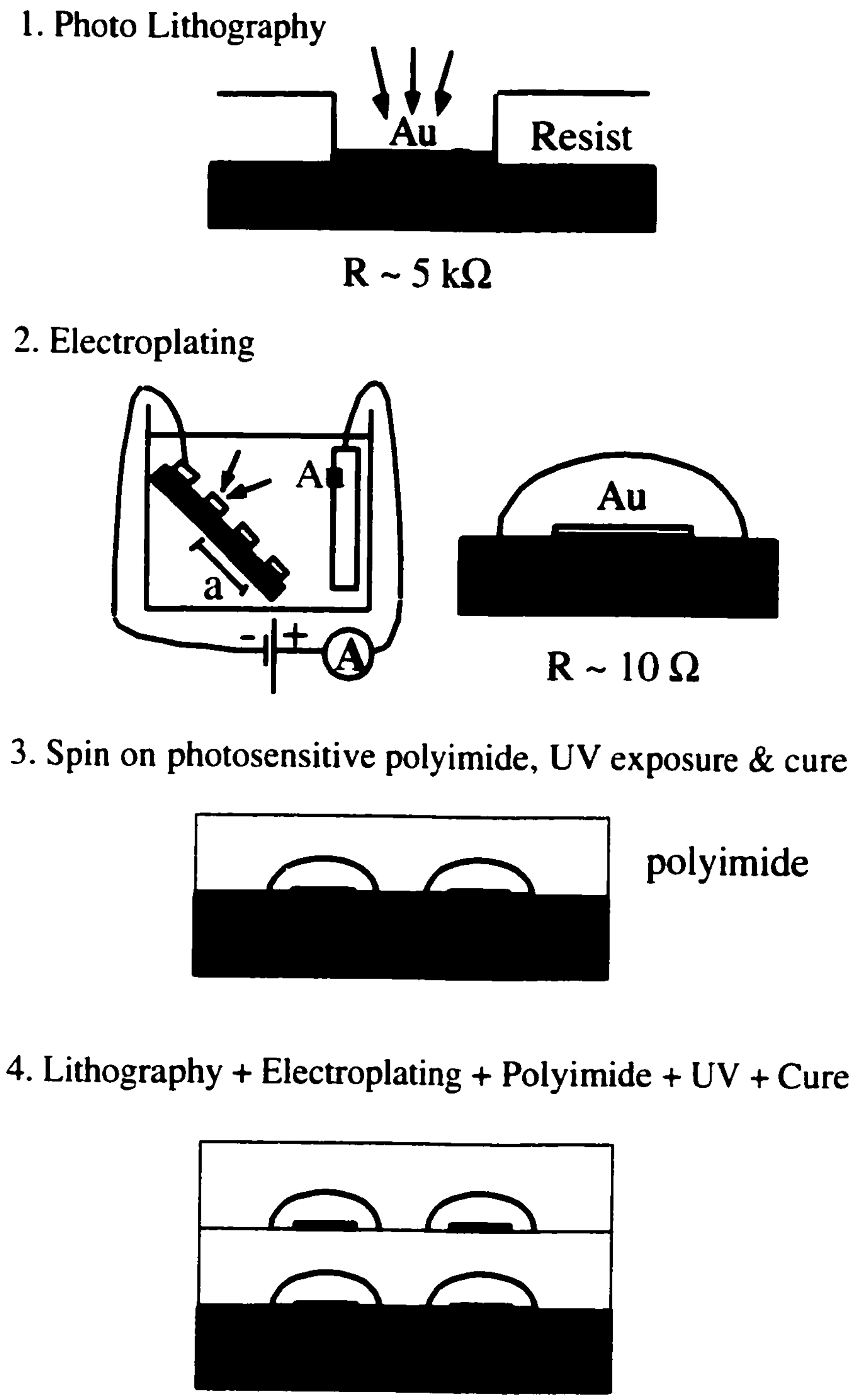

Figure 2.5. Schematic diagrams of fabrication process for multi-layer micro-electromagnets.

(2) The substrate is soft baked for 3.5 min at 100 °C to dry off remaining solvents and to thermally link the polymer.

(3) The substrate is exposed to UV light for 40 s through a photomask, then developed for 40 s and rinsed for 20 s in commercially available solutions DE 6180 and RI 9180 respectively. Photosensitive polyimides are negative resists meaning exposed areas remain on the surface while unexposed areas gets removed. Therefore, photomask must be designed in opposite way: region to be patterned are dark. Photoresist 1813 used in our fabrication was positive resist: region to be patterned are transparent.

(4) After developed, the substrate is thermally cured on a hot plate for the same duration as regular polyimide described above.

(5) Repeat lithography and electroplating steps to make a second layer of wires on top of this insulating layer. During lithography process, the second layer wire pattern needs to be perpendicularly aligned to the first layer of conductor. Using a Karl Suss mask aligner, the location of photomask is adjusted over a substrate and precise alignment to ~ 10 μm can be possible.

(6) After electroplating the second layer of wires, a thin layer of smooth regular polyimide is spun on and thermally cured, and the fabrication procedure is completed.

2.3. Nano-Electromagnet Guide/Interferometer for Cold Neutral Atoms

In this section, we report the fabrication procedure and properties of sub-micron sized nano-electromagnets fabricated on silicon substrates. We have designed and fabricated sub-micron sized micro-electromagnets for the purpose of manipulating ultra cold atoms. We have used the new Raith 150 (e-beam writer) located in the cleanroom in the basement of Gordon McKay for patterning small wire geometries. We used silicon wafers as substrates to pattern small devices because electrons charged up sapphire substrates when doing e-beam lithography, which made it difficult to focus electron beam on a substrate. It turns out evaporated metals stick much better on the surface of silicon substrates than on sapphire substrates. We had no problem applying continuous currents with current density up to 4.5 x 10^7 A/cm^2 at room temperature without device failure. We have also fabricated devices on sapphire substrates by applying a sacrificial layer (50 nm Cr) on top of PMMA layer to reduce the electron charging effect. Devices fabricated in this way involved more fabrication steps with smaller success rates; hence they were not investigated further.

The fabrication procedure to write patterns using e-beam lithography technique is similar to that of optical lithography. The detailed recipe is as follows:

(1) Substrates were prepared by cutting a 4" silicon wafer into small pieces using a diamond tip cutter. Silicon wafers used were circular with 4" diameter,

500 μm thick. They were p-type with boron and coated with 300 nm thick SiO_2 layer on top to prevent electrical shorting between patterned conductors[5].

(2) Substrates are ultrasonically cleaned in TCE, acetone and methanol for 10 min each. They are blown dry and baked at 100 °C on a hot plate for 10 min to completely dry off solvents.

(3) Three layers of polymethyl methacrylate (PMMA) are spun on subsequently followed by soft bake in following sequences. First, 495 PMMA 2% in Anisole is spun on for 40 s at 3000 rpm. The substrate is placed on a hot plate at temperature of 180 °C for 2 min. Second layer of 495 PMMA 2% in Anisole is spun on for 40 s at 3000 rpm to thicken the resist layer. The substrate is again placed on a hot plate (180 °C) for 2 min. We then spin on 950 PMMA 2% in Anisole for 40 s at 3000 rpm followed by final soft bake at 180 °C for 2 min. Expected final thickness of PMMA layers is ~ 150 nm.

(4) The substrate is loaded into Raith 150 and patterns are written. The complete procedure for writing patterns using Raith is described in Appendix A.1.

(5) The substrate is placed in PMMA developer for 90 s and rinsed with IPA (Isopropanyl) for 20 s.

(6) Using a new thermal evaporator (from Sharon vacuum) in cleanroom in the basement, 5 nm of Cr followed by 50 ~ 150 nm of Au are evaporated. The procedure for using new evaporator is illustrated in Appendix A.2.

(7) After metal evaporation, the substrate is placed in acetone for a few hours to lift off the unwanted parts of Au from the surface.

---

[5] Si wafers are 4" <100> p-type, 15 – 30 cmΩ, 457 ~ 559 μm thick, prime grade with 300 nm thick SiO_2 layer on top. They were purchased from NOVA electronic materials inc. 2833 Trinity Square Drive, Suite #173, Carrollton, TX 75006. Tel. 972-664-0550. http://www.novawafers.com

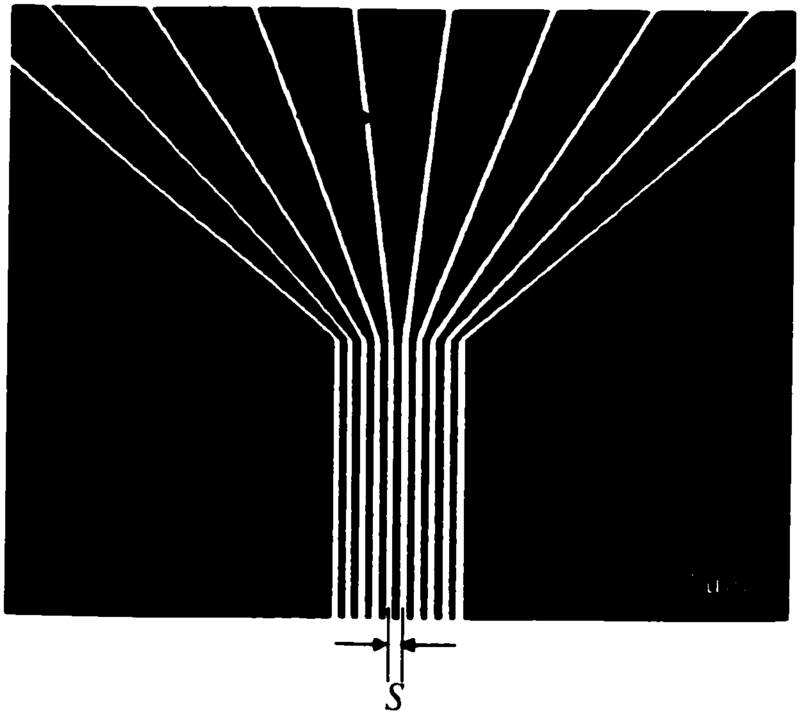

Figure 2.6. SEM image of an atom guide/interferometer. It consists of ten equally spaced wires, where each wire has a width of 200 nm and a height of 80 nm. The center-to-center spacing between two adjacent wires, denoted by *S*, is 400 nm.

Figure 2.6 shows an SEM image of an atom guide/interferometer fabricated using procedure described above. It consists of ten equally spaced wires fabricated on a Si/SiO$_2$ substrate, where each wire has wire width $w = 200$ nm and wire height $h = 80$ nm, which gives wire resistance per unit length $R/l = 1.4$ Ω/μm. The center-to-center spacing between adjacent wires is $S = 400$ nm. This device can work in many modes: single channel guide, multi channel guides and an interferometer or a beam splitter for atoms.

Figure 2.7 shows contour plots of magnetic field magnitude that can be produced by the device shown in Fig. 2.6. Single channel guide can be created when currents are applied to any combination of three or four wires. For example, when currents are applied in alternate directions to four adjacent wires, a region with field magnitude zero is created above the surface along the wires, where the contour plot of field magnitude is shown in Fig. 2.7(a). Atoms in weak field seeking states are guided by this two-dimensional minimum and transported from one end of wires to the other end. Multi-channel guides can be created using this device by applying currents through nine wires as shown in Fig. 2.7(b). The location and depth of these channels can be controlled precisely by adjusting the current distribution.

More interestingly, by applying time-dependent current through the wires, it is possible to create interferometers or beam splitters for atoms. Three field plots are shown in Fig. 2.7(c) to illustrate how this works. Single magnetic field minimum created initially is split into two magnetic fields minima by varying the currents on the wires. Therefore, atoms that travel along a single minimum can be split into two paths. In order to realize an interferometer for atoms, two magnetic field minima are created initially,

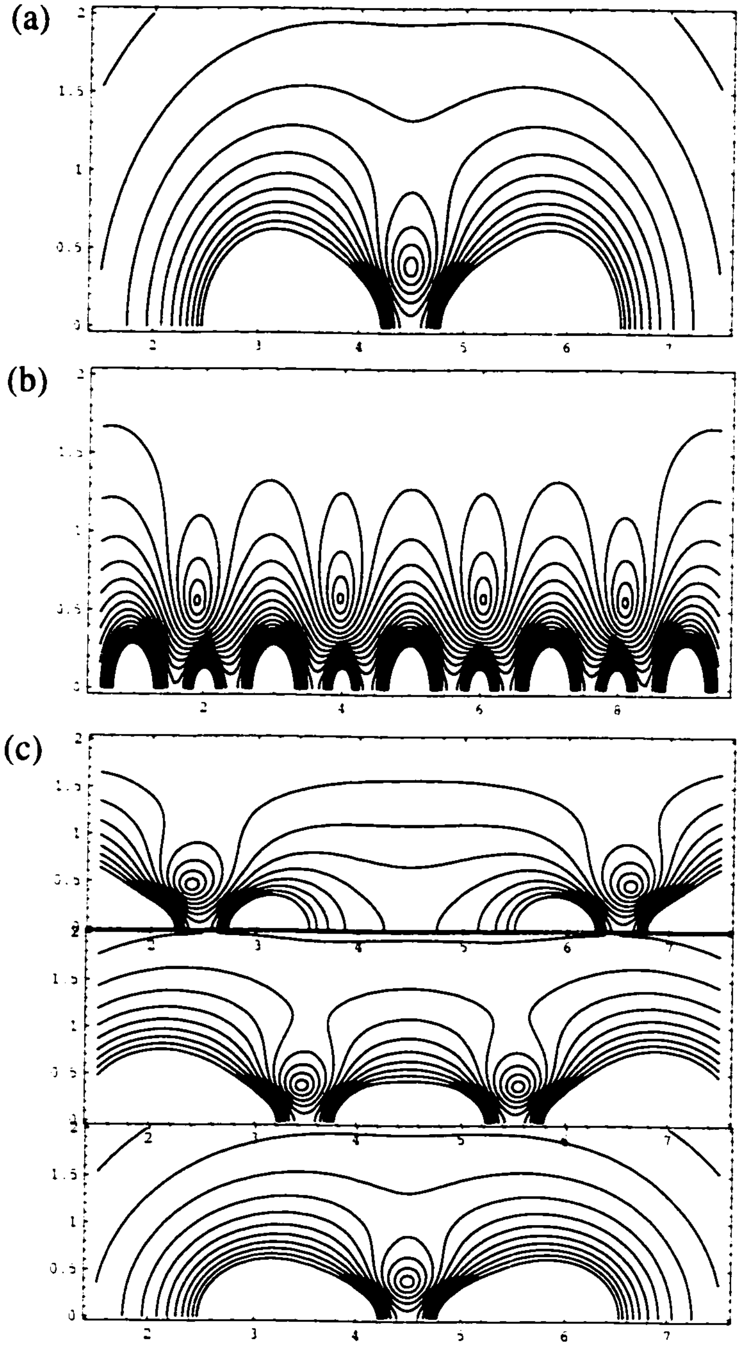

Figure 2.7. Contour plots of computed magnetic field magnitude using the device shown in Fig 2.6. With different current distribution, (a) single magnetic field minimum can be produced that can act as single channel guide for atoms. (b) multiple field minima (four in this case) can be produced simultaneously that can act as multi channel guides. (c) two magnetic field minima can be converged to a single field minimum. This profile can be used as interferometer or beam splitter for atoms.

converged to a single field minimum, and the single field minimum is split again into two minima. Atoms that enter into two separate channels come together when two magnetic field minima are converged to a single field minimum. Atoms are then split into two channels again when the field minimum is separated. This method to manipulate the trajectories of atoms is powerful because we can create many different field configurations without having to alter the shape of the micro-electromagnets. Amount of currents to be supplied to each wire can be calculated, controlled and synchronized by a computer.

When the size of micro-electromagnets become comparable to the de Broglie wavelength of the atoms, as with the device shown in Fig. 2.6, quantum effect can be observed. The energy spacing between modes are quantized and coherent transport of atoms can be possible.

2.4. Nano-Electromagnets for Magnetic Nanoparticles

Combining e-beam lithography with multi-layer fabrication techniques, we have designed and fabricated submicron sized nano-electromagnets for manipulating magnetic nanoparticles. By constructing smaller devices, it is possible to control the location of single or a small group of particles at a time.

Devices were patterned by e-beam lithography using a Raith 150 in the basement of Gordon McKay. There are number of challenges for making devices with wire width smaller than 1 μm, and we have considered various ways for fabrication methods. The difficulty arises from the fact that the spacing between the first conducting layer and the second conducting layer needs to be as thin as possible, yet they must be well separated so that the currents do not leak through the insulating layer. Because of the height of evaporated metals (typically 100 ~ 150 nm), the surface of the structures is not flat, but it has success of hills and valleys. Ideally, the insulating layers need be planarized in order to avoid height variations along the surface using a process called Chemical Mechanical Polishing (CMP). Using a CMP process, oxide layer is planarized by rotating a wafer under pressure against a polishing pad in the presence of silica-based alkaline slurry. As we do not have a CMP machine in our facility, we have proceeded to make our device without planarizing the insulating layer, by using fabrication steps illustrated in Fig. 2.8. In order for the fabrication to be successful, the insulating layers need to be as thin as possible yet there shouldn't be electrical shorting between conducting layers. This can be done by varying the thickness of evaporated materials in each step.

The detailed recipe is as follows:

(1) The patterns are written using e-beam lithography and developed in the cleanroom in the basement of Gordon McKay.

(2) Using a new thermal evaporator, 50 Å of Cr layer for adhesion followed by 1000 Å of Au is evaporated as shown in Fig. 2.8(a).

(3) Evaporate 1500 Å of SiO_2 layer on top of Au layer using an e-beam evaporator (See Appendix A.3 for the complete procedure) in the cleanroom on the 2nd floor, shown in Fig. 2.8(b). The height of the insulating layer must be taller than the height of the evaporated metals so that the second layer of wires does not come in contact with the first layer of wires.

(a) E-beam Lithography: Deposition of 1st conducting layer (100 nm)

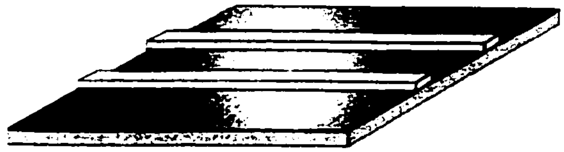

(b) Evaporate 1st insulating layer: SiO_2 (150 nm)

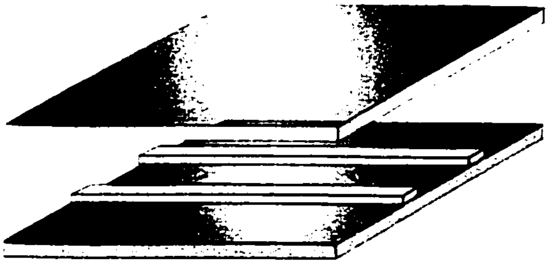

(c) E-beam Lithography: Deposition of 2nd conducting layer (200 nm)

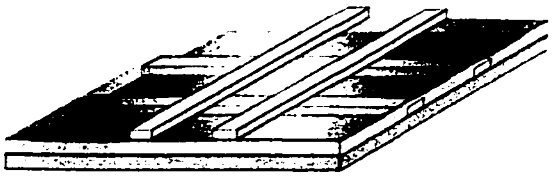

(d) Evaporate 2nd insulating layer: SiO_2 (200 nm)

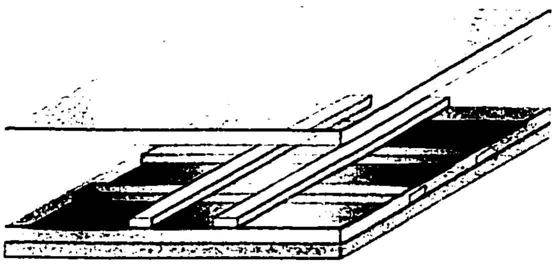

Figure 2.8. Schematic diagrams of fabrication process for multi-layer nano-electromagnets on silicon substrates using electron beam lithography.

(4) Second layer of wires is patterned using e-beam lithography.

(5) Evaporate 2000 Å of Au using a new thermal evaporator, shown in Fig. 2.8(c).

(6) Evaporate 2000 Å of SiO_2 layer as shown in Fig. 2.8(d). This ensures that there is no electrical shorting between two layers of conductors and between the top conductors and solution.

Figure 2.9 shows nano-electromagnets fabricated using fabrication steps described above: a ring trap [Fig. 2.9(a)], double ring traps [Fig. 2.9(b)] and a matrix [Figs. 2.9(c) and 2.9(d)]. A ring trap shown in Fig. 2.9(a) has radius of 250 nm, wire width of 100 nm and wire height of 80 nm with 200 nm thick layer of SiO_2 deposited on the top. With a current of 100 mA ($J = 1.25 \times 10^7$ A/cm^2), a maximum field magnitude $B = 0.1$ T is produced at the center above the surface. Double ring traps shown in Fig. 2.9(b) may be used to manipulate particles between two traps and to study stochastic behavior of the trapped particles.

Figure 2.9(c) shows the micrograph of a 10x10 wire matrix. A large area is shown here to illustrate how currents can be applied to the device. Close up of this matrix is shown in Fig. 2.9(d). Each wire has wire width of 500 nm, wire height of 100 nm for the first layer and 200 nm for the second layer, and the center-to-center spacing between wires is 1 μm. This matrix has 400 times smaller trapping area compared to the matrix fabricated using optical lithography, which was previously shown in Fig. 2.4(a). This gives higher spatial resolution in positioning magnetic particles.

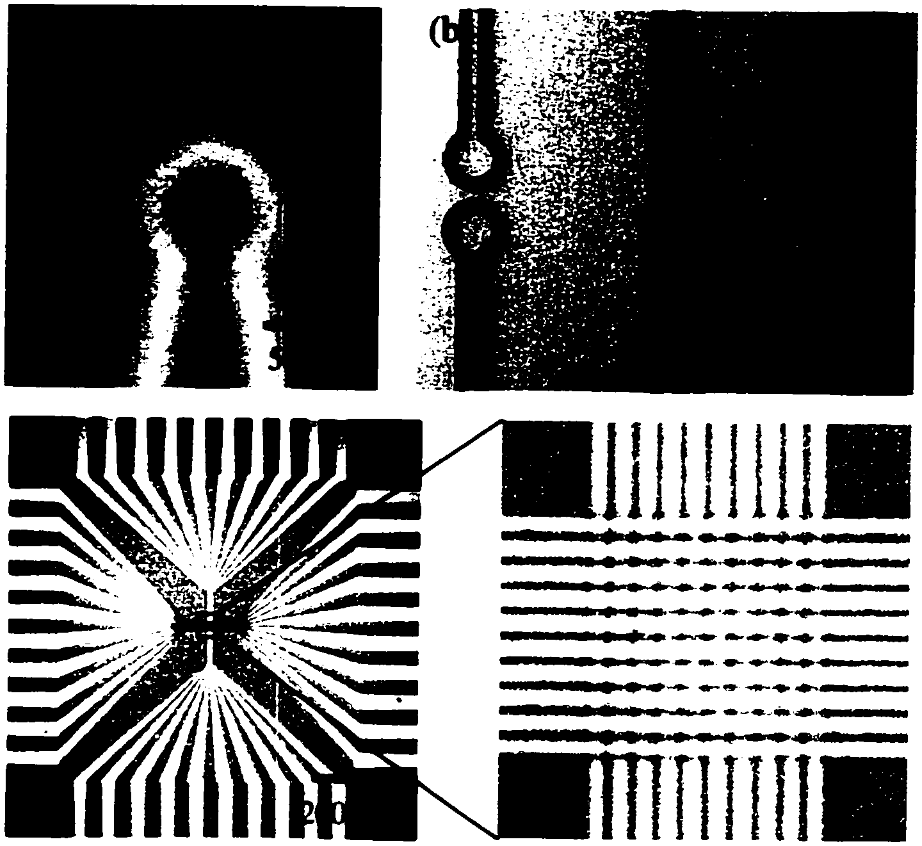

Figure 2.9. (a) Optical micrograph of a fabricated ring trap. A wire has width of 100 nm, height of 80 nm and the thickness of insulating layer (SiO_2) of 200 nm. (b) Micrograph of a fabricated double ring traps. All wires have wire width of 1 μm and height of 100 nm. Outer double traps have radius of 5 μm, while middle double traps have radius of 2 μm. (c) Micrograph of a fabricated matrix (10x10 wires). Larger area is shown in this photo. It shows how wires go out in order to apply currents. (d) Close up of the matrix shown in (c). Each wire has width of 500 nm, height of 100 to 200 nm, and the center-to-center spacing between wires is 1 μm.

2.5. Current Capacity of A Wire

In this section, we investigate both theoretically and experimentally the maximum current density that can be achieved on a wire fabricated on a cooled substrate. Let us consider a simplified case of a normal wire, which has width w, height h, length l and carries a current I, as shown in Fig. 2.10. The wire heats up due to the ohmic heating producing power $P = I^2R$, where R is the resistance of the wire. The rate of heat transfer through the substrate is governed by the heat transfer equation, $H = -\kappa A\nabla T$, where κ is the thermal conductivity of the wire, A is the area of the interface and ∇T is the thermal gradient. The thermal gradient is roughly $\nabla T \cong \Delta T_{max}/h$, where ΔT_{max} is the maximum allowable temperature difference between the wire and the substrate.

The condition to remove the heat effectively via this heat transfer is that the rate of transfer heat through the substrate is greater than or equal to the power generated by wire heating, i.e., $I^2R \leq \kappa A\nabla T$. Because the resistance of the wire is $R = \rho l/(wh)$, where ρ is the electrical resistivity of the wire and $A = wl$, this condition yields following relation:

$$I \leq w\sqrt{\frac{\kappa\Delta T_{\max}}{\rho}}.$$

Therefore, this simple model tells us that the maximum current on a wire fabricated on a substrate is linearly proportional to the width of the wire. Because the current density is inversely proportional to the cross sectional area, i.e., $J = I/(wh)$, the current density is

$$J \leq \sqrt{\frac{\kappa\Delta T_{\max}}{\rho}},$$

which is independent of the wire width. For Au at room temperature with $\Delta T_{max} = 100$ K

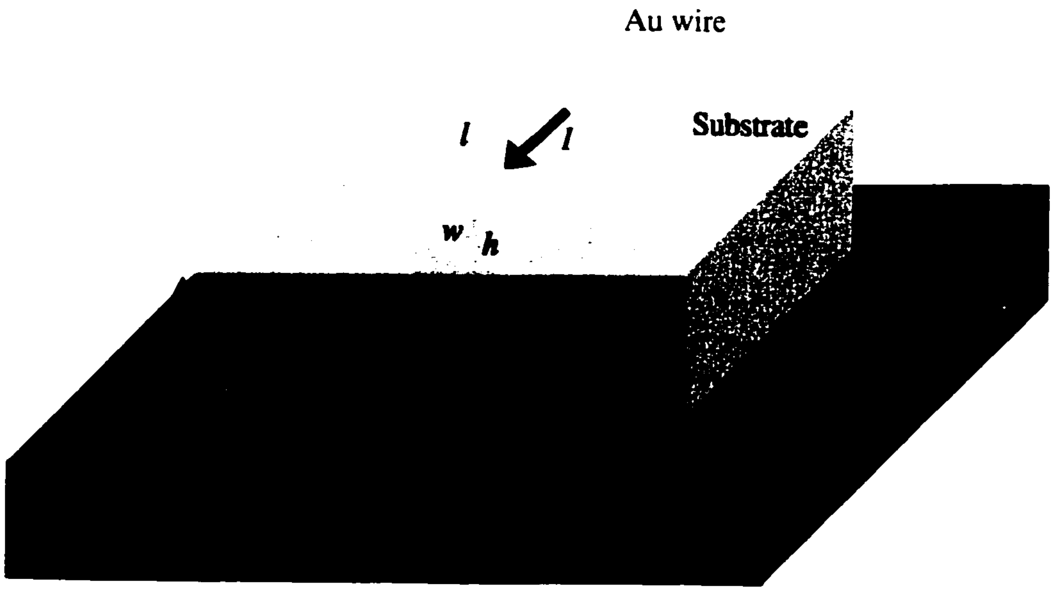

Figure 2.10. Schematic diagram of a Au wire fabricated on a substrate. Au wire has width *w*, height *h*, length *l* and carries a current *I*. The wire heats up due to the ohmic heating and the heat is transferred through the substrate, which sits on a copper plate. Copper plate is cooled down using a thermoelectric cooler. Heat is removed by conduction through the substrate.

and standard values for κ and ρ, we obtain $I/w \leq 1$ A/μm [Drndic M. *et al.*, 1998]. This corresponds to a current density of 10^8A/cm^2 through wires that have cross sectional area of 1 μm x 1 μm. Cooling can be used to achieve even higher values of I/w by reducing ρ and increasing κ.

The current capacity of wires fabricated on silicon substrates was tested on a copper plate that was cooled to 7 °C ($T = 280$ K) using a thermoelectric cooler (Peltier cooler) by applying constant currents through four wires with different wire widths. Test wires were fabricated on a same substrate using e-beam lithography such that same amount of Au is evaporated for all the wires. Fabricated wires have wire widths of 1 μm, 2 μm, 5 μm and 10 μm with wire height of 100 nm.

Figure 2.11 shows I-V graphs for four wires, where the current I was slowly ramped up continuously for each wire and the voltage V was measured along the length l of the wires. With the increase in current, the resistance of the wire increases due to the heating of the wire. The temperature increase in the wires can be deduced from the resistance change and they are evaluated later. As the current is increased in small increments, the wires quickly come to thermal equilibrium with the cold plate.

The important results are summarized in Table 6.1 below, where the table shows the maximum current and current density that was achieved for each wire. Data shows that the maximum current is linearly dependent on wire width and maximum current density is independent of wire width, which are in agreement with the theory presented earlier. For higher current amounts than reported here, the wires did not come to thermal equilibrium with the cold plate. Instead, we observed that the resistance kept going up

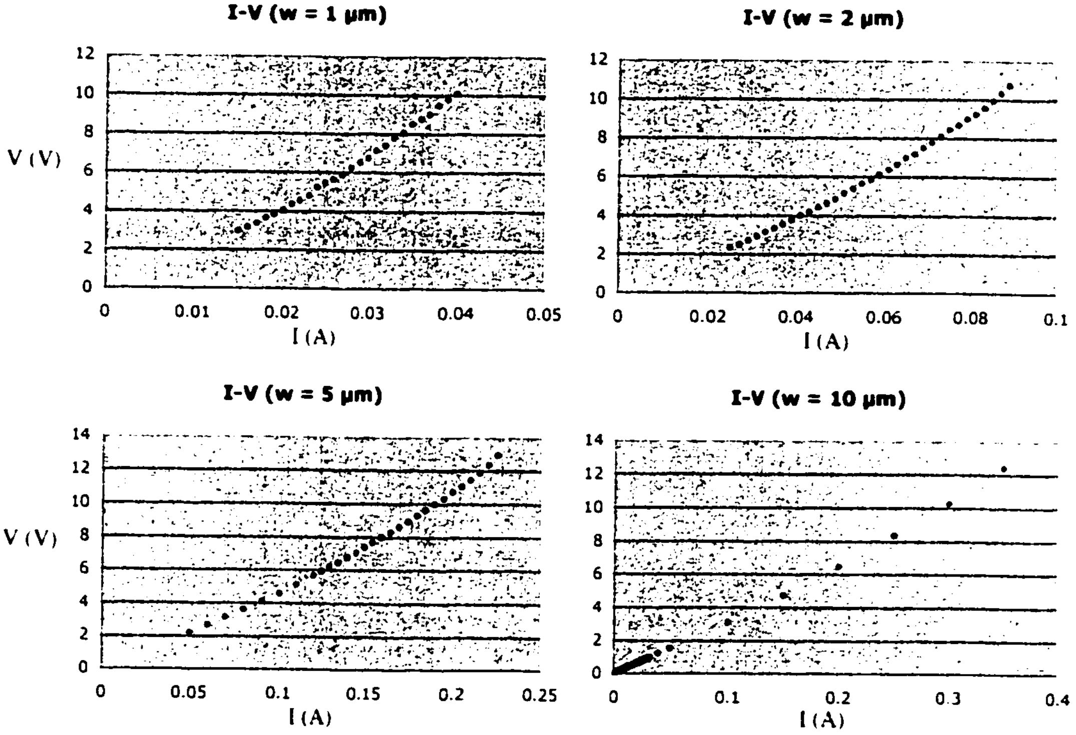

Figure 2.11. I-V graphs for four different wires. All four wires have the same height of 100 nm, but widths are varied: 1 µm, 2 µm, 5 µm and 10 µm. Current was ramped up continuously in constant current mode for each wire. For higher currents, resistance increases due to the heating on the wires.

Wire Area	1 μm x 0.1 μm	2 μm x 0.1 μm	5 μm x 0.1 μm	10 μm x 0.1 μm
I_{max} (A)	0.04	0.089	0.225	0.4
J_{max} (A/cm^2)	4 x 10^7	4.45 x 10^7	4.5 x 10^7	4 x 10^7

Table 2.1. Maximum current and current density achieved for various wire sizes. The substrate was placed on a copper plate, which was cooled to 280 K. Wire height is the same for all the wires at 0.1 μm, while width is varied from 1 μm to 10 μm. Maximum current density of 4.5 x 10^7 A/ cm^2 was achieved for the wire size 5 μm x 0.1 μm.

without stabilizing, eventually breaking one of the wires. We have achieved maximum current density of better than 4 x 10^7 A/ cm^2 for all four wires. The highest current density was achieved for the wire size 5 μm x 0.1 μm, which yielded 4.5 x 10^7 A/ cm^2. This is much better than the maximum current density that has been achieved with superconducting wires, which is ~ 10^7 A/cm^2 for Pb at $T = 4$ K. The maximum current in superconductors is limited either by the critical field H_c for type I, or by flux pinning for type II superconductors.

Figure 2.12 shows the calculated plots of temperature vs. squared current (T vs. I^2) for all four wires. From this calculation, we can estimate how much a wire heats up when current flows through it. From I-V graphs shown in Fig. 2.11, we determined the resistance of the wire for each current amount and deduced the temperature rise on a wire due to the heating using the resistance-temperature relation, $R = R_0[1 + \alpha(T - T_0)]$, where α is temperature coefficient. The wires heat up significantly when maximum current amount is applied: 80 K increase for 1 μm, 87 K increase for 2 μm, 93 K increase for 5 μm and 53 K increase for 10 μm wire width. The temperature

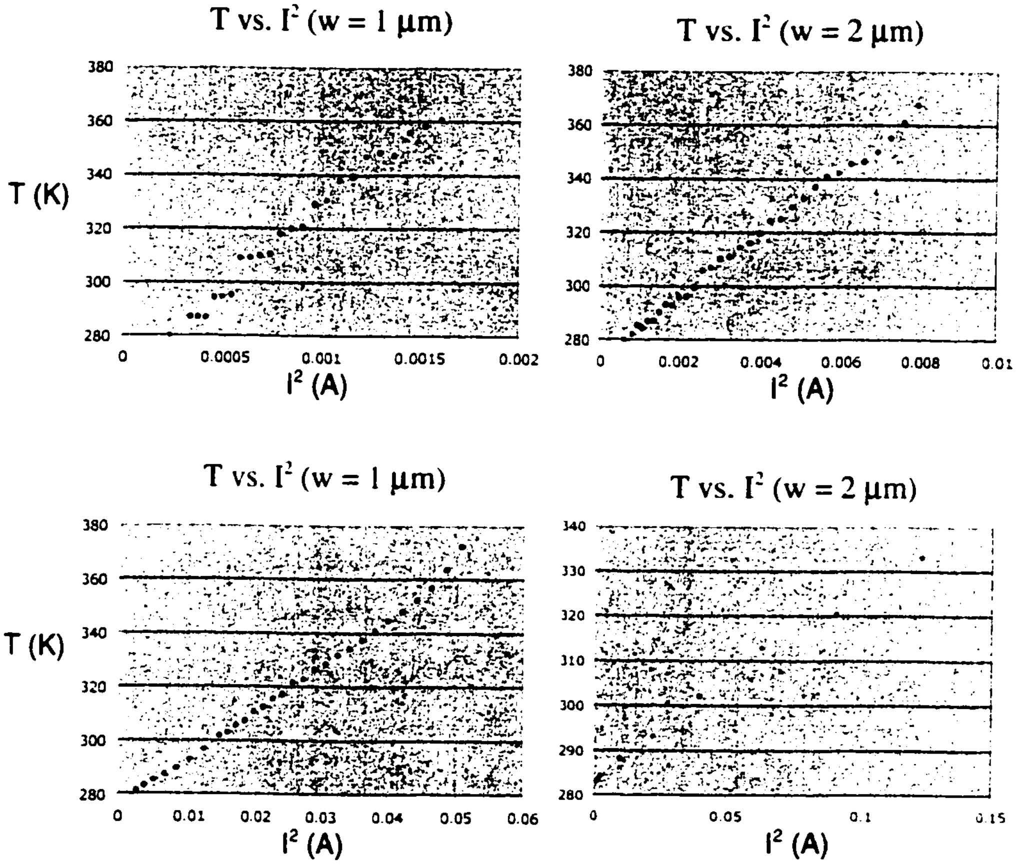

Figure 2.12. Temperature vs. squared current plots (T vs. I^2) for four wires with different width. Temperature rise on a wire is calculated from the increase in wire resistance. At maximum current, temperature rise of as high as 93 K is observed for a wire width of 5 µm.

increase on the wire should be linearly proportional to the power generated by the ohmic heating on the wire. The linear dependence is clearly shown in the plots.

2.6. Summary

In conclusion, we have described in detail how to fabricate various kinds of micro-electromagnets for manipulating both atoms and magnetic particles. Both optical lithography and e-beam lithography were used in fabricating devices with wire sizes ranging from 0.1 μm to 100 μm. We have also discussed the magnetic field profiles that are produced by these micro-electromagnets.

Continuous currents with current densities up to 4.5 x 10^7 A/cm^2 have been achieved on the wires fabricated on silicon substrates, with substrates cooled to temperature $T = 280$ K using thermoelectric cooler. This corresponds to the current $I = 0.45$ A through a wire with 1 μm^2 cross sectional area. With this current density, magnetic field magnitude $B = 0.1$ T can be produced on the surface of a wire. Higher current densities may be obtained for these wires either by cooling the substrate further using nitrogen feedthrough, or by pulsing currents through the wires.

Chapter 3

MICRO-ELECTROMAGNETS FOR THE CONTROL AND MANIPULATION OF COLD NEUTRAL ATOMS

Micro-electromagnets provide flexibility and versatility to manipulate atoms on a chip, and may open possibilities ranging from integrated atom circuits to quantum dots in vacuum for quantum computation systems. In this Chapter, we describe the design, construction and operation of micro-electromagnets to control the trajectories of ultra cold neutral atoms dropped from a magneto optical trap (MOT). These micro-electromagnets consist of single layer of current-carrying Au wires fabricated on sapphire substrates using lithography and electroplating techniques. The magnetic field patterns produced by these devices allow microscopically precise control and manipulation of cold neutral atoms. In particular, we describe in detail how to design a micro-electromagnet atom guide and demonstrate the guiding of atoms using the device.

3.1. History and Overview

In recent years, micro-electromagnets have played important roles as new tools in micro-manipulating cold neutral atoms in the field of atom optics. The field of atom optics seeks to develop optical elements such as mirrors, traps, guides, gratings, lenses and interferometers for atoms that will lead to the development of integrated atom optical devices. As an effort to build these devices, various techniques have been developed and employed. One method exploited light-atom interactions to demonstrate reflection, diffraction, focusing and trapping of atoms [Adams C.S. *et al.*, 1994]. Another method is to exploit interactions between magnetic fields and the intrinsic magnetic moment that atoms possess. Utilizing magnetic interactions, mirrors using macroscopic permanent rare-earth magnets [Sidorov A. I. *et al.*, 1996] and magnetic tapes [Roach T.M. *et al.*, 1995] have been experimentally demonstrated. Current-carrying microstructures have been developed and experimentally demonstrated that can manipulate atoms above the surface of a substrate [Drndic M. *et al.*, 1998]. These micro-electromagnets, first developed in our group, are the focus of this Chapter.

Recently, a number of manipulation schemes for atoms above planar microstructures have been suggested and experimentally demonstrated. Micro-electromagnet mirrors for atoms have been demonstrated in both deflection [Drndic M. *et al.*, 1998; Johnson K.S. *et al.*, 1998] and reflection [Drndic M. *et al.*, 1999; Cognet L. *et al.*, 1999] experiments. Micro-electromagnet traps have been proposed [Weinstein J.D. *et al.*, 1995], a wire trap for atoms have been experimentally demonstrated to confine atoms along a free standing wire [Fortagh J. *et al.*, 1998], and micro traps fabricated on a chip have been demonstrated to trap atoms above the surface [Reichel J. *et al.*, 1999]. With the development of a mirror MOT [Kim J.A. *et al.*, 1997; Reichel J. *et al.*, 1999], atoms can be loaded into the micron sized structures without much loss; loading of atoms to micro-electromagnets on a substrate from conventional MOT resulted in considerable loss of atoms. Micro-electromagnet guides have been experimentally demonstrated to guide atoms above a substrate [Dekker N.H. *et al.*, 2000; Mueller D. *et al.*, 1999]. Three-dimensional (3D) micro-electromagnets also have been proposed and fabricated [Drndic M. *et al.*, 2000], which give spatially symmetric potential with bigger trap depth and stronger forces to confine atoms. The possibility of entangling neutral atoms for quantum computation has been discussed [Drndic M. *et al.*, 2000]. Recently, Bose Einstein Condensation (BEC) of atoms has been demonstrated using a miniaturized current carrying surface trap [Hansel W. *et al.*, 2001; Ott H. *et al.*, 2001].

In this Chapter, we describe the design, magnetic field calculations and operation of micro-electromagnet guides that we have developed and tested experimentally. Specifically we report (1) micron and sub-micron sized atom guides, (2) loading of atoms into guides, (3) simulations of the magnetic potential that atoms see in the loading process, and (4) experimental demonstrations of atom guiding. We also propose a new micro-electromagnet that may act as both interferometer and beam splitter for atoms.

3.2. Interaction Potential

Micro-electromagnets consist of lithographically patterned current carrying wires on a substrate, which produce locally generated magnetic fields to control the trajectories of cold neutral atoms with micron or submicron spatial resolution. The magnetic dipole interaction between the intrinsic magnetic moment that atoms possess and the inhomogeneous magnetic field produced by micro-electromagnets allow precise control of the trajectories of atoms above the substrate inside the vacuum system. The magnetic dipole interaction potential is given by

$$U(x,y,z) = -\vec{\mu} \cdot \vec{B}(x,y,z),$$

where $\vec{\mu} = -g_F \mu_B \vec{J}$ is the magnetic moment of the atom, $\vec{J}$ is the angular momentum, μ_B is the Bohr magneton, g_F is the Landé g-factor, and $\vec{B}$ is the magnetic fields produced by a micro-electromagnet. If the magnetic moment of the atoms can follow the change in direction of the magnetic field adiabatically, the potential can be written in the form

$$U(x,y,z) = g_F m_F \mu_B B,$$

where m_F is the magnetic quantum level of the atomic sublevel. In this adiabatic regime, the potential only depends on the magnitude B of the magnetic field, but not on its direction. The force exerted on atoms due to this potential is then

$$\vec{F} = \nabla(\vec{\mu} \cdot \vec{B}) = -g_F m_F \mu_B \nabla B.$$

Therefore, atoms with positive magnetic quantum number ($m_F g_F > 0$) will be repelled by increasing magnetic field gradient and attracted to field minima; these atoms are commonly referred as weak field seeking atoms. On the other hand, atoms with negative magnetic quantum number ($m_F g_F > 0$) will be attracted to increasing magnetic field gradient and attracted to field maxima, hence called strong field seeking atoms.

Micro-electromagnets are designed to manipulate weak field seeking atoms ($m_F g_F > 0$) because it is possible to create local minimum region in magnetic field magnitude in free space, but not a maximum in field magnitude. This makes manipulation of atoms using micro-electromagnets attractive and versatile because the magnitude B can be tailored to achieve a particular manipulation scheme such as reflection, trapping or guiding, by designing the wire geometry and the current distribution accordingly.

As discussed above, the magnetic field magnitude B, not its direction, determines the trajectory of atoms in the adiabatic regime. In order for atoms to remain in adiabatic

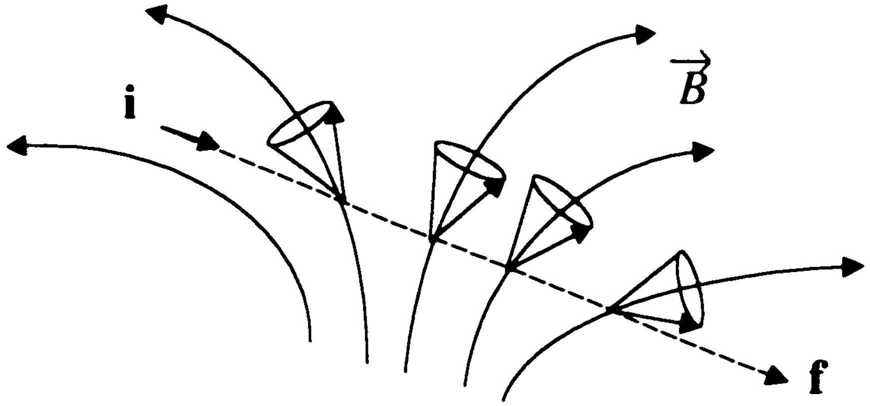

Figure 3.1. Schematic diagram illustrating the adiabaticity of atoms in changing magnetic fields. The cones (in blue) represent the atoms' magnetic moment precessing around the local magnetic field. In adiabatic regime, atoms moving from point *i* to point *f* experience changing magnetic field direction and align its magnetic moment to preserve the angle between the its magnetic moment and the magnetic field.

regime, atoms should move through magnetic fields adiabatically, i.e., the atoms should not make transitions between Zeeman sublevels. As atoms move from point i to point f in changing magnetic fields, the projection of atoms' magnetic moment onto the magnetic field should remain constant, as illustrated in Fig. 3.1. The condition is met if atoms move slowly enough compared to the rate of change of the direction of the magnetic field. The adiabatic condition can be expressed as

$$\omega_{ij} << \partial \hat{e}_B / \partial t \, ,$$

where ω_{ij} is the transition frequency between magnetic sublevels, $\hat{e}_B = \vec{B} / |\vec{B}|$ is the unit vector of the magnetic field $\vec{B}$, and $\partial \hat{e}_B / \partial t$ is the rate of change of the direction of the magnetic field. This condition is not met if atoms go through a region where field magnitude is zero. During the experiment, zero field regions is avoided by applying small external magnetic field, commonly referred as a holding field.

3.3. Micro-electromagnet Atom Guides

A micro-electromagnet atom guide consists of an array of current carrying wires with currents flowing in alternate directions. By optimizing current distribution on the wires, an atom guide produces a region of magnetic field minimum, where weak field seeking atoms can be guided above the surface of a substrate. For a micro-electromagnet to guide atoms from one position to another above a surface, it needs to generate magnetic fields, which gives confining potential in transverse dimension, but not confining in longitudinal dimension. A number of ways to realize an atom guide using current carrying wires fabricated on a substrate are described by [Thywissen J.H. *et al.*, 1999]. Although straight wires are discussed and experimentally tested in our group [Dekker N.H. *et al.*, 2000], curved wires can also guide atoms [Mueller D. *et al.*, 1999]. All the calculations shown in this section assume that the wires are point wires having infinite lengths. Calculations correcting for the finite size of wires are shown later.

There are four simple ways to achieve guide for atoms: one wire + external magnetic field, two wires + external magnetic field, three wires, and four wires. Each wire configuration is described in detail in following text.

One-wire guide – Figure 3.2 shows a schematic diagram and a computed magnetic field profile of a one wire guide. The magnetic field produced by a single wire in the y-direction, is cancelled by applying homogeneous external magnetic field B_{ext} as shown in Fig. 3.2(a). As a result, a magnetic field minimum is formed above the substrate that gives two-dimensionally confining potential for weak field seeking atoms. Weak field seeking atoms are guided along this confining potential to form an atom guide. The location where this minimum is formed can be easily calculated; it is given by

$$h = \frac{\mu_o I}{2\pi B_{ext}},$$

where $\mu_o = 4\pi \times 10^{-7}$ and I is the current on a wire. The field gradient at this minimum is

$$\nabla B\,(z = h) = \frac{2\pi B_{ext}{}^2}{\mu_o I}.$$

Figure 3.2(b) shows a contour plot of wire configuration shown in Fig. 3.2(a).

Two-wire guide – Figure 3.3 shows a schematic and magnetic field profile for a two-wire guide. Two wires separated by distance S produces magnetic field in z-direction between wires when equal amount of currents are applied in opposite direction.

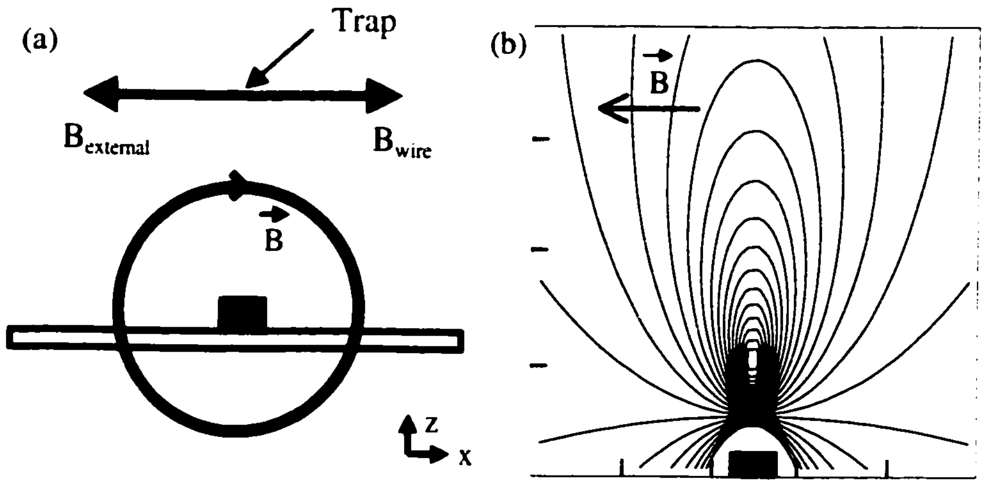

Figure 3.2. (a) Schematic diagram of a one-wire guide. Magnetic field produced by single wire is cancelled by an external magnetic field. (b) Contour plot for one-wire guide shown in (a).

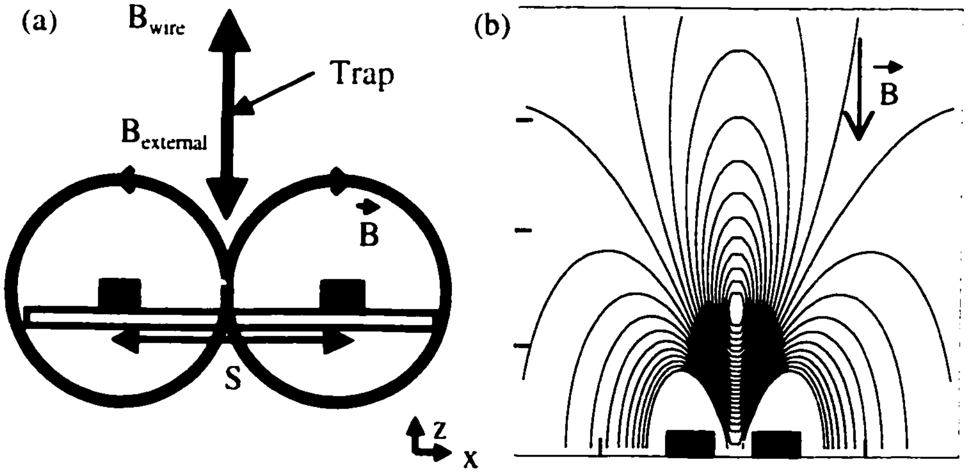

Figure 3.3. (a) Schematic diagram of a two-wire guide. Magnetic field produced by two wires is cancelled by an external magnetic field. (b) Contour plot for two-wire guide shown in (a).

Midway between the wires, the magnetic field magnitude produced by two wires is

$$B\,[x=0,z]=\frac{\mu_o I}{2\pi}\frac{S}{(z^2+S^2/4)}\hat{z}.$$

By applying an external magnetic field in the z-direction, which is opposite to the field direction produced by two wires, the minimum is formed above the substrate shown schematically in Fig. 3.3(a). For two wires with external magnetic field, B_{ext}, this minimum is formed at height h above the substrate,

$$h=\sqrt{\frac{\mu_o IS}{\pi B_{ext}}-\frac{S^2}{2}}.$$

Figure 3.3(b) shows a contour plot for two-wire configuration.

Three-wire guide – Figure 3.4 shows a schematic diagram and a magnetic field profile for a three-wire guide. Unlike one- or two-wire guides, a three-wire or four-wire guide, shown next, do not require an external magnetic field to form a field minimum. Instead, magnetic fields produced by two outer wires are cancelled by magnetic fields produced by an inner wire. The minimum is formed right above the middle wire for a three-wire guide.

Four-wire guide – Figure 3.5 shows a schematic diagram and a magnetic field profile for a four-wire guide. The wires are separated by equal distances, with the spacing between adjacent wires S. When currents flow in alternate directions, the magnetic field produced by the two outer wires is cancelled by the fields produced by two inner wires at a location above the substrate as shown in Fig. 3.5(a).

The location of a magnetic field minimum can be precisely controlled, because it depends on two things: the spacing between wires S and the current ratio between the inner and the outer wires. Figure 3.5(b) shows the computed contour plot of magnetic

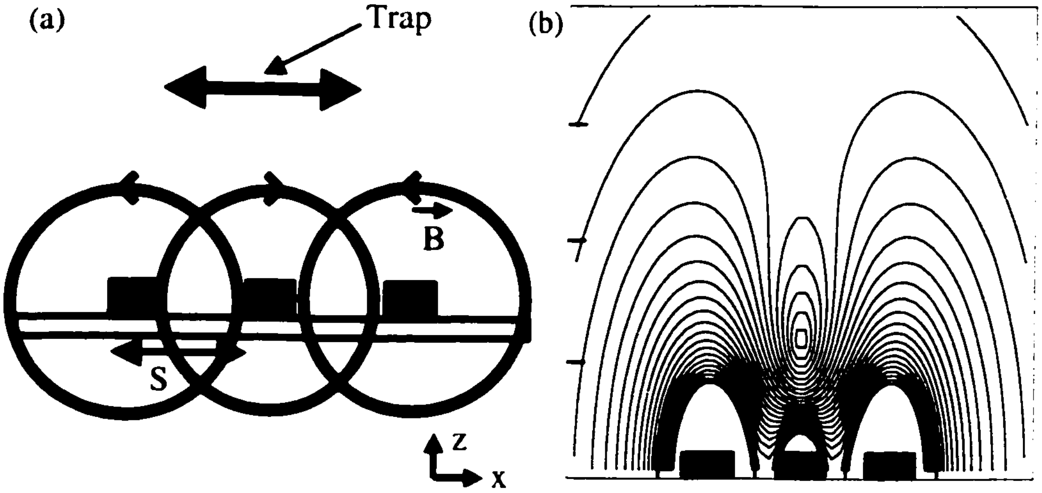

Figure 3.4. (a) Schematic diagram of a three-wire guide. Magnetic field produced by two outer wires is cancelled by field produced by an inner wire. No external field is needed to form a minimum. Field minimum is formed right above the middle wire. (b) Contour plot for three-wire guide shown in (a).

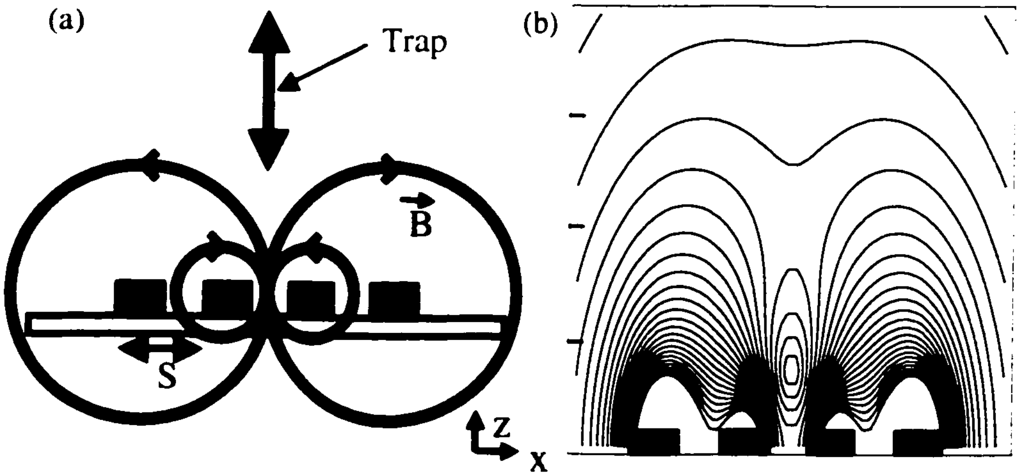

Figure 3.5. (a) Schematic diagram of a four-wire guide. Magnetic field produced by two outer wires is cancelled by field produced by two inner wires. (b) Contour plot for four-wire guide shown in (a).

field magnitude for the wire geometry shown in Fig. 3.5(a). For a four-wire guide, the location where the magnetic field is zero is formed at height h above the substrate

$$h = \frac{S}{2}\sqrt{\frac{9-3\alpha}{3\alpha-1}},$$

where $\alpha = I_{out} / I_{in}$, where I_{out} are the current on outer wires and I_{in} are the current on inner wires. For example, the location of the zero field in magnitude is $h = 0.39S$ above the surface for $\alpha = 2$. The radial field gradient of the field magnitude near its minimum is

$$\nabla B\,(z = h) = \frac{\mu_o I}{8\pi S^2}\frac{1}{\alpha}\sqrt{(3\alpha-1)^5(1-\frac{\alpha}{3})}.$$

The field gradient is maximized at $\alpha = 2.38$ to give $\nabla B = 4.46\mu_o I/(2\pi S^2)$.

We briefly summarize the difference between four different guides discussed above. It can be easily seen that one or two wire guides have larger trapping area compared to those with three or four wires, therefore one or two-guides can confine and guide more atoms. In addition, by adjusting the magnitude of the external magnetic field, the height where the minimum is formed can be easily changed, which can be useful to load atoms to the device more effectively. One and two-wire guides require external magnetic field to function; this could cause problem when integrating a guide with other atom optical devices, which may not require an external magnetic field. Atom guides with three and four wires have a smaller trapping area, but they have larger field gradients and curvatures than the atom guides with one and two wires.

The adiabaticity is discussed briefly here. Although weak field seeking atoms are attracted to the minimum of the magnetic field, this minimum must not be zero. At a point where the magnetic field is zero, atoms lose their adiabaticity and can flip their spins, causing the atoms to be pushed out of the trap. To avoid the formation of zero field in the guide potential, a weak homogeneous external magnetic field must be applied in z-direction. This magnetic field is called a holding field, denoted $B_h(z)$, because it keeps atom from flipping their spins. Near the minimum, this holding field creates harmonic potential and the oscillation frequency of an atom near this quadratic minimum is $\omega = \sqrt{\mu B'^2 / M B_h}$ (in cgs unit), where μ is the magnetic moment and M is the mass of the atom.

The loss rate due to spin flip has been calculated [Bergeman T.H. *et al.*, 1989] for atoms passing through a singular point produced by a quadrupole trap, and it is found to be significant. The loss rate can be reduced by applying a holding field B_h, and the spin flip loss rate (or transition rate, w) of an atom in the ground state with this holding field is given by [Sukumar C.V. *et al.*, 1997]

$$w = \frac{\pi\omega}{2\sqrt{e}} \exp\left[-\frac{\mu B_h}{\hbar\omega}\right],$$

where ω is the oscillation frequency.

The device to be discussed in the next section shown in Figure 3.6, where the center to center spacing between wires is $S = 200$ μm, is a multi-mode atom guide and this transition rate is negligibly small. However for smaller devices, the transition is a more prominent phenomenon. It was shown [Thywissen J.H. *et al.*, 1999] that for a device with $S = 5$ μm and with $I = 0.9$ A and $\alpha = 2$, the field gradient the near guide center is $\nabla B = 2.9 \times 10^6 G/cm$. In this guide, rubidium (^{87}Rb) confined in the $|F = 2; m_F = +2>$ state would have a classical oscillation frequency of $\omega = 2\pi$ x 1.1 MHz and a level spacing of 52 μK. By applying a holding field of $B_h = 12$ G, the transition rate due to spin flips near field minimum is ~ 1 Hz.

3.4. Design of Micro-electromagnet Atom Guides

In this section, we discuss how to design a micro-electromagnet that can guide atoms most effectively. Lithography is used to define micron sized structures to control the trajectories of atoms. Small alterations in the shape of the structures can affect the atom trajectories significantly, and careful design should be implemented in constructing a device. We will demonstrate how slight alterations in wire geometries change the magnetic field profile produced by the device, and show how optimizing wire geometry can help loading atoms smoothly into the device.

Figure 3.6 shows a photograph from an optical microscope of a micro-electromagnet guide that we have fabricated. The device was fabricated using optical lithography and electroplating technique described in detail in section 2.1. A variety of guide configurations with 1 to 4 wires can be achieved by using a single four-wire device because each wire is individually connected to a current supply and only selected wires can be energized during the experiments.

The geometry of a micro-electromagnet guide is discussed in following text. As shown in Fig. 3.6, the top and bottom parts of the guide are symmetric and they extend out with different slopes. Lead wires to connect to a current supply must be attached to the device and eight contact pads are patterned where these wires are attached. Each contact pad has area of 1 mm^2. They are located as far away as possible from the central part of the device where atoms travel.

It is important to carefully calculate and design the whole device in order to load atoms into the guide effectively without losing many atoms in the process. One of the

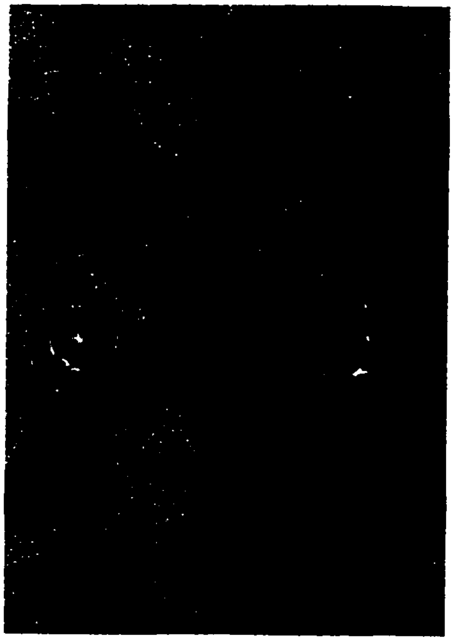

Figure 3.6. Fabricated atom guide with four straight current carrying wires. Each wire has wire width of 100 μm and the center to center spacing between wires is 200 μm. Two holes are drilled using diamond tips in the physics machine shop so that the sapphire substrate can be mounted on a copper cold finger.

difficult tasks in atom manipulation using micro-electromagnets is to load cold atoms into the micron scale devices from the atom source, usually magneto optical trap, because atoms can easily escape during the loading process unless proper loading scheme is implemented. Special care must be taken into account in designing a device because stray fields due to leads can alter the magnetic field profile dramatically, resulting in loss of atoms even before atoms see the device. Magnetic field profile produced by the guide can be optimized by patterning wires to extend out at angle to minimize the potential bump that atoms see when they enter the device. This way, the amount of atom loss can be reduced. This is discussed in detail in following texts.

Figure 3.7 shows a schematic diagram of a model that has four-wire segments of finite length and the computed magnetic field profiles of this geometry at the entrance point, labeled P in the figure. Note that the wire geometry in Fig. 3.7(a) can not be physically realized in a real experiment because it does not form a current loop. The magnetic field calculations for this wire geometry are shown here to compare with actual wire geometries that will be shown later.

Figure 3.7(b) shows the contour plot of the magnetic field produced at the entrance of the device, through dotted line P, by the wire geometry shown in Fig. 3.7(a). The plot is calculated numerically with following parameters: spacing between adjacent wires, $S = 200$ μm, currents on outside wires, $I_{out} = 2$ A, and currents on inside wires, $I_{in} = 1$ A. The contours have spacing of 2 G. It produces magnetic trap with trap depth of $B \sim 5$ G with trap area of 150 μm in z-direction and 100 μm in x-direction. Figure 3.7(c) shows a slice of the magnetic field magnitude through x = 0. At the surface (y = 0) the magnetic field has a finite value which falls off rapidly until it reaches zero at $y = 0.8S$.

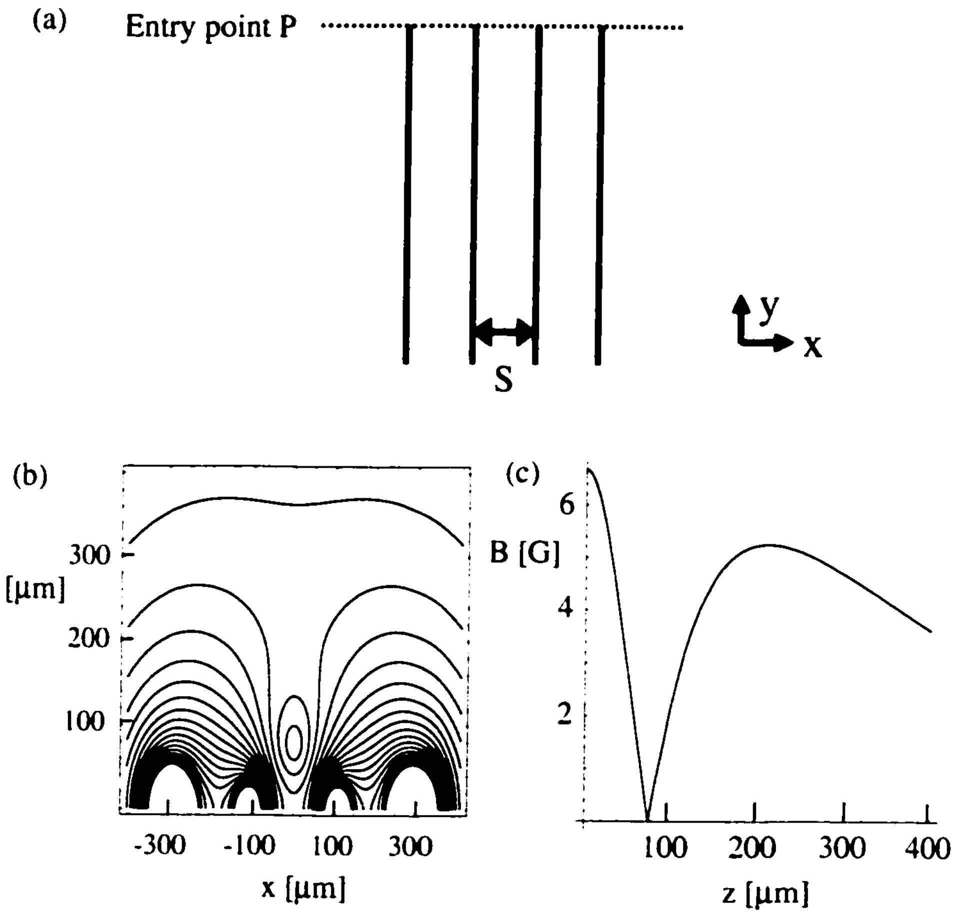

Figure 3.7. Schematic diagram and magnetic field plots of four-wire segments of finite length. Note that this wire geometry is not physically possible because wires do not form a current loop. (a) Schematic diagram of a four-wire guide, which has four parallel wires. (b) Contour plot of magnetic field magnitude through entry point P. The plot is calculated numerically starting from Biot-Savart law. A minimum is formed above the surface. (c) Plot of field magnitude through slice at $x = 0$. The field minimum is formed at $z = 80$ μm, i.e., $z = 0.4S$.

The magnetic field magnitude increases slowly as y is further increased ($y \sim S$) and then decreases again at higher y values ($y > S$). Atoms entering this region ($0 < y < S$) will be guided along the length of the wires.

For a real device, the wires should be continuous and connected to current supplies. Figure 3.8(a) shows a schematic diagram of a wire geometry where wires extend out at right angle to connect to the pads. Although it looks like a legitimate wire geometry to function as an atom guide, the magnetic field simulations for the device shows that it is not.

Figure 3.8(b) shows the contour plot of the magnetic field produced at the entrance of the device, through dotted line P, by the wire geometry shown in Fig. 3.8(a). The plot is calculated using the same parameter as above: spacing between adjacent wires, $S = 200$ μm, currents on outside wires, $I_{out} = 2$ A, and currents on inside wires, $I_{in} = 1$ A. The contours have spacing of 2 G. Unlike the earlier wire geometry shown in Fig. 3.7, this wire geometry produces a magnetic field pattern with no local minimum that decreases monotonously away from the surface as shown in Fig. 3.8(c), which is a slice of the magnetic field magnitude through $x = 0$. Weak field seeking atoms entering the device are pushed away from the surface, while strong field seeking atoms are attracted to the surface; hence most of atoms are lost and never make it to the lower part of the device where the minimum is formed by straight parts of the wires.

For this reason, it is important to design micro-electromagnets very carefully and all parts of the wires should be taken into an account when calculating for the magnetic fields. We have investigated many wire geometries to get optimum magnetic field

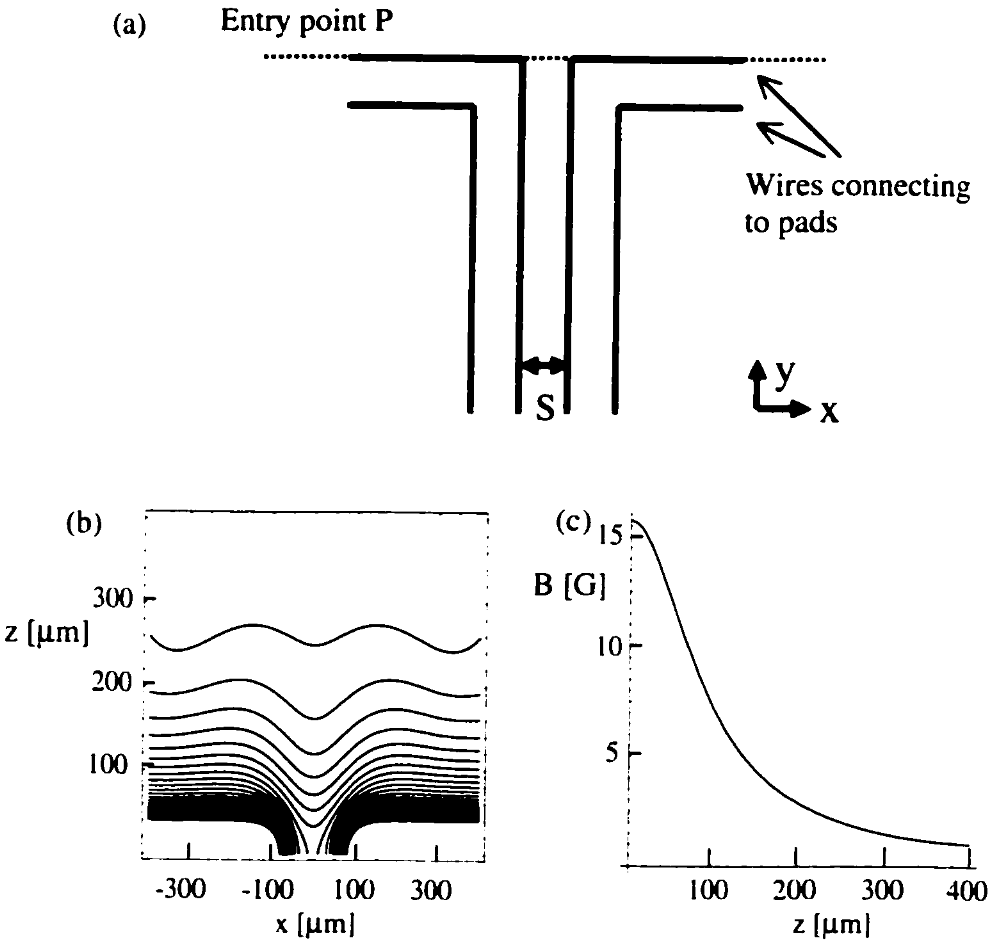

Figure 3.8. (a) Schematic diagram of a four-wire guide, where wires extend out at right angle to connect to the pads. (b) Contour plot of magnetic field magnitude through entry point P. Note that there is no local field minimum above the surface. (c) Plot of field magnitude through slice x = 0. Field magnitude decreases monotonously away from the surface.

profile, which can lead to maximum loading of atoms into the device. The best result is obtained for the wire geometry shown in Fig. 3.9.

Figure 3.9(a) shows a schematic diagram of a funnel shaped wire geometry, where the wires extend out at different angles. This geometry gives the best magnetic field profile to load atoms smoothly into the guide. It consists of three parts: (1) wires that go straight out to the pads that are perpendicular to incoming atoms, (2) funnel shaped part that connect to (1), and (3) four straight wires that are parallel to incoming atoms. For region (3), the magnetic potential remains almost constant along the wire length. The wires are patterned such that the wires are equally distanced from each other. The angles at which the wires extend out may be arbitrarily chosen as long as the wires are equally distanced from each other.

For the device shown in Fig. 3.6, the wires are angled at $\theta_1 = 59°$ (slope = ± 5/3) and $\theta_2 = 79°$ (slope = ± 5). Figure 3.9(b) shows the contour plot of the magnetic field produced through dotted line P for the wire geometry shown in Fig. 3.9(a). The plot is calculated using the same parameter as above: spacing between adjacent wires, $S = 200$ μm, currents on outside wires, $I_{out} = 2$ A, and currents on inside wires, $I_{in} = 1$ A. The contours have spacing of 2 G. Unlike the wire geometry shown in Fig. 3.8, this wire geometry produces a magnetic field minimum with trap depth of ~ 7.5 G. The slice of the magnetic field magnitude through x = 0 is shown in Fig. 3.9(c). As evident from the magnetic field plots shown, this wire geometry produces optimum magnetic fields at the entrance of the device, thus it is investigated further.

Figure 3.10 shows a 3D plot of a magnetic field surface at constant magnitude $B = 2$ G as well as contour plots of field magnitude along the funnel shaped region. All

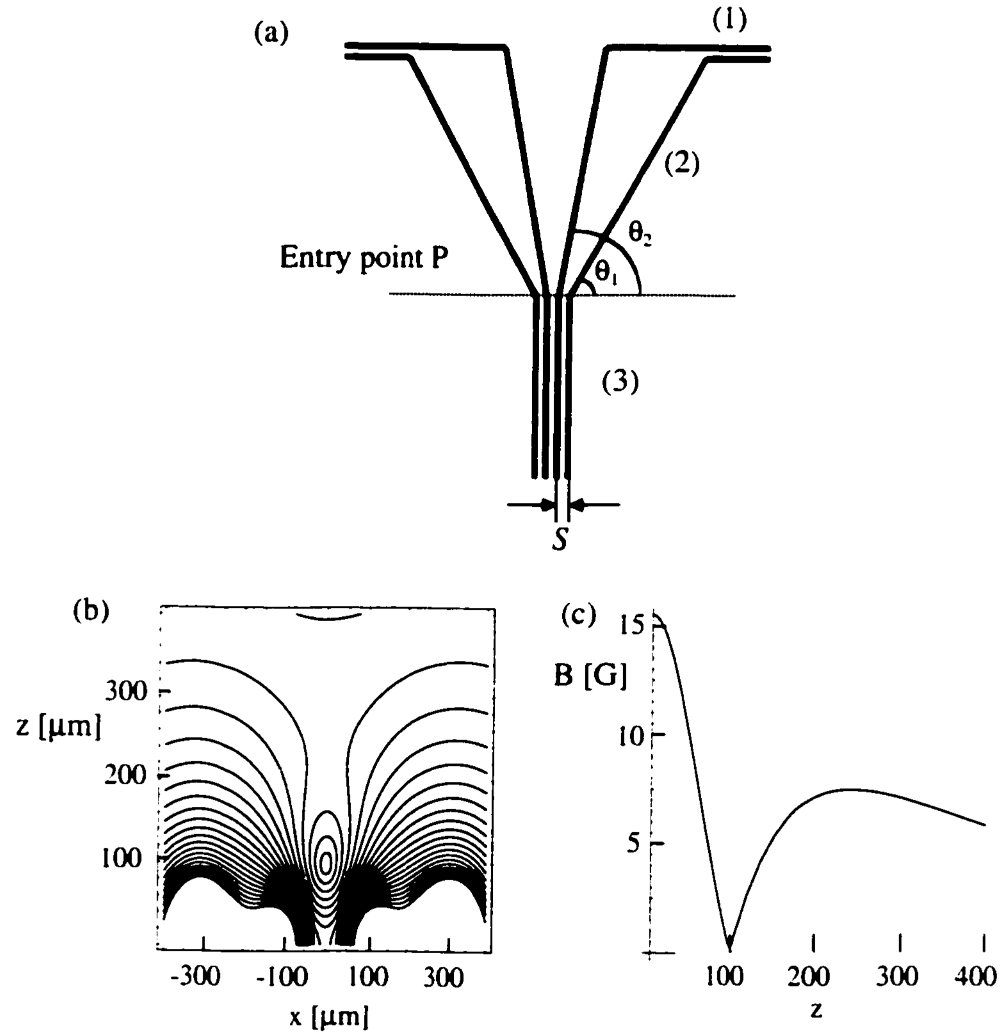

Figure 3.9. (a) Schematic diagram of a four-wire guide, where wires extend out with a funnel shaped geometry. It has three parts: (1) wires that go straight out to the pads that are perpendicular to incoming atoms, (2) funnel shaped part that connect to part (1), and (3) four straight wires that are parallel to incoming atoms. (b) Contour plot of magnetic field magnitude through entry point P. A minimum region is formed above a surface. (c) Plot of field magnitude through slice x = 0. The field minimum is formed at z = 100 µm.

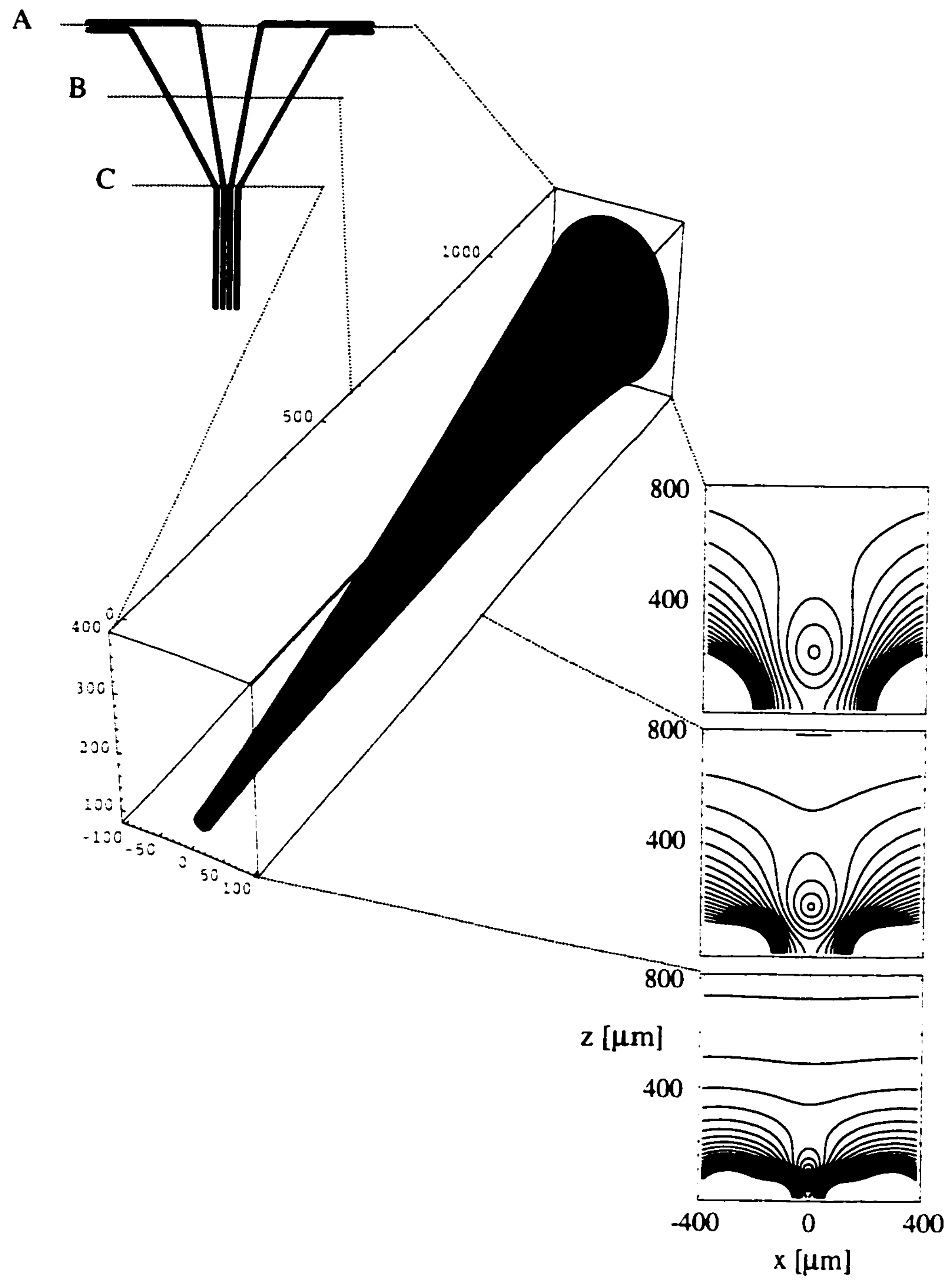

Figure 3.10. 3D plot of a magnetic field surface at constant magnitude $B = 2$ G as well as contour plots of field magnitude along the funnel shaped region. Through line A, magnetic trap with trap depth of ~ 2 G is formed, which has a trap area of 300 μm in z-direction and 200 μm in x-direction. Through line B, magnetic trap with trap depth of B ~ 3 G and trap area with ~ 260 μm in z-direction and 180 μm in x-direction is formed. The trap area continues to shrink while trap depth gets bigger as you move closer to the main guiding area. Through line C, the trap area is 150 μm in z-direction x 100 μm in x-direction, and the trap depth is B ~ 7.5 G.

calculations are done with wire widths w = 100 μm, center-to-center spacing of S = 200 μm, currents on outside wires I_{out} = 2 A, and currents on inside wires, I_{in} = 1 A. At the entrance of the guide, through line A, a magnetic trap with depth of B ~ 2 G is formed with a trap width of 300 μm in z-direction and 200 μm in x-direction.

Therefore, as evident from Fig. 3.10, atoms can be smoothly loaded and guided using funnel shaped wires. In the middle of the funnel-shaped region in Fig. 3.10, through line B, magnetic trap with depth of B ~ 3 G and trap width 260 μm in z-direction and 160 μm in x-direction is formed. The trap area continues to shrink while trap depth gets bigger as you move closer to the main guiding area. Through line C, the trap width is 150 μm in z-direction and 100 μm in x-direction, and the trap depth is B ~ 7.5 G. For this reason, all atom guides made in our group have been fabricated this way.

3.5. Experimental Setup and Results for Atom Guiding Experiment

In this section, we describe the experimental setup and discuss the experimental results for the atom guiding experiment [Dekker N.H., Thesis]. In the experiment, a micro-electromagnet guide fabricated on a silicon substrate, shown in Fig. 3.6, is used to guide atoms that are dropped from a MOT. The result is the first demonstration of guiding atoms using a microstructure fabricated on a substrate [Dekker N.H *et al.*, 2000]. Figure 3.11 shows schematic diagrams of the experimental setup used to demonstrate guiding of atoms using a micro-electromagnet guide, where top view is

(a) Top view

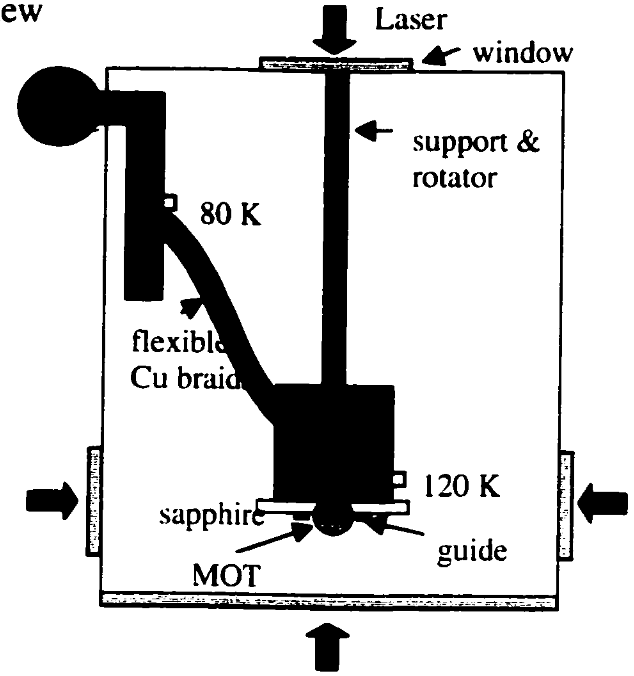

(b) Front view

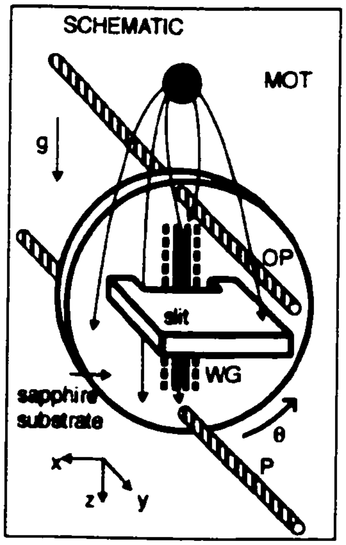

Figure 3. 11. (a) Top view of the schematic diagram of the experimental setup. The pressure of the vacuum chamber is ~ 10^{-9} Torr. The magneto optical trap (MOT) is formed right above the substrate by aligning six lasers and macroscepic magnetic field. (b) Front view of the schematic diagram of the experimental setup. MOT is produced approximately 1.5 cm above the sapphire substrate without clipping the laser beams. Small laser beam, OP, is placed at the entrance of the guide to optically pump the atoms to weak field seeking state. Another laser beam is placed at the exit of the guide to detect the atoms after they interacted with the guide. To avoid atoms that do not interact with the guide, a small stainless steel slit is mounted perpendicular to the sapphire substrate, where the slit has dimension of 5.5 mm in x-direction and 0.5 mm in y-direction.

shown in Fig. 3.11(a) and front view in Fig. 3.11(b). The experiment is carried out in ultra high vacuum chamber, where the pressure in the chamber is pumped down to ~ 10^{-9} Torr using a turbo pump. In order to reduce the resistance on the wires so that higher currents can run through the wires, the sapphire substrate is mounted on a copper cold finger, which extends to outside the vacuum chamber where it is cooled using liquid nitrogen. At thermal equilibrium, temperature of $T \sim 120$ K is measured near the sapphire substrate. Mechanical feedthrough is connected to the copper cold finger such that sapphire substrate can be rotated in either clockwise or counterclockwise directions at an angle θ. In the experiment, atoms are dropped from a MOT, which contains 10^8 cesium atoms at a density of 5 x 10^{10} atoms/cm^3.

The basic operating principle of the magneto optical trap (MOT) is described in following text. Six laser beams, which are detuned slightly below Cs ($6S_{1/2}$ to $6P_{1/2}$) transition frequency, cross each other in vacuum chamber. Because the laser frequency is detuned below the atomic transition frequency, atoms do not absorb the photon if the atom is stationary. If the atom is moving toward the laser beam, it will come to resonance with the laser and will absorb the photon due to Doppler effect. Atoms that absorb photons will slow down as momentum of the photon is transferred to the atom. Atoms moving in any direction will be slowed down, because there are six laser beams that slow down the atoms from all directions. A spring force, also necessary to trap the atoms, is provided by applying an inhomogeneous magnetic field, which is provided by anti Helmholtz coil configuration. The magnetic field is zero at the center of the trap, but increases in magnitude away from the center. The magnetic field induces a Zeeman shift in the atomic transition frequency, which causes the atoms to absorb more photons as they move away from the center of the trap. Hence, atoms are pushed back towards the center of the trap.

The cesium atoms are dropped from the MOT and cooled to a temperature of approximately 20 μK by polarization gradient cooling [Dalibard J. *et al.*, 1989] right after it is dropped from the MOT. The MOT should be formed close to the device by aligning the magnetic field and the laser, but because of the lead wires and the sapphire substrate, MOT was produced approximately 1.5 cm above the sapphire substrate without clipping the laser beams. Small laser beam, OP in Fig. 3.11(b), which is circularly polarized and tuned to both the $F = 3 \rightarrow F' = 4$ and $F = 4 \rightarrow F' = 4$ transitions, is placed at the entrance of the guide to optically pump the atoms to weak field seeking state $| F = 4, m_f = 4 >$. Another laser beam is placed at the exit of the guide to detect the atoms after they interacted with the guide. To avoid atoms that do not interact with the guide, a small stainless steel slit is mounted perpendicular to the sapphire substrate, where the slit has dimension of 5.5 mm in x-direction and 0.5 mm in y-direction.

Figure 3.12(a) shows the experimental data demonstrating the guiding of the atoms using a two-wire guide [Dekker N.H *et al.*, 2000]. The data were taken by scanning the probe beam below the output of the device in x-direction. For this data, the device was tilted at $\theta = 9.4 \pm 0.5$ degrees, current $I = 0.5$ A, and external magnetic field was applied in y-direction with magnitude $B_{ext} = 10$ G. There are three distinct traces: top two traces are with the guide on with the solid line positioned closer to the output of the guide than the position of the dotted line, bottom trace is with the guide off.

The absorption signal with the guide off varies slowly as a function of probe beam position, with the peak signal observed at 0 mm. The absorption signals with the guide

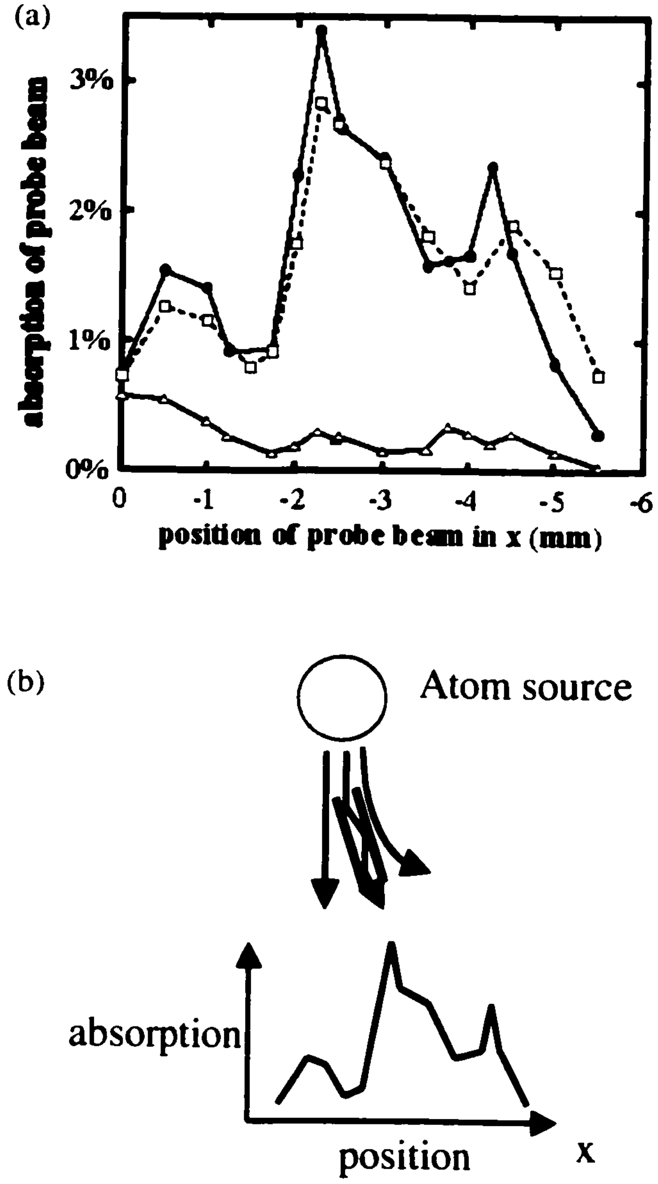

Figure 3. 12. (a) The experimental data demonstrating the guiding of the atoms using a two-wire guide [Dekker N.H *et al.*, 2000]. The data were taken by scanning the probe beam below the output of the device in x-direction. For this data, the device was tilted at $\theta = 9.4 \pm 0.5$ degrees, current $I = 0.5$ A, and external magnetic field was applied in y-direction with magnitude $B_{ext} = 10$ G. There are three distinct traces: top two traces are with the guide on with the solid line positioned closer to the output of the guide than the position of the dotted line, bottom trace is with the guide off. (b) Schematic diagram explaining three peaks shown in the data. The three peaks from right to left are due to (1) atoms that are deflected by the repulsive potential outside the guiding region, (2) atoms that are guided by the confining potential, and (3) atoms that are undeflected because they crossed through the guide field at the unstable equilibrium point between the guiding and repelling potentials.

on can be more than an order of magnitude larger than that with the guide off, which indicates that atoms have been guided with the device. For the data with the guide on, three distinct peaks are observed. This differs from the data with the guide off, where the number of collected atoms slowly decreases away from the center. Three peaks are located at approximately at $x = 0.8$ mm, $x = 2.3$ mm, and $x = 4.2$ mm. The maximum peak is at $x = 2.3$ mm. Such a spatial distribution can be explained with a schematic shown in Fig. 3.12(b). The three peaks from right to left are due to (1) atoms that are deflected by the repulsive potential outside the guiding region, (2) atoms that are guided by the confining potential, and (3) atoms that are undeflected because they crossed through the guide field at the unstable equilibrium point between the guiding and repelling potentials.

In this experiment, several other signatures of guiding are observed: (1) We verify over a range of 20° that the location of the guide output follows the angle θ of the guide to within 10%. (2) No atoms are observed below the guide output when the circularity of the optical pump beam is reversed to pump the atoms into strong-field seeking states, because these atoms are repelled from the field minimum. (3) As the temperature of the atom source is increased, guiding efficiency decreases because fewer atoms are confined by the guiding potential.

3.6. Nano-Electromagnet Interferometer for Atoms

In this section, we discuss a submicron sized micro-electromagnet interferometer for atoms that have been fabricated using electron-beam lithography, and propose a novel

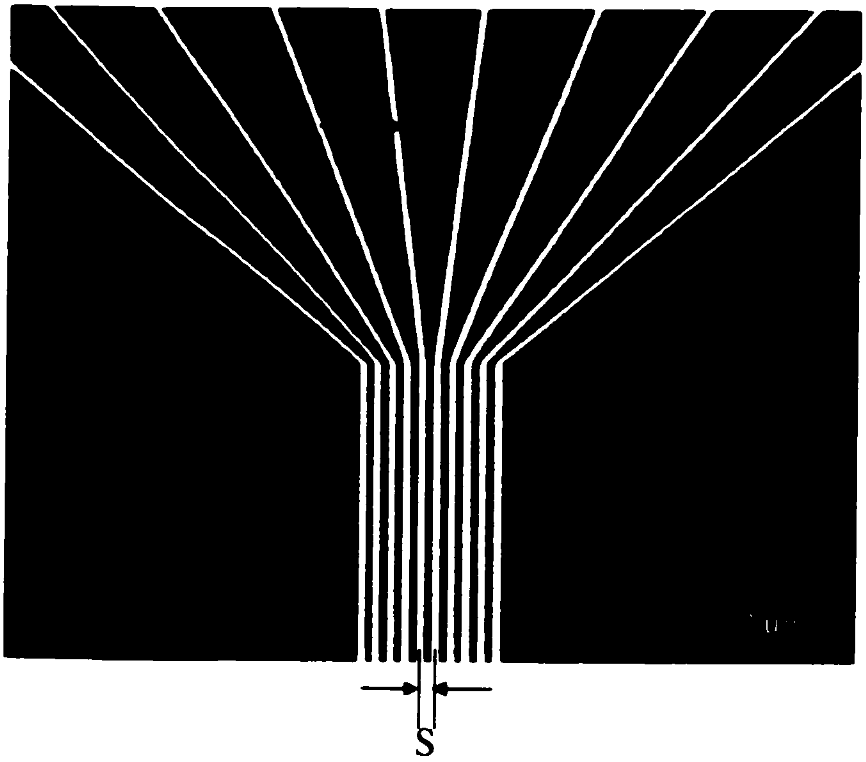

Figure 3.13. SEM image of an atom guide/interferometer. It consists of ten equally spaced wires, where each wire has a width of 200 nm and a height of 80 nm. The center-to-center spacing between two adjacent wires, denoted by *S*, is 400 nm.

way of constructing both a beam splitter and an interferometer for neutral atoms using a single micro-electromagnet device. By making a submicron sized device, it may be possible to propagate de Broglie waves in a single transverse mode in 1D or 2D, to make a controlled and coherent splitting of the wave function, and to realize a novel atom interferometer [Hinds, E.A. *et al.*, 2001]

Beam splitters and interferometers for neutral atoms have been suggested [Cassettari D. *et al.*, 2000], and experiments have been conducted to split a beam of atoms into two separate paths [Denschlag J. *et al.*, 1999; Mueller D. *et al.*, 2000; Folman R. *et al.*, 1999]. It was suggested that magnetic fields produced by "X" or "Y" shaped current carrying wires fabricated on substrates superimposed with external homogenous magnetic fields can create a minimum magnetic field that splits into two local minimum field regions. In the beam splitting experiment, "Y" shaped current carrying wire was used to split atoms as atoms traveling through single minimum sees two splitting potential minima at a point where wires split.

Figure 3.13 shows an SEM image of an atom guide/beam splitter/interferometer fabricated on a silicon substrate. It is a multi functional device, which consists of ten equally spaced wires fabricated using e-beam lithography, where each wire has wire width $w = 200$ nm and wire height $h = 80$ nm, which gives resistance per unit length $R/l = 1.4\ \Omega/\mu\text{m}$. More metals can be evaporated to increase the height of the wires if higher currents are desired. The spacing between adjacent wires is $S = 400$ nm. The complete fabrication procedure has been described in section 2.3.

The device works in many modes without the need of external magnetic fields: single channel guide, multi channel guides, beam splitter and an interferometer for atoms.

Although external magnetic fields can be applied to create guides for atoms as described in previous section, we focus on magnetic guides created only by the current carrying wires in this section. Self-complete devices are desirable when one is to build integrated atom optical devices on a single chip.

The single channel guide can be created when currents are applied to any combination of three to four wires as illustrated and explained in Figs. 3.4 and 3.5. For example, for a guide with four adjacent wires, wire spacing $S = 400$ nm with current $I = 8$ mA (corresponding current density $J = 5 \times 10^7$ A/cm^2) and $\alpha = 2$, a radial field gradient $\nabla B_{\min} = 400\ G/\mu m$ is produced near the minimum.

It is possible to create interferometers or beam splitters for atoms using the device shown in Fig. 3.13 by utilizing the time-dependent features of the device. Because magnetic fields in micro-electromagnets are produced by electric currents, the shape of magnetic fields can be changed rapidly and precisely. For the device shown in Fig. 3.13, the current time constant is $L/R \approx 1$ ps, with inductance $L \approx 0.1$ nH and resistance $R \approx 100\ \Omega$. Fast modulation of the magnetic field is an advantage of micro-electromagnets over permanent magnet structures, which require physical motion to generate time dependent fields.

Five magnetic field profiles are shown in Fig. 3.14 to illustrate how the device shown in Fig. 3.13 can work as a beam splitter and an interferometer for atoms. Figure 3.14(a) shows a single magnetic field minimum produced above a substrate with following currents: $I_4 = I_6 = 2$ mA, $I_5 = 1$ mA, and all others have zero current. I_1 through I_{10} are amount of currents that are applied through the wires from left to right for the device shown in Fig. 3.13. The single magnetic field minimum in Fig. 3.14(a) can be split into two regions of field minima in Figs. 3.14(b) to 3.14(e) by changing the current distributions on the wires. The splitting of atom paths must be done smoothly as atoms can lose their adiabaticity if the field changes abruptly.

The field profiles shown in Fig. 3.14 show how a single magnetic field minimum is slowly split into two field minima. The parameters used to produce magnetic field profiles shown in Fig. 3.14 are listed in the footnote[1]. Using these magnetic field profiles, atoms that travel along a single minimum may be split into two paths. Two minima can be separated as long as the device width. To realize an interferometer for atoms, two magnetic field minima are created initially, converged to a single field minimum, and it is split into two minima, all happening while atoms are traveling through the device. Atoms that enter into two separate paths interfere with each other when magnetic field minima are converged to one location, and they are then split into two paths. This method to manipulate the trajectories of atoms is powerful because we can create many different field configurations without having to alter the shape of the micro-electromagnets. Amount of currents to be supplied to each wire can be calculated, controlled and synchronized by a computer. The location and depth of these paths can be precisely controlled by adjusting the current distribution.

---

[1] (b) $I_3 = 6$ mA, $I_4 = 2.6$ mA, $I_5 = 0.488$ mA, $I_6 = 2.6$ mA, $I_7 = 6$ mA, (c) $I_3 = 6$ mA, $I_4 = 2.6$ mA, $I_5 = 0.488$ mA, $I_6 = 2.6$ mA, $I_7 = 6$ mA, (d) $I_3 = 2.5$ mA, $I_4 = 1$ mA, $I_5 = 1$ mA, $I_6 = 1$ mA, $I_7 = 2.5$ mA, (e) $I_2 = 3$ mA, $I_3 = 1.5$ mA, $I_4 = 1.5$ mA, $I_5 = 3$ mA, $I_6 = 1.5$ mA, $I_7 = 1.5$ mA, $I_8 = 3$ mA. Zero currents for all other wires unless specified as above.

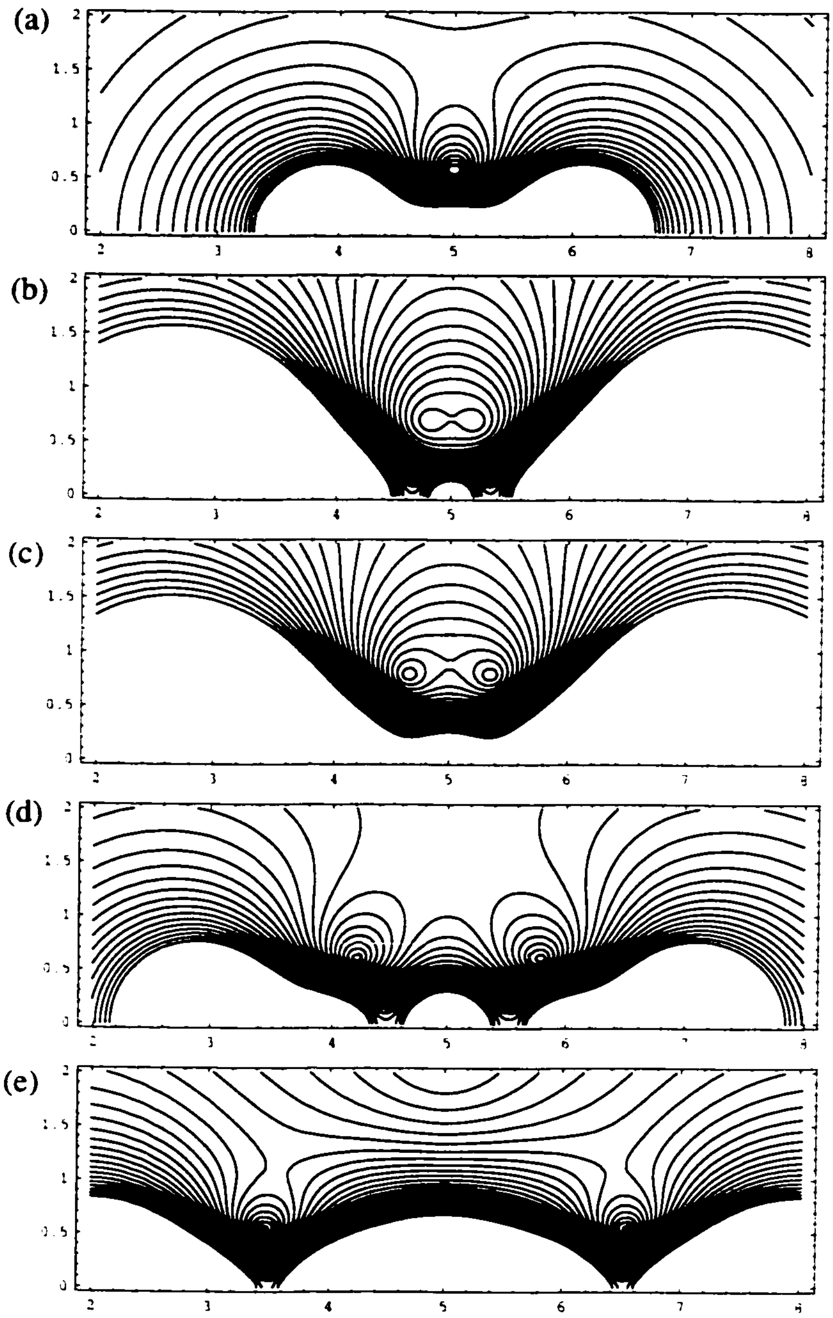

Figure 3.14. Five magnetic field profiles to illustrate how the device can work as a beam splitter and an interferometer for atoms. All magnetic fields are calculated for the device shown in Fig. 3.13. The currents used to produce plots are (a) $I_4 = I_6 = 2$ mA, $I_5 = 1$ mA, (b) $I_3 = 6$ mA, $I_4 = 2.6$ mA, $I_5 = 0.488$ mA, $I_6 = 2.6$ mA, $I_7 = 6$ mA, (c) $I_3 = 6$ mA, $I_4 = 2.6$ mA, $I_5 = 0.488$ mA, $I_6 = 2.6$ mA, $I_7 = 6$ mA, (d) $I_3 = 2.5$ mA, $I_4 = 1$ mA, $I_5 = 1$ mA, $I_6 = 1$ mA, $I_7 = 2.5$ mA, (e) $I_2 = 3$ mA, $I_3 = 1.5$ mA, $I_4 = 1.5$ mA, $I_5 = 3$ mA, $I_6 = 1.5$ mA, $I_7 = 1.5$ mA, $I_8 = 3$ mA. Zero currents for all other wires unless specified as above.

3.7. Summary

In conclusion, we have designed, fabricated and demonstrated a micro-electromagnet guide to control the trajectories of atoms above the surface of a substrate. By carefully designing the geometry of the current carrying wires, we have shown that the magnetic field profile can be optimized to load atoms into the device smoothly. By using a funnel shaped guide, which is the optimized geometry for an atom guide, we have experimentally demonstrated the guiding of atoms above a substrate.

We have also fabricated a nano-electromagnet guide/interferometer/beam splitter device and calculated magnetic field profiles that can be produced by the device. By utilizing time dependent feature of the device, it may be possible to create both interferometer or beam splitter for atoms using a single device.

Chapter 4

MAGNETIC NANOPARTICLE MANIPULATION USING MICRO-ELECTROMAGNETS

In this Chapter, we show how micro-electromagnets can be used to position and control magnetic nanoparticles. Micro-electromagnets consist of multiple layers of lithographically defined Au wires separated by transparent insulating polyimide layers fabricated on a substrate. Magnetic field peaks produced by current carrying wires on a substrate allow precise control and manipulation of magnetic nanoparticles with submicron spatial resolution. A micro-electromagnet matrix produces single peak or multiple peaks in magnetic field magnitude, which can trap, move and rotate magnetic nanoparticles. A matrix also produces electromagnetic fields to probe and detect the location of the particles. Micro-electromagnets are new tools to study and manipulate nanoparticles and biological entities. We describe the manipulation of magnetic particles using current-carrying wires as a novel way to trap, move and rotate these particles.

4.1. Introduction

With recent advances in the synthesis and growth of nanoscale particles in fluids, there has been a growing interest to study and control these nanoparticles. Magnetic nanoparticles and nanocrystal quantum dots have been grown in solution with excellent control, and their quantum characteristics have been studied [Alivisatos, A.P., 1996; Dinega, D.P. *et al.*, 1999]. Nanoscale Co bars and wires grown with high uniformity orient in an applied magnetic field. The quantized charge of a single semiconductor nanocrystal has been measured [Krauss, T.D. *et al.*, 1999] and the feasibility of nanocrystal quantum dot lasers has been demonstrated [Klimov, V.I. *et al.*, 2000].

Most experiments have used optical methods to test nanocrystals suspended in fluids. In order to study and explore the advantages of their quantum characteristics, methods to move, control and probe nanoparticles are needed. By precisely controlling the location of nanoparticles, it may be possible to construct arbitrary structures from these nanoparticles and make assembly of nanoparticles possible. The ability to move magnetic particles can be also important in biological and biomedical applications, for example to separate, manipulate and study cells and DNA that are attached to magnetic particles, in micron or nanoscale range. In addition, by attaching magnetic particles to nanocrystal quantum dots and nanotubes, it may be possible to manipulate them and to make hybrid circuits.

Motivated by these possibilities, we have developed micro-electromagnets consisting of multiple layers of lithographically patterned wires as a novel way to micromanipulate magnetic nanoparticles [Lee C.S. *et al.*, 2001]. High magnetic fields ($B \sim 0.1$ T) and high field gradients ($\nabla B \sim 10^4$ T/m) produced by micro-electromagnets allow precise control and manipulation of magnetic particles at room temperature, enabling the study of their motion and characteristics in a microscopic region.

Particular interest will be given to a micro-electromagnet matrix due to its versatility and importance. The matrix is a multi-layer structure that produces single peak or multiple peaks in magnetic field magnitude in microscopic region to trap and move objects that have magnetic moment, including ferromagnetic or superparamagnetic nanoparticles, magnetotactic bacteria, and magnetically tagged cells and macromolecules including DNA.

The matrix demonstrated in this Chapter has advantages for nanoparticle assembly: (1) Dynamic magnetic field profiles can be created in a matrix with each wire individually connected to a current supply. (2) Magnetic field peaks can be generated and individually moved continuously over the surface with spatial resolution much less than the wire spacing. By making a matrix with submicron wire spacing, the spatial resolution can be as small as ~ 100 nm. (3) Two or more magnetic field peaks can be generated simultaneously and can be moved independently. (4) A matrix is an integrated device on a chip, where optical tweezers [Ashkin A. *et al.*, 1986] and magnetic tweezers [Haber C. and Wirtz D., 2000] require a sophisticated and large setup to operate. The matrix also could be very useful in the manipulation of biological entities to study and examine their physical properties and characteristics. As an example, a matrix may be used to measure a tensile strength of DNA and to study the formation of supercoils in DNA by attaching magnetic particles to ends of a DNA strand.

In this Chapter, we describe in detail the use of micro-electromagnets to trap, move and assemble magnetic nanoparticles suspended in fluid above a chip at room temperature. Specifically we report the computed magnetic field profiles of a ring trap (section 4.2) and a matrix (section 4.3), and the demonstration of two-dimensional manipulation of superparamagnetic particles (section 4.4 and 4.5).

4.2. Ring Trap

Figure 4.1 shows a schematic diagram and a micrograph of a ring trap. A ring trap consists of a single circular current-carrying wire with an insulating layer on top. A single magnetic field peak is produced at the center of the circular wire above an insulating layer as current flows through the device. As illustrated in Fig. 4.1(a), magnetic field lines produced by a ring trap go into or out of the surface depending on the direction of the current flow. The ring trap shown in Fig. 4.1(b) has wire width $w = 10$ μm, wire height $h = 3$ μm, radius $r = 35$ μm and thickness of an insulating layer $t = 30$ μm. A ring trap can be used as a single trap for magnetic particles as magnetic particles are attracted to the maximum in the magnetic field magnitude.

Figure 4.2 shows a contour plot and a three-dimensional (3D) plot of computed magnetic field magnitude for the ring trap shown in Fig. 4.1. The thickness of the insulating layer is adjusted to optimize the shape of the magnetic field peak. If the insulating layer is too thin, the field is the strongest right above where the wire is patterned and magnetic particles are attracted to the wires, not to the center of the circle. If the insulating layer is too thick, the magnetic field is weak and the gradient is too small to trap any particles. This is evident from Fig. 4.2(a), where the contour lines of magnetic field magnitude for the ring trap shown in Fig. 4.1(b) are calculated and plotted. Magnetic field produced by a ring trap is solved numerically starting from Biot-Savart law. We deduce from the plot that the magnetic field profile is optimized when the thickness of the insulating layer is about the same as the radius of the circle, i.e., $t \sim r$. Figure 4.2(b) shows the 3D plot of the magnetic field magnitude at $t = r$. The magnetic

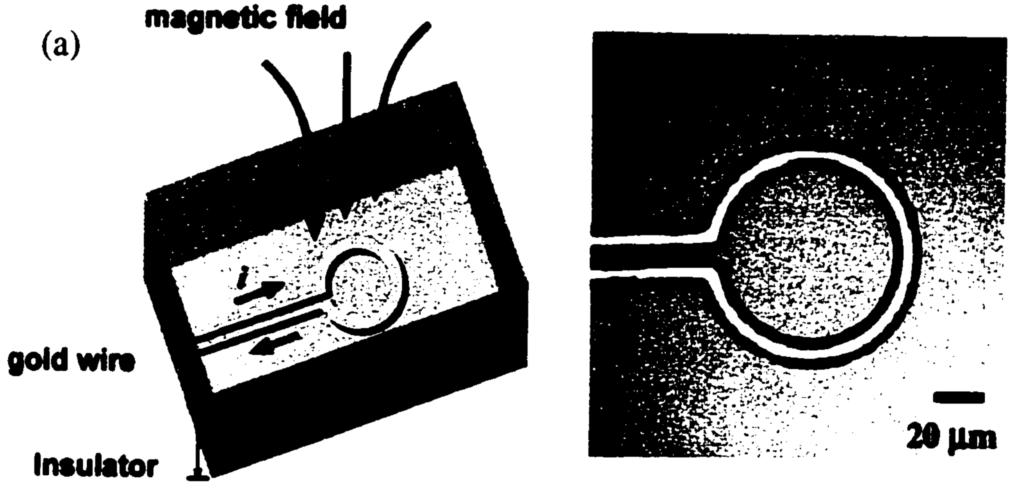

Figure 4.1. (a) Schematic diagram of a micro-electromagnet ring trap. *i* indicates the direction of current flow. (b) Micrograph of a fabricated ring trap. It has width of 10 μm, height of 3 μm, and radius of 35 μm. An insulating layer is spun on top, which has thickness of 30 μm. Ring trap produces single peak in magnetic field magnitude on the center of the surface of the insulating layer.

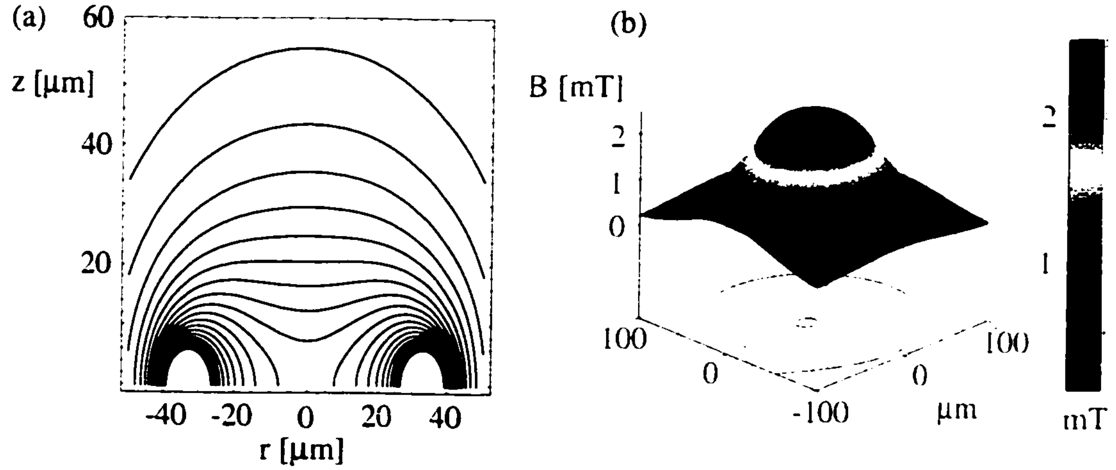

Figure 4.2. (a) Contour lines for the computed magnetic field magnitude for a ring trap with radius *r* =35 μm. (b) Three-dimensional plot of magnetic field magnitude at *t* = *r*.

field magnitude at the center of the ring trap above t is given by

$$B = 0.5\mu_o I \frac{r^2}{(r^2 + t^2)^{3/2}}.$$

The field gradient near the center is then given by

$$\frac{\partial B}{\partial r} \cong \mu_o I \frac{r}{(r^2 + t^2)^{5/2}} (t^2 - \frac{1}{2} r^2).$$

For the ring trap shown in Fig. 4.1(b), $B = 8$ mT with $\nabla B = 60$ T/m is produced on the center of the ring trap for a current $I = 1$ A. For $I = 1$ A, $B = 0.1$ T is produced on the surface of the wire.

4.3. Micro-electromagnet Matrix

A micro-electromagnet matrix can trap, move and rotate magnetic nanoparticles by producing sharp magnetic field peaks in magnitude that can easily change their positions on a two-dimensional surface. A schematic and a micrograph of a matrix are shown in Figs. 4.3(a) and 4.3(b) respectively. A matrix consists of two layers of current-carrying Au wires, separated by an insulating layer, with an additional insulating layer on top. Insulating layers are used in multi-layer structures to prevent electrical shorting between wires, and between wires and the solution containing magnetic particles. As mentioned in earlier section, the thickness of insulating layers is important to generate optimum magnetic field profiles. The fabrication procedure to construct a matrix was described in detail in section 2.2.

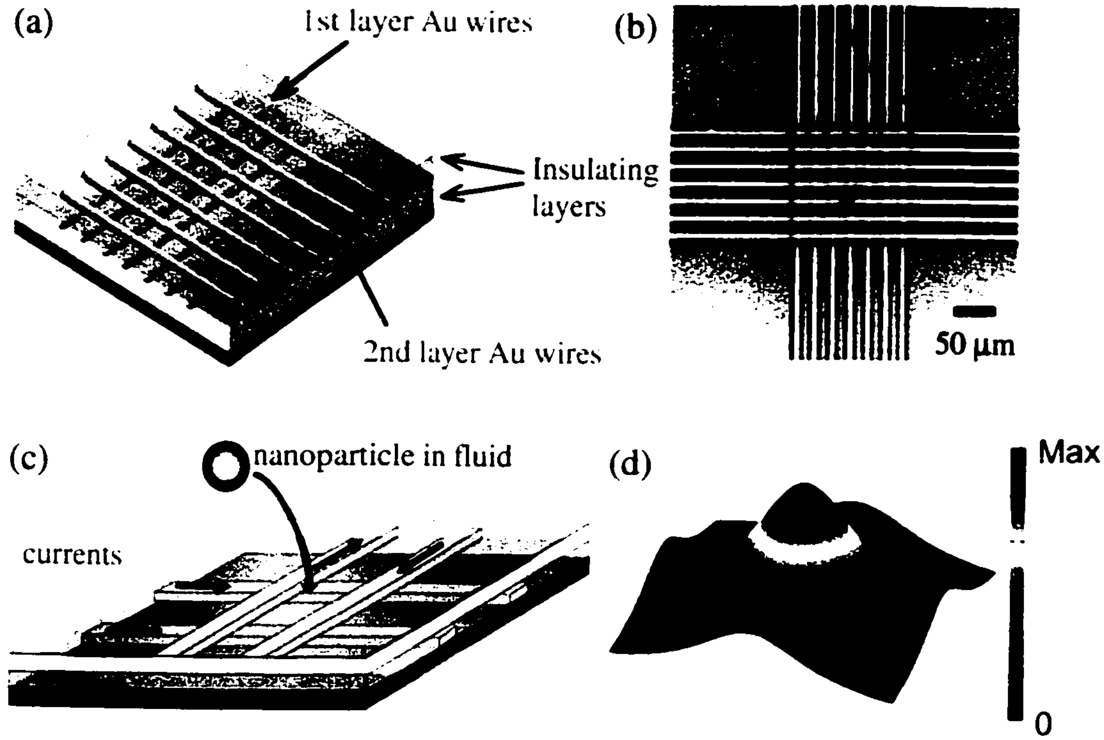

Figure 4.3. (a) Schematic diagram of a micro-electromagnet matrix. The matrix consists of two layers of current carrying conductors with two layers of insulators. (b) Micrograph of a fabricated matrix (7x7wires). Each wire has a width of 10 µm, height of 3 µm, and center-to-center spacing between wires is 20 µm. (c) Operating principle of the matrix. Magnetic particles are attracted to the field maxima formed by current carrying wires. (d) Computed magnetic field profile with current distribution shown in (c). Single magnetic field peak is produced as a result.

The operating principle of magnetic particle manipulation by micro-electromagnets is illustrated in Fig. 4.3(c). The peak in magnetic field magnitude produced by the current carrying wires attracts magnetic particles to maxima in the field magnitude. Magnetic dipole interaction between the magnetic field produced by the wires and the particle's magnetic moment pulls the magnetic particles to desired locations. The interaction potential energy is $U = -\vec{m} \cdot \vec{B}$ where $\vec{m}$ is the particle's magnetic moment and $\vec{B}$ is the magnetic field. The field magnitude B scales with the characteristic size d of the wire as $B \propto I/d$, the field gradients as $\nabla B \propto I/d^2$, and the current as $I \propto d$. Thus, larger gradients can be produced for smaller devices. The wire size for the devices shown in Fig. 4.3(b) is 10 x 3 μm^2. For the matrix reported here, current densities 10^7 A/cm^2 can be achieved at room temperature, yielding $B \cong 0.1$ T and $\nabla B \cong 5$ mT/µm. Improvement in ∇B is possible if the devices are made with submicron sizes by using e-beam lithography. This is described in Chapter 6 when we discuss the manipulation of single nanoparticles using nano-electromagnets.

Localized electromagnetic fields can be generated by micro-electromagnets to perturb and sense their response of nanoparticles. Examples are Nuclear Magnetic Resonance (NMR) and Electron Spin Resonance (ESR). Due to their small size and their geometry, micro-electromagnets are able to generate ac magnetic fields at rf and microwave frequencies in a small volume containing a single nanoparticle or group of nanoparticles, and the response of the magnetization inside the nanoparticle can be tested.

The strength of the trap can be estimated for ferromagnetic, superparamagnetic and paramagnetic particles. The condition for controlling magnetic particles using micro-electromagnets is that the potential energy produced by a micro-electromagnet is greater than the thermal energy of the particle, i.e., $U > k_BT$, where k_B is the Boltzmann constant and T is the absolute temperature. For a ferromagnetic particle, the potential energy is $U = -MVB$, where M is the magnetization of the particle, V is the volume of the particle and B is the magnitude of the magnetic field. For a superparamagnetic particle, the direction of the magnetization does not align with the magnetic field, but fluctuates around it due to the thermal motion. Hence, the potential energy is $U = -\langle M\rangle VB$, where $\langle M\rangle$ is the average magnetization due to thermal fluctuations. $\langle M\rangle$ can be written as

$$< M > \; = \frac{\int M \exp[MVB\cos\theta / k_BT]\cos\theta\sin\theta d\theta d\phi}{\int \exp[MVB\cos\theta / k_BT]\sin\theta d\theta d\phi},$$

where θ is the angle between the applied magnetic field and the magnetic moment of the particle. By simplifying the integral, we get

$$< M > \; = M\left[\coth\left(\frac{MVB}{k_BT}\right) - \frac{k_BT}{MVB}\right].$$

The blocking energy of a particle depends on the size, shape and the anisotropy energy of the particle. For a paramagnetic particle with magnetic moment $m = (\chi B/\mu_0)V$, where χ is the magnetic susceptibility, V is the particle volume, and μ_0 is the permeability of free space, the potential energy is $U = -mB = -(\chi B^2/\mu_0)V$. The minimum size of a paramagnetic particle that can be trapped is $V \geq (3/2)k_BT\mu_0/\chi B^2$.

It is possible to estimate the minimum size of a particle that can be trapped using a micro-electromagnet. Trapping condition, $U > k_BT$, yields the volume of the smallest magnetic particle that can be trapped, which is $V \geq k_BT/(M_SB)$, where M_S is the saturation magnetization of the particle. From this relation, we have calculated the minimum radius

Substance	Fe	Co	Fe_3O_4	CrO_2
Minimum radius (nm)	3.8	4.1	5.9	5.8

Table 4.1. Minimum radius that can be trapped using a micro-electromagnet for B = 10 mT at room temperature for various particles, assuming the particles are spherical.

of a spherical particle that can be trapped for B = 10 mT at room temperature and the results are listed in Table 4.1.

A matrix is a versatile device and it can operate in many different modes. The first thing it can do is to generate single magnetic field peak at any position above the surface and to move its peak from one position to another with a spatial resolution much less than the spacing between two adjacent wires. This ability is illustrated in Fig. 4.4, which shows computed magnetic field profiles for two matrices that have two different numbers of wires. Figure 4.4(a) shows how a single peak in field magnitude can trap and move strong field seeking magnetic particles continuously over the matrix with spatial resolution less than the wire spacing. The magnetic field peak was calculated with a matrix of 8x8 wires and the currents in the wires were adjusted to approximate a Gaussian peak in field magnitude at each peak position. Figure 4.4(b) shows the same calculation, but with 16x16 wires. It is clear how adding wires can improve the shape of the peak as more wires contribute to the formation of the peak, making it possible to precisely control the shape and the location of each peak.

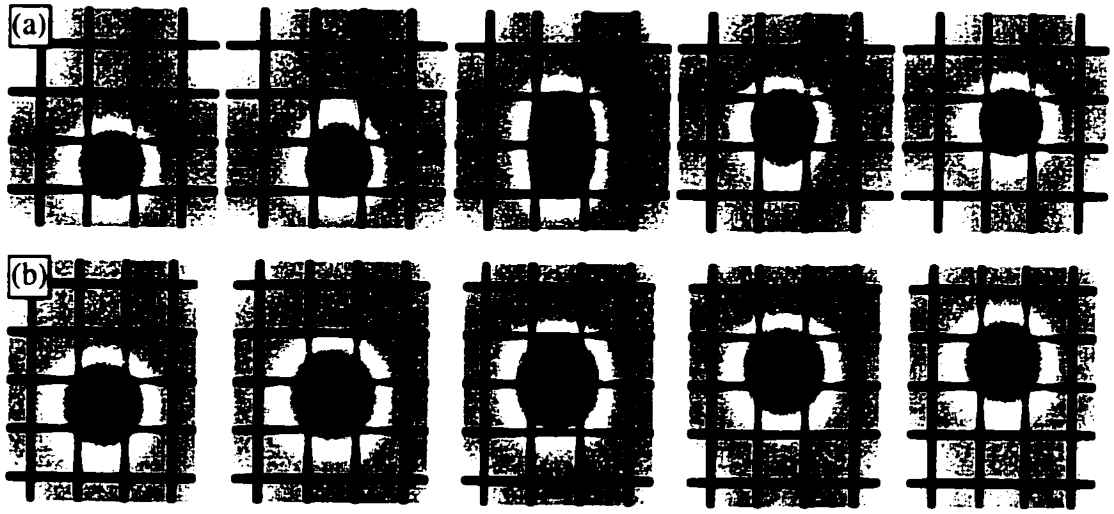

Figure 4.4. (a) Simulation of a moving peak in field magnitude produced by 8x8 wire matrix; the solid lines show wire positions. Currents were adjusted to approximate a Gaussian magnetic field peak. The peak moves continuously between two adjacent wires, with steps less than the wire spacing, but the peak deformation occurs above a wire. (b) Same simulation as in (a) but with a 16x16 wire matrix. By adding more wires, the peak deformation disappears and the peak moves more smoothly across the wires.

A matrix can produce two or multiple peaks simultaneously and move their peak positions independently from each other. For example, Fig. 4.5 shows a variety of magnetic field profiles that can be produced using a matrix. All calculations were done using a 16x16 wire matrix. Figure 4.5(a) shows how two separate magnetic field peaks can be produced and moved diagonally to converge at one position. Two peaks can be formed at any position above the surface and moved continuously. This profile could be used to bring two nanoparticles together for particle assembly or biological entities can be captured at two separate locations and brought in together and the matrix can be used to study how they interact in micron- or nano scale. By making a matrix with submicron wire spacing, it may be possible to trap and move a single nanoparticle suspended in a fluid to a desired position equipped with electrical leads or sensors and study its characteristics.

Figure 4.5(b) shows how a magnetic field peak is fixed at a position while another peak rotates around it. The picture shown on the far right is the overlay of the peak movement for a revolution of one cycle in steps of $\Delta\theta = 30°$. Figure 4.5(c) shows how four magnetic field peaks can be produced simultaneously and moved and converged at one position with the overlay of the entire movement shown on the right. A letter "H" is produced by moving four magnetic field peaks.

Where it can be very difficult to create traps in more than two positions simultaneously using optical tweezers or magnetic tweezers, multiple traps can be easily created using a matrix. Because each wire in a matrix can carry a different current, many magnetic field profiles can be created by changing the currents on the wires.

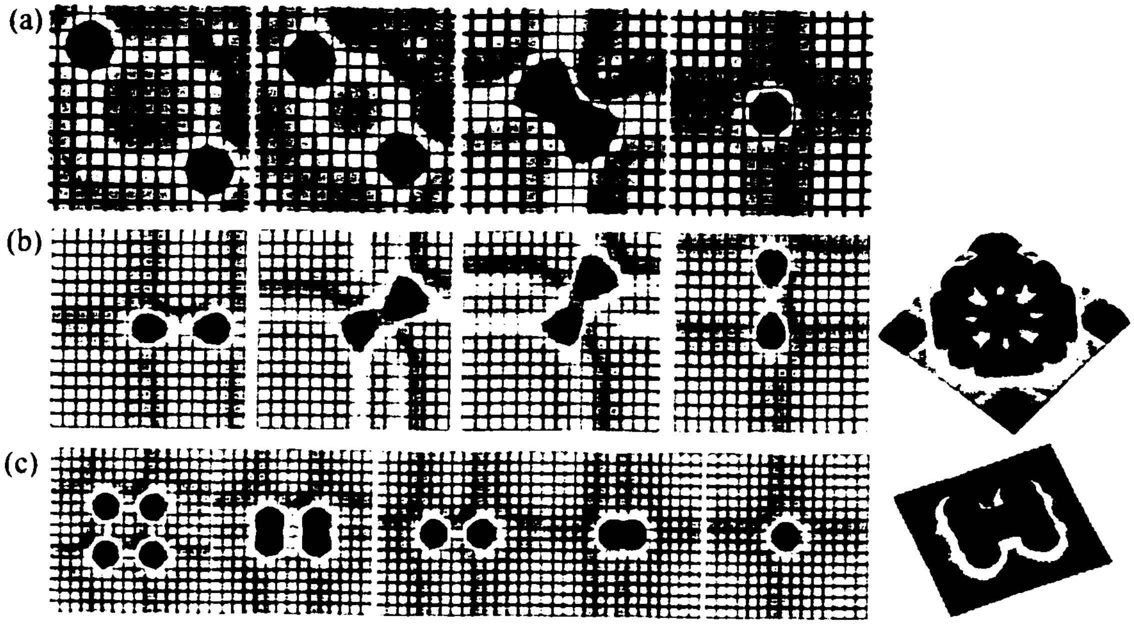

Figure 4.5. (a) Simulation of two separate peaks in magnetic field magnitude, which move diagonally and join at one position. (b) Simulation of two separate peaks in magnetic field magnitude, where one peak is fixed at a position while another peak rotates around it. Overlay of full rotation is shown on the right. (c) Simulation of four separate peaks in magnetic field magnitude, where those peaks are converged and joined at one position. Overlay of full motion is shown on the right. A letter "H" is produced by moving four peaks simultaneously.

The discussions thus far have been limited to static magnetic fields that are produced by applying dc currents on the wires. We now discuss the effect of ac field on these magnetic fields, using one of the Maxwell's equations

$$c^2 \nabla \times \bar{B} = \frac{\bar{j}}{\varepsilon_0} + \frac{\partial \bar{E}}{\partial t},$$

where j is the current density, ε_0 is the permittivity of free space, c is the speed of light, and $\bar{E}$ is the electric field. This law states that the line integral of the electric field around any closed path equals the rate of change of magnetic flux through any surface area bounded by that path [*Physics for Scientists and Engineers*, 1990]. Using this equation, we can estimate frequency range, where ac electric field becomes important in the calculation of magnetic field peaks.

Figure 4.6 shows the schematic diagram of a simple model, where two parallel plates are charged up by applying ac voltages on these plates [See discussion on *The Feynman Lectures on Physics Vol. 2*, 1966]. For this model, current $I = 0$, and the first term on the right side of the equation vanishes. Oscillating electric field is produced between two plates, where this electric field induces magnetic field. We expect that the induced magnetic field would encircle in the way that is shown in Fig. 4.6 because the induced magnetic field should be normal to the electric field. By integrating the Maxwell's equation shown above, we obtain

$$c^2\, 2\pi r B = \int \frac{\partial \bar{E}}{\partial t} \cdot d\bar{a},$$

where r is the radius of the circle. For two parallel plates, $E = V/d$, where d is the separation between two plates. Assuming that the applied voltages are sinusoidal with frequency f, i.e., $V = V_0\, exp[-i(2\pi f)t]$, we obtain, in magnitude,

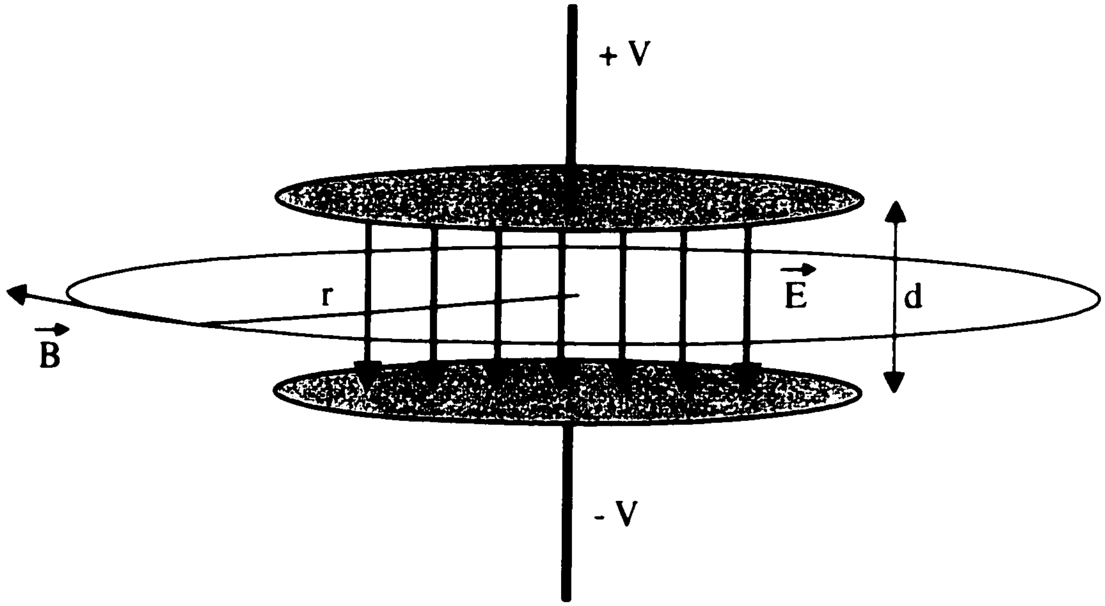

Figure 4.6. Schematic diagram of two parallel plates that are charged up by applying ac voltages. Oscillating electric field is produced between two plates, and this electric field induces magnetic field. The induced magnetic field would encircle in the way that is shown, which should be normal to the electric field. The circle has radius *r*, and area *A*. Two plates are separated by distance *d*.

$$c^2 \mu_0 I = \frac{A}{d}(2\pi f)V_0$$

where A is the area enclosing the circle. Two parallel plate approximation is valid because in a matrix, wires are perpendicularly stacked up and they cross each other. For the matrix shown in Fig. 4.3(b), the area where two wires cross is $A = (10\ \mu\text{m})^2$, separated by distance $d = 5\ \mu\text{m}$. Using these values, the relation is obtained, which gives the magnetic field induced by ac electric field that equals the magnetic field produced at a distance r by a current carrying wire with current $I = 1$ A,

$$f V_0 = 10^{15}.$$

With ac voltage with amplitude of 150 V, which corresponds to a breakdown voltage in air ($V_0 = 30$ V/μm), frequency $f = 6.7$ THz needs to be applied to the wires in order to obtain the same magnetic field magnitude as a current carrying wire with current $I = 1$ A at distance r. Therefore, ac voltages practically do not change the magnetic field profiles produced by current carrying wires.

4.4. Demonstration of Magnetic Particle Manipulation

Experiments to trap and move magnetic particles using micro-electromagnets were done using commercially available "magnetic microspheres"[1]. Magnetic microspheres contain magnetite, iron oxide (Fe_3O_4), crystals of ~ 1 to 20 nm, which are dispersed in styrene or styrene/divinylbenzene monomers and polymerized. Particles have mean diameters of ~ 0.35 to 2.5 μm and contain approximately 12, 20, 40 or 60% of

---

[1] Magnetic microspheres used in the demonstration were purchased from Bangs Laboratories, Inc, 9025 Technology Drive, Fishers, IN. 46038. Tel: 800-387-0672, Fax: 317-570-7034. http://www.bangslab.com

magnetite in mass inside the polymer. In our experiment, magnetic microspheres with mean diameter of 2.29 μm with 21% magnetite crystals in mass (Bangs Lab product number: ME01N/3240) were used. Because the densities are low (~1.1 to 2.2 g/cm^3) and magnetite crystals are encapsulated in a thick polymer, microspheres remain well dispersed in solution.

Magnetic microspheres are superparamagnetic and possess negligible magnetic remanence and hysteresis. Therefore, microspheres are magnetized when magnetic field is applied, but fully demagnetize when the field is removed. This makes it easy to separate the particles from the liquid phase by applying magnetic field, and they can be redispersed without clumping by removing the field. In addition, the surface of these particles can be functionalized such that biomolecules can be easily attached. For example, streptavidin-coated magnetic microspheres are attached to biotinylated DNA [Strick T.R. *et al.*, 1998]. Because of these properties, magnetic microspheres are widely used in the study of both cells [Fabry B. *et al.*, 2001] and DNA [Smith S.B. *et al.*, 1992; Strick T.R. *et al.*, 1998].

In the experiment, a drop of fluid containing magnetic microspheres was dispensed on the micro-electromagnet, either a ring trap [Fig. 4.1(b)] or a matrix [Fig. 4.2(b)]. Current was supplied to the micro-electromagnets from either a commercial power supply (ring trap) or a group of 14 bipolar current sources controlled by a computer (7x7 wire matrix). For the ring trap demonstrated, current amount less than 0.5 A was applied, which gives peak magnetic field less than 4 mT. For the matrix, currents less than 0.1 A were applied to wires in the top layer and currents less than 0.3 A to the wires in the bottom layer. The peak magnetic field above the matrix for these conditions was less than 4 mT. The motion of nanoparticles was observed using an optical microscope equipped with a digital camera (Nikon Coolpix 850) and the images were downloaded to a computer.

The trapping of magnetic microspheres using a ring trap is demonstrated in Fig. 4.7. Figure 4.7(a) shows magnetic microspheres that are randomly distributed when they are dropped on a ring trap without magnetic field. The density of particles is clearly small. These particles are immediately pulled in and trapped to the center of the ring trap when the field is turned on as shown in Fig. 4.7(b). Current of 0.35 A was applied to the device, which gives magnetic field magnitude of 2.7 mT at the center of the ring trap. The image was taken ~ 30 seconds after field was applied.

Figure 4.8 shows the operation of a micro-electromagnet matrix to move a group of magnetic microspheres continuously over (a) short distances comparable to the wire spacing, (b) longer distances, and (c) to move two groups of particles together and join them into a single larger group. These figures demonstrate that a matrix can build larger objects in two dimensions from nanoparticles, an ability that can be used to assemble custom designed nanostructures. An important ability of a matrix is to move nanoparticles continuously over distances smaller than the wire spacing. This ability is demonstrated in Fig. 4.8(a). The continuous motion of magnetic particles in Fig. 4.8(a) by increments less than the wire spacing is in agreement with the continuous motion of the magnetic field peak shown in Fig. 4.4. Note that the size of the particle group is broadened above a wire in both experiment and theory. Figure 4.8(b) shows that a matrix can move a group of particles over a longer distance, four wire spacing for this case.

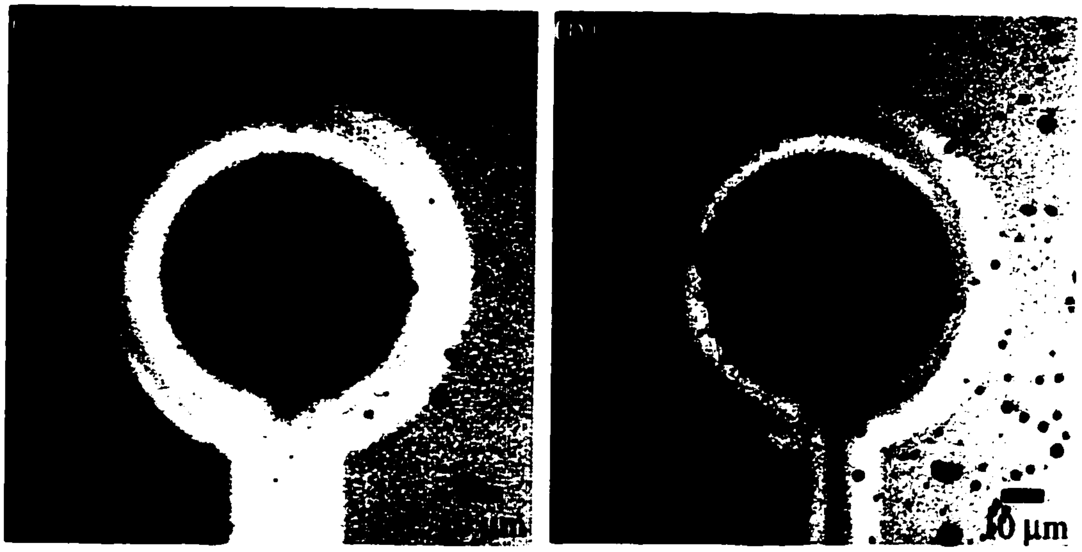

Figure 4.7. Micrograph of magnetic microspheres in fluid above (a) a ring trap with no current and (b) I = 0.35A. The particles are 1 to 20 nm magnetite nanoparticles coated with a polymer composed of polystyrene and carboxylic acid, suspended in water based solution; the coated particle diameters are 1 to 2 μm. A spherical magnetite nanoparticle with 10 nm diameter has magnetic moment ~ $10^5\mu_B$. The current $I = 0.35$ A in (b) produces a magnetic field peak $B = 2.7$ mT at the center of a ring trap above the insulating layer.

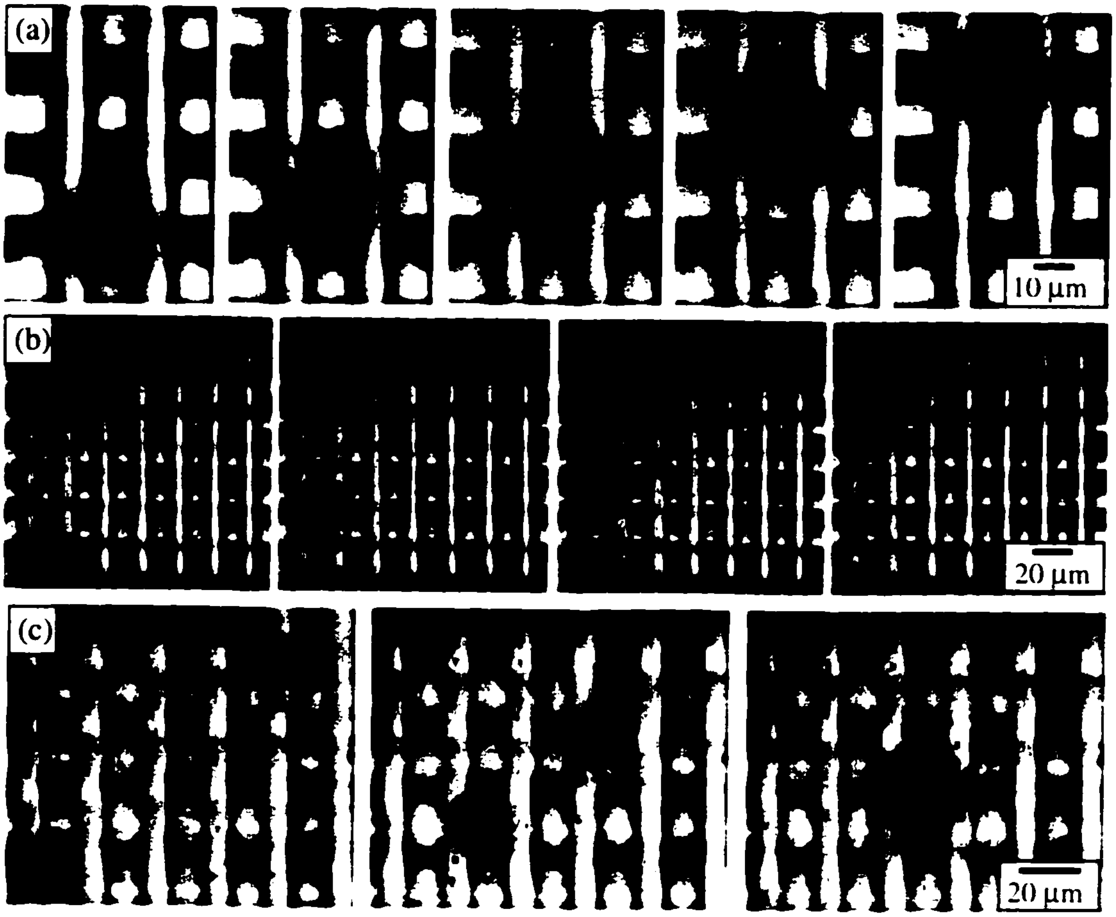

Figure 4.8. (a) Demonstration of moving a group of superparamagnetic particles over two wires of a micro-electromagnet matrix. The wire currents were adjusted to continuously move particles by increments less than the wire spacing. The size of particle group is broader above the wire in agreement with the simulation in Fig. 2(b). (b) A group of particles is moved vertically by the matrix over a longer range of four wire spacing. (c) Two groups of particles are moved diagonally to join in a single location. Particles can be moved diagonally at any angle. These experimental results agree well with the motion of peaks of magnetic field magnitude shown in Figs. 4.4 and 4.5. Current was passed through all fourteen wires for the demonstrations shown in the figure.

Together, Figs. 4.8(a) and 4.8(b) demonstrate that the matrix can move and precisely locate magnetic nanoparticles anywhere on its surface.

In Fig. 4.8(c), the matrix simultaneously moves two groups of particles diagonally and joins them into a single large group of particles, in agreement with the motion and joining of two peaks in magnetic field shown in Fig. 4.4(a). Moving magnetic beads along a line has been recently demonstrated using a single layer micromagnetic system [Deng, T. *et al.*, 2001]; the device requires an external magnetic field and the particles move in steps of several hundred microns.

Although all magnetic field calculations shown thus far have used dc currents, a matrix can also operate in another mode by applying ac currents to the wires. A matrix can generate a rotating magnetic field over a surface utilizing time-dependent control of the currents. This property can be used to rotate magnetic particles above a surface at μm distances. Instead of using many wires at the same time, only two wires are needed to make a magnetic motor. Figure 4.9(a) illustrates how a matrix generates a rotating magnetic field above an insulating plane. To generate a rotating magnetic field, ac currents are applied to two wires that are perpendicular to each other. Each wire carries sinusoidally modulating current with frequency f with amplitude I_0, but with phase difference of 90 degrees between them. With this current distribution, the resulting magnetic field rotates either in clockwise or counterclockwise direction with frequency f above an insulating plane. For the current configuration shown in Fig. 4.9(a), the magnetic field rotates in clockwise direction.

The computed magnetic fields are shown in Fig. 4.9(b) for a revolution of one cycle, where red arrows indicate the direction of the magnetic field and the contour lines

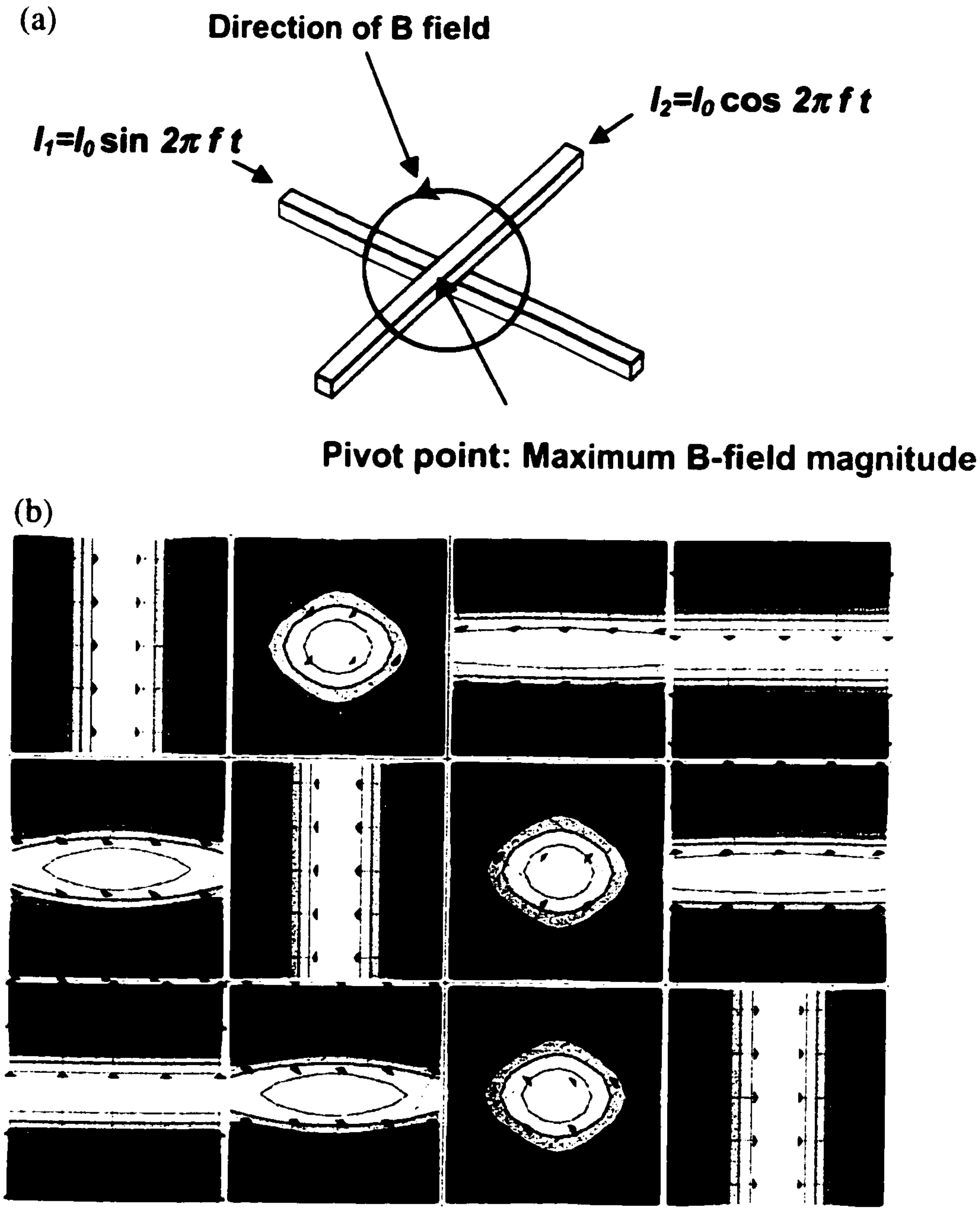

Figure 4.9. (a) Illustration of how a matrix generates a rotating magnetic field. AC currents applied to two perpendicularly aligned wires result in generation of rotating magnetic field. (b) Computed magnitude and direction of the magnetic field. Red arrows indicate magnetic field direction and the contour lines indicate field magnitude. The field direction rotates continuously in clockwise direction while the magnitude is kept maximum above where two wires cross.

show its magnitude. The magnetic field produced by two wires on the insulating layer is given by

$$\bar{B} = \frac{\mu_o I_o}{2\pi h}\hat{\varphi},$$

where h is the height of an insulating layer and $\varphi = 2\pi f t$ in degrees (angle). The direction of the magnetic field rotates continuously on the plane of the insulating layer, while the magnetic field magnitude is kept maximum right above where two wires cross. This is the pivot point where magnetic particles rotate around.

Figure 4.10 shows a demonstration of the rotation of magnetic particles using a matrix. In this demonstration, ferromagnetic iron particles with ~2 μm in size are used instead of superparamagnetic particles. The body of a superparamagnetic particle does not rotate under changing field direction because its magnetic moment relaxes to the direction of the field before its body can rotate and align to the field direction. Iron particles are prepared by putting small amount of fine iron powders into distilled water. A drop of water containing these particles is dispensed on the surface of the matrix.

As soon as ac currents are applied to two perpendicular wires, iron particles are attracted and assembled above where two wires cross, and they start rotating immediately. Iron particles are shown to rotate in clockwise direction in agreement with the calculation shown in Fig. 4.9. For the matrix, the current time constant is $L/R = 0.1$ ns, with inductance $L \approx 1$ nH and resistance $R \approx 10\ \Omega$. Therefore, magnetic field can rotate as high as in GHz range. For the demonstration shown in Fig. 4.10, iron particles have been shown to rotate at 3 Hz (180 rpm). Because the rod shaped particle shown in Fig. 4.10 consists of many smaller iron particles that are aggregated due to attractive magnetic forces between them, particles break up at higher speed. In addition,

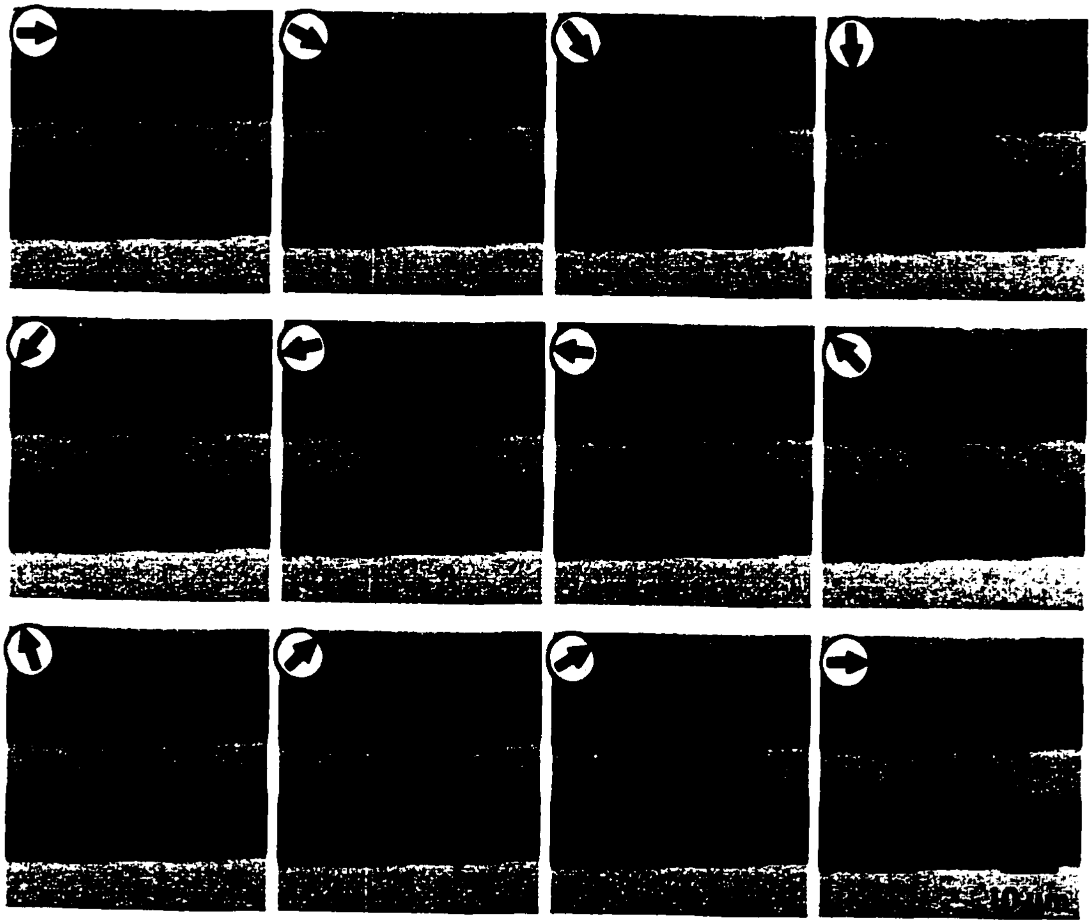

Figure 4.10. Demonstration of rotating iron particles by applying AC currents to two wires that are perpendicular to each other. Ferromagnetic iron particles were used for the demonstration, where they are shown to align with the rotating magnetic field. Iron particles are rotated in clockwise direction. The red arrow indicates the direction of the particles' magnetic moment. Particles are rotated at a speed of 180 rpm.

particles rotate in a fluid on the surface of the substrate. Because of the viscosity of the solution and the friction on the surface, particles can not rotate too fast.

4.5. Array of Magnetic Traps

In this section, we discuss how a micro-electromagnet can be used to assemble magnetic particles into a periodic structure. Figure 4.11 shows (a) micrograph of a micro-electromagnet that produces an array of periodic magnetic field peaks, (b) a computed magnetic field magnitude produced by the device shown in (a), and (c) and (d) demonstration of the device to assemble magnetic particles into periodic structures. The micro-electromagnet consists of two serpentine pattern wires stacked up perpendicular to each other separated by an insulating layer and another insulating layer on top. For a matrix shown in Fig. 4.3(b), each wire is individually connected to a current supply and carries a different amount of current. For the device shown in Fig. 4.11(a), the same amount of current flows through each layer of serpentine array because all the wires in a same layer are connected.

The magnitude of magnetic fields produced by the device near the surface can be expressed as

$$|B| \propto 1 + Sin(\frac{\pi x}{a}) \cdot Sin(\frac{\pi y}{a}),$$

where a is the center-to-center spacing between adjacent wires. The resulting potential has alternating maxima and minima that resemble a shape of an egg carton: three-dimensional plot of magnetic field magnitude is shown in Fig. 4.11(b). The spacing

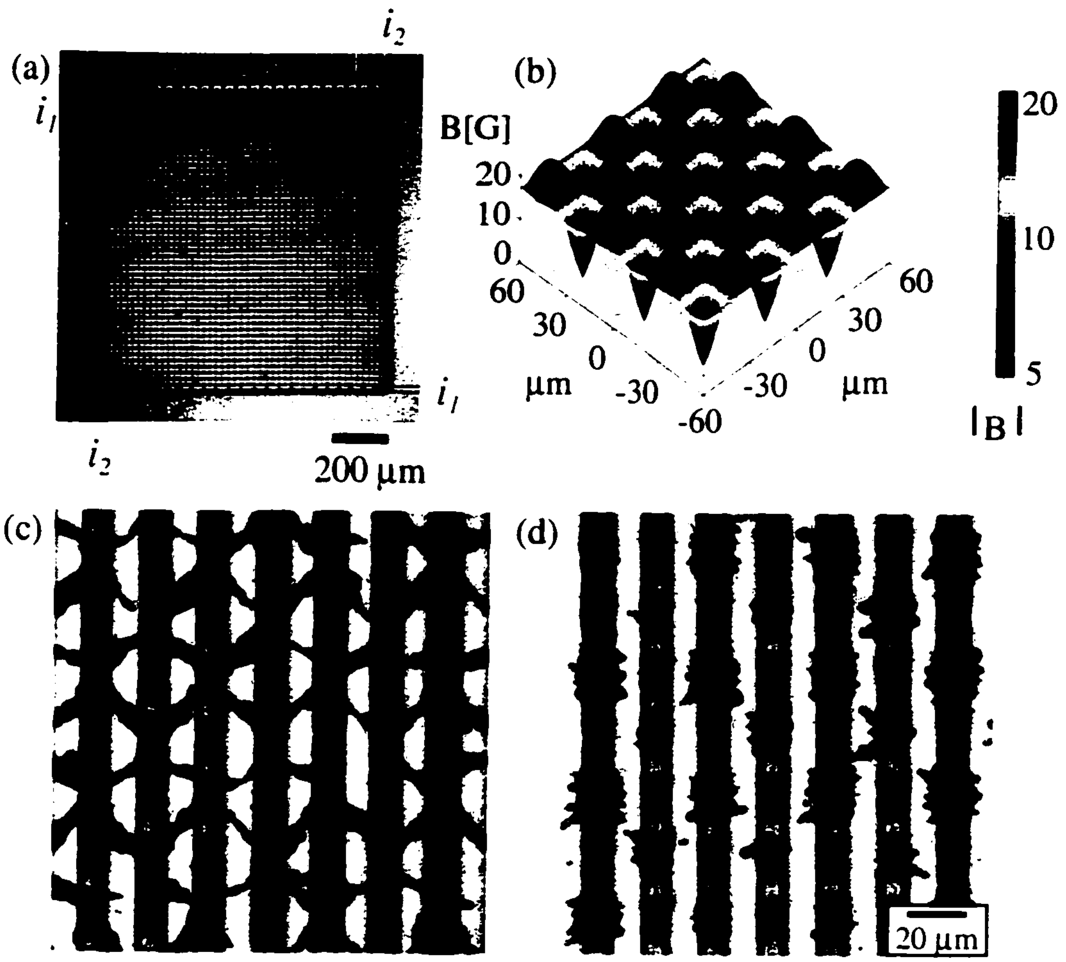

Figure 4.11. (a) Schematic of a micro-electromagnet that produces an array of periodic magnetic field peaks. It consists of two serpentine pattern wires stacked up perpendicular to each other separated by an insulating layer with another insulating layer on top. Each wire has a width of 10 µm, height of 3 µm, and center to center spacing between wires is 20 µm. (b) Computed magnetic field profile produced by the device for $i_1 = i_2 = 0.1$ A. $B_{max} = 20$ G with $\nabla B = 1$ G/µm is produced as a result. (c) Demonstration of trapping iron particles. Iron particles are connected in chain and form a diagonally connected diamond shaped array due to aggregation. (d) Demonstration of trapping magnetic microspheres. Periodic array of magnetic particle dots are formed, where the position of particles agree well with the computed magnetic field profile shown in (b).

between two nearest maxima (or minima) is $\sqrt{2}a$. With the spacing between wires of 20 μm and $i_1 = i_2 = 0.1$ A, $B_{max} = 20$ G with $\nabla B = 1$ G/μm is produced on each peak.

Two types of magnetic particles are shown to form periodic arrays using this device and they are shown in Figs. 4.11(c) and 4.11(d). Figure 4.11(c) shows iron particles that were used in the rotation of magnetic particle demonstration, and Fig. 4.11(d) shows magnetic microspheres that were used in the trapping and moving demonstration. From the calculation, magnetic particles are expected to form an array of dots at each peak magnetic field positions. However, iron particles do not form an array of dots, but they are assembled to form a diagonally connected diamond shaped array as shown in Fig. 4.11(c). This is because iron particles become small magnets connecting each other in chain causing aggregation between them. These chains are formed through saddle points between field maxima. For magnetic microspheres, magnetic interactions between particles are negligible because they are encapsulated in a thick polymer; hence aggregation between particles is prevented. Figure 4.11(d) shows how magnetic microspheres are assembled to form a periodic array of dots.

4.6. Summary

In conclusion, we have designed, fabricated and demonstrated various multi-layer micro-electromagnets for controlling and manipulating magnetic nanoparticles. In particular, the micro-electromagnet matrix is a versatile device, which can create complex static or dynamic magnetic field profiles for many experimental purposes. Most importantly, a matrix can produce single or multiple magnetic field peak(s) at any positions above the surface and independently move them continuously with spatial resolution much less than the spacing between wires. Using a matrix, we have demonstrated the trapping of particles at desired location, the continuous motion of particles in two dimensions, the simultaneous motion and joining of two separate groups of particles into one group. A matrix also rotated magnetic particles above a fixed position utilizing time dependent current control. To control and manipulate semiconductor nanocrystals, microelectrode arrays could produce electric field peaks that interact with the particle's induced electric dipole moment, or micro-electromagnets can be used to manipulate them by attaching semiconductor nanocrystals to magnetic nanoparticles.

Chapter 5

MANIPULATION OF MAGNETOTACTIC BACTERIA

We have demonstrated the ability of micro-electromagnets to trap, move and assemble magnetically tagged biological systems. As an example, we report the basic manipulation to trap and move magnetotactic bacteria using micro-electromagnets in this Chapter. Two types of micro-electromagnets, a ring trap and a matrix used to demonstrate magnetic particle manipulation in Chapter 4, are used to control the location of magnetotactic bacteria in microscopic scale.

Micro-electromagnets produce high magnetic fields ($B \sim 0.1$ T) and high field gradients ($\nabla B \sim 10^4$ T/m) to precisely control and manipulate magnetic objects in a fluid at room temperature. The versatility of micro-electromagnets comes from the fact that it can manipulate magnetic objects or objects with magnetic particles attached, without physical barriers or channels. A virtual barrier produced by a current carrying micro-electromagnet matrix can change its shape with precise control.

In this Chapter, we discuss the possibilities of manipulating biological systems in section 5.1. We then describe magnetotactic bacteria in section 5.2, and the operating principle of micro-electromagnets in section 5.3. Demonstrations of magnetotactic bacteria manipulation are shown in section 5.4.

5.1. Manipulation of Biological Systems

Micro-electromagnets, first developed in our group [Drndic M. *et al.*, 1998], have played important roles in manipulating both cold neutral atoms (Chapter 3) and magnetic nanoparticles (Chapter 4). The ability to move magnetic particles can lead to a new technology where biological systems can be freely controlled and manipulated, and the applications may extend to both biological and biomedical sciences. Controlled experiments with biological systems including cells, microorganisms, DNA and proteins may be carried out by inserting or attaching magnetic particles to those entities. Furthermore, the experiments can be automated and miniaturized, realizing "micro-Total Analysis systems"(μ-TAS) on a single chip [*Micro Total Analysis Systems*, 1994 & 1998].

As a way of manipulating biological systems, optical tweezers have been used to trap and manipulate small particles [Ashkin A. *et al.*, 1986], bacteria and viruses [Ashkin A. and Dziedzic J.M., 1987], and cells [Ashkin A. *et al.*, 1987]. Mechanical properties of DNA attached to a magnetic bead have been studied using magnetic tweezers experimental setup [Haber C. and Wirtz D., 2000]. Magnetic field gradient produced by magnetic tweezers allow controlling the magnetic bead motion. DNA was studied by monitoring the motion of the bead. Because the magnetic field is produced by large permanent magnets in magnetic tweezers, individual control of several DNA in parallel is not possible.

The use of micro-electromagnets may open a new way of assembling biological systems, including macromolecules and DNA, into artificial structures. By producing a sharp magnetic field peak with high field gradient, the ring trap can trap and position magnetically tagged biological samples suspended in a fluid. The matrix can move these samples continuously over its surface with submicron spatial resolution, enabling controlled experiments in a microscopically confined region. By combining micro- or nano fabrication techniques with chemistry, where magnetic particles can be attached to many biological or non-biological objects, biological systems including cells and DNA may be controlled and manipulated. For example, it may be possible to manipulate and study large number of DNA simultaneously by magnetic field peaks produced by a micro-electromagnet matrix.

5.2. Magnetotactic Bacteria

Magnetotactic bacteria, first discovered in 1975 [Blakemore R., 1975], grow single domain ferromagnetic magnetosomes inside the body, which consists of nanometer sized membrane bound crystals of magnetite (Fe_3O_4) particles [Schuler D., 1999]. Because they are either microaerophilic or anaerobic, they use magnetosomes to avoid high oxygen levels and their navigation along the geomagnetic field lines facilitates migration to their favored position in the oxygen gradient [Frankel R.B. *et al.*, 1994]. These magnetic chains passively align to the direction of the magnetic field and the bacteria swim along the field lines.

When magnetosomes are arranged in a single chain, as in magnetospirillum species, magnetostatic interactions between the single magnetic domain particles cause the particle magnetic moments to orient spontaneously parallel to each other along the chain direction. The magnetic moment is then large enough (~ $10^9\ \mu_B$) to be oriented along the geomagnetic field at ambient temperature [Schuler D. *et al.*, 1999].

Magnetotactic bacteria have many biotechnological applications, where the applications involve either living bacteria or isolated magnetosome particles extracted from bacteria [Schuler D. *et al.*, 1999]. One of the possible applications using our micro-electromagnets is to micro-manipulate these magnetotactic bacteria to study how they behave and interact in a microscopic region by assembling them in a controlled way.

An example of magnetotactic bacteria is shown in Fig. 5.1. Figure 5.1(a) shows a TEM image of a whole body, where it is few microns long and few hundred nanometers wide. The close up TEM image of magnetotosom is shown in Fig. 5.1(b). Particles are connected in one-dimensional chain, where each particle is about 100 nm in size. The schematic shown in Fig. 5.1(c) illustrates how bacteria navigate along the geomagnetic field lines in order to avoid oxygen rich region. In the northern hemisphere, geomagnetic field lines point downward at an angle and these bacteria aligned to this field lines also point downward. By moving along this field line, they move to deeper part of the water, where there is less oxygen. In the southern hemisphere, the geomagnetic field lines point upward at an angle and these bacteria still move downward; they are "south seeking". Because geomagnetic field lines point parallel to the surface near the equator, both kinds of bacteria, north seeking and south seeking, are found. For this reason, magnetotactic bacteria are found in deeper part of the lake or pond, not on the surface.

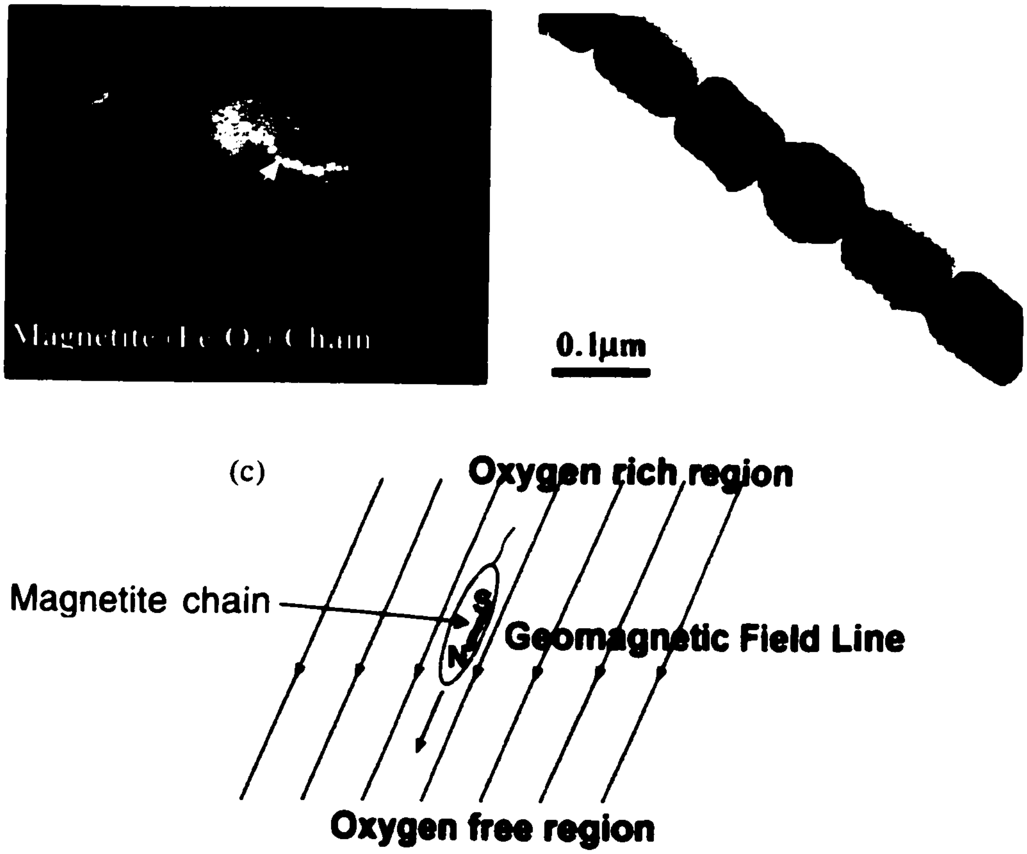

Figure 5.1. (a) TEM image of magnetotactic bacteria. The bacteria are a few microns long and a few hundred nanometers wide. They grow a chain of magnetic particles inside body, where the close up of the chain is shown in (b). (c) Schematic of how bacteria navigate. Because magnetotactic bacteria are either microaerophilic or anaerobic, they use magnetosomes to avoid high oxygen levels. Their navigation along the geomagnetic field lines facilitates migration to their favored position in the oxygen gradient.

5.3. Operating Principle

Magnetotactic bacteria were manipulated using two types of micro-electromagnets: a ring trap [Fig. 2.4(a)] and a matrix [Fig. 2.4(c)]. The fabrication steps for making these devices were described in detail in section 2.2. In this section, we discuss the operating principle of magnetotactic bacteria manipulation by micro-electromagnets.

Micro-electromagnets produce local peaks in the field magnitude that can attract and control the location of magnetotactic bacteria on a two-dimensional surface. Because of magnetic chains that these bacteria possess in their bodies, bacteria align themselves in the field direction produced by a micro-electromagnet and swim along the field lines towards the position of the peak in the field magnitude. As discussed in section 4.3, the matrix produces single or multiple peak(s) in field magnitude simultaneously at any position above the surface and moves the peak position(s) independently from each other. Because each wire in a matrix can carry a different current, many magnetic field profiles can be created. Consequently, using a matrix, a group or groups of magnetotactic bacteria can be trapped in one or multiple position(s), and they can be moved around above a two-dimensional surface.

We can calculate the torque and the force exerted on magnetotactic bacteria by micro-electromagnets. The interaction potential energy between a micro-electromagnet and a bacteria is $U = -mB$, where m is the bacteria's magnetic moment and B is the magnitude of the field, when bacteria is aligned to the field direction. The torque exerted on the bacteria due to the field is $\vec{\tau} = \vec{m} \times \vec{B}$. The magnetic force on the bacteria due to the field is $\vec{F} = m\nabla B$. The magnetic moment for a typical magnetotactic bacteria is m = 1.6 x 10^{-15} Am^2 [Rosenblatt C. *et. al.*, 1982]. For micro-electromagnets we have constructed, current densities up to 4 x 10^7 A/cm^2 in continuous current mode have been demonstrated at room temperature. This yields magnetic fields up to $B \cong 10$ mT with field gradients as large as $\nabla B \cong 5$ mT/μm with current micro-electromagnets. Using these values, the maximum torque exerted on a bacteria, i.e., when the bacteria is oriented at 90° to the field direction, is τ = 1.6 x 10^{-15} Nm, and the force exerted on a bacteria due to the field gradient is F = 8 x 10^{-10} N. Because the field magnitude B scales with the characteristic size d of the wire as $B \propto I/d$, gradients of the field magnitude as $\nabla B \propto I/d^2$, where I is the wire current, larger gradient, hence larger force on a bacteria can be produced for smaller devices.

5.4. Demonstration of Bacteria Manipulation

Experiments to trap and move magnetotactic bacteria using micro-electromagnets were carried out using an experimental setup shown in Fig. 5.2. A drop of fluid containing magnetotactic bacteria[1] is dispensed on a micro-electromagnet, which is mounted on a copper plate. The copper plate is cooled to about T = 5 °C using a Peltier cooler to remove heat generated by the device. Current is supplied to a ring trap via commercially available power supply and to a matrix from a group of 14 bipolar current sources. Bipolar current supplies were built in our group. For the ring trap and the

---

[1] [1] Magnetotactic bacteria were purchased from American Type Culture Collection (ATCC). They are magnetospirillum bacteria, ATCC # 31632. P.O. Box 1549, Manassas, VA 20108. Tel: 800-638-6597. http://atcc.org.

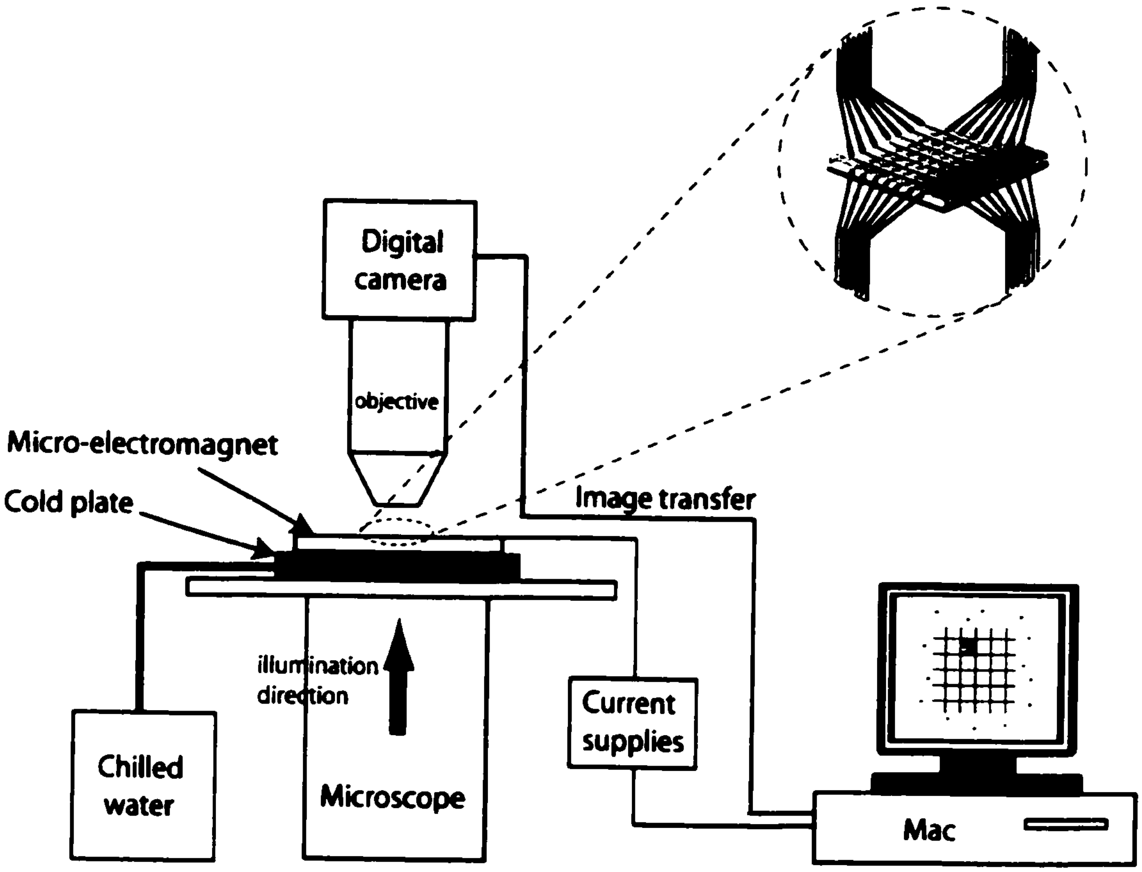

Figure 5.2. Schematic diagram of the experimental setup. A drop of fluid containing magnetotactic bacteria is dispensed on a micro-electromagnet. A matrix is shown in the schematic. The micro-electromagnet is mounted on a copper plate, which is cooled to about $T = 5$ °C using a Peltier cooler to remove heat generated by the device. Chilled water runs through the Peltier cooler to remove heat generated by the Peltier cooler. Current is supplied to a ring trap via commercially available power supply and to a matrix from a group of 14 bipolar current sources. Computer controls the current amount on each wire. Commercially available optical microscope equipped with a digital camera (Nikon Coolpix 850) is used to observe the motion of magnetotactic bacteria on the micro-electromagnets.

channel, current < 0.15 A was applied. For the matrix, currents < 0.1 A were applied to wires in the top layer and currents < 0.2 A for the bottom layer. Higher amount of currents are need for the bottom layer to compensate for the longer distance to the surface. Magnetic field peak of < 1.5 mT for a ring tap and < 4 mT for a matrix are produced under these conditions. Commercially available optical microscope equipped with a digital camera (Nikon Coolpix 850) was used to observe the motion of magnetotactic bacteria on the micro-electromagnets.

Figure 5.3 shows the operation of a ring trap and a channel to trap magnetotactic bacteria. Figure 5.3(a) shows the magnetotactic bacteria on a ring trap when there is no current flowing through the device. They are randomly distributed without magnetic field as expected. With the current of 150 mA applied to the trap, bacteria swim into the center of the device and they get localized as shown in Fig. 5.3(b). The cartoon illustrates the motion of the magnetotactic bacteria in the presence of localized magnetic field. Bacteria are observed to line up in the direction of the magnetic field lines. Above or near the wire, bacteria lie on the surface in the direction perpendicular to the wire as the field lines point in the direction perpendicular to the wire. Inside the circular wire, bacteria are observed in the form of small dots because thy are lined up in the direction of the magnetic field lines, which go into the surface.

Figure 5.3(c) shows a channel that consists of two straight wires with an insulating layer on top. For this wire configuration, magnetic field magnitude is the strongest between the wires when equal amount of currents flow in opposite directions. Without magnetic fields, bacteria are randomly positioned [Fig. 5.3(c)], but they are assembled to form one-dimensional chain in the middle of the channel as soon as the

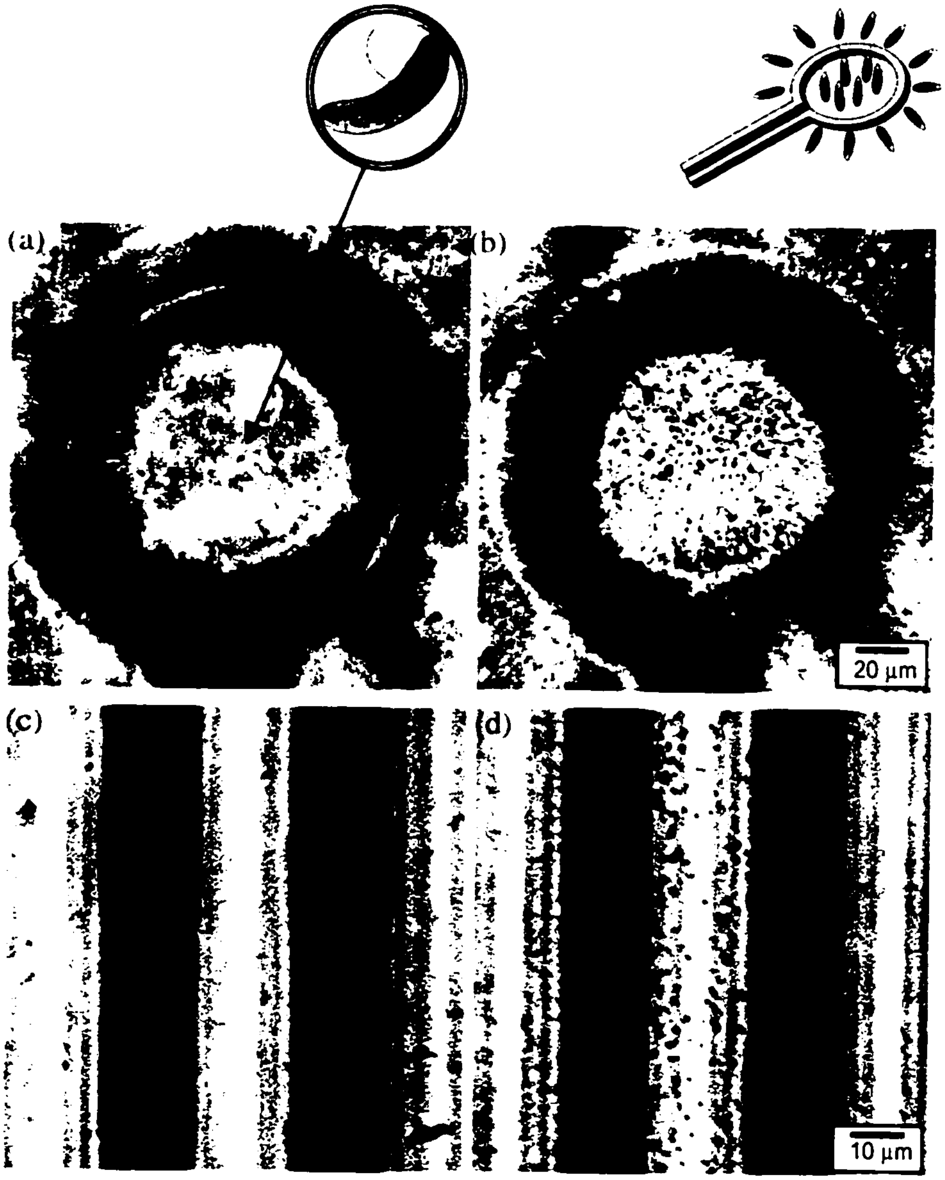

Figure 5.3. (a) A ring trap with no current. Magnetotactic bacteria in fluid are dispensed on the trap. (b) A ring trap with $I = 150$ mA. Magnetotactic bacteria swim into the direction of the field and concentrated on the center of the trap. (c) A channel with no current. (d) A channel with $I = 150$ mA. Bacteria are concentrated in narrow channel forming a one-dimensional chain of these bacteria along the channel.

field is turned on [Fig. 5.3(d)]. For both devices, the density of bacteria is clearly bigger with the field on.

Figure 5.4 shows the operation of a matrix to move a group of magnetotactic bacteria continuously from one position to another over two-dimensional surface. The same kind of bacteria above is used for this demonstration. Without magnetic fields, bacteria are randomly distributed (not pictured in the figure). When a magnetic field peak with $B = 2$ mT is produced at the top on the second column from the left on a matrix, a group of bacteria swim into the region and get localized, shown in Fig. 5.4(a). By changing the current distribution on a matrix, the field peak is moved gradually from the top of the figure to the bottom. Magnetotactic bacteria smoothly follow the field peak and moves down with it, shown in Figs. 5.4(a) to 5.4(e). The motion of the bacteria is not affected by the Joule heating of the device and the manipulation process can continue until the solution dries out, which we observed to be more than 10 to 20 minutes; hence the effect of heating on the biological samples is negligible. The amount of power produced by the matrix on the region (20 μm x 20 μm) that bacteria are concentrated when trapped is 100 μW, which corresponds to power per unit area of 0.25 $\mu W/\mu m^2$.

Although a matrix can move magnetic objects continuously over distances much smaller than the wire spacing, this ability was not tested, because bacteria were illuminated from below in the optical microscope setup we have; bacteria are not observable when they are located right above the wire. Figure 5.4(f) shows the overlay of the full path that bacteria take during the operation. These figures demonstrate that a matrix can locate and move biological objects in any position in two dimensions, an

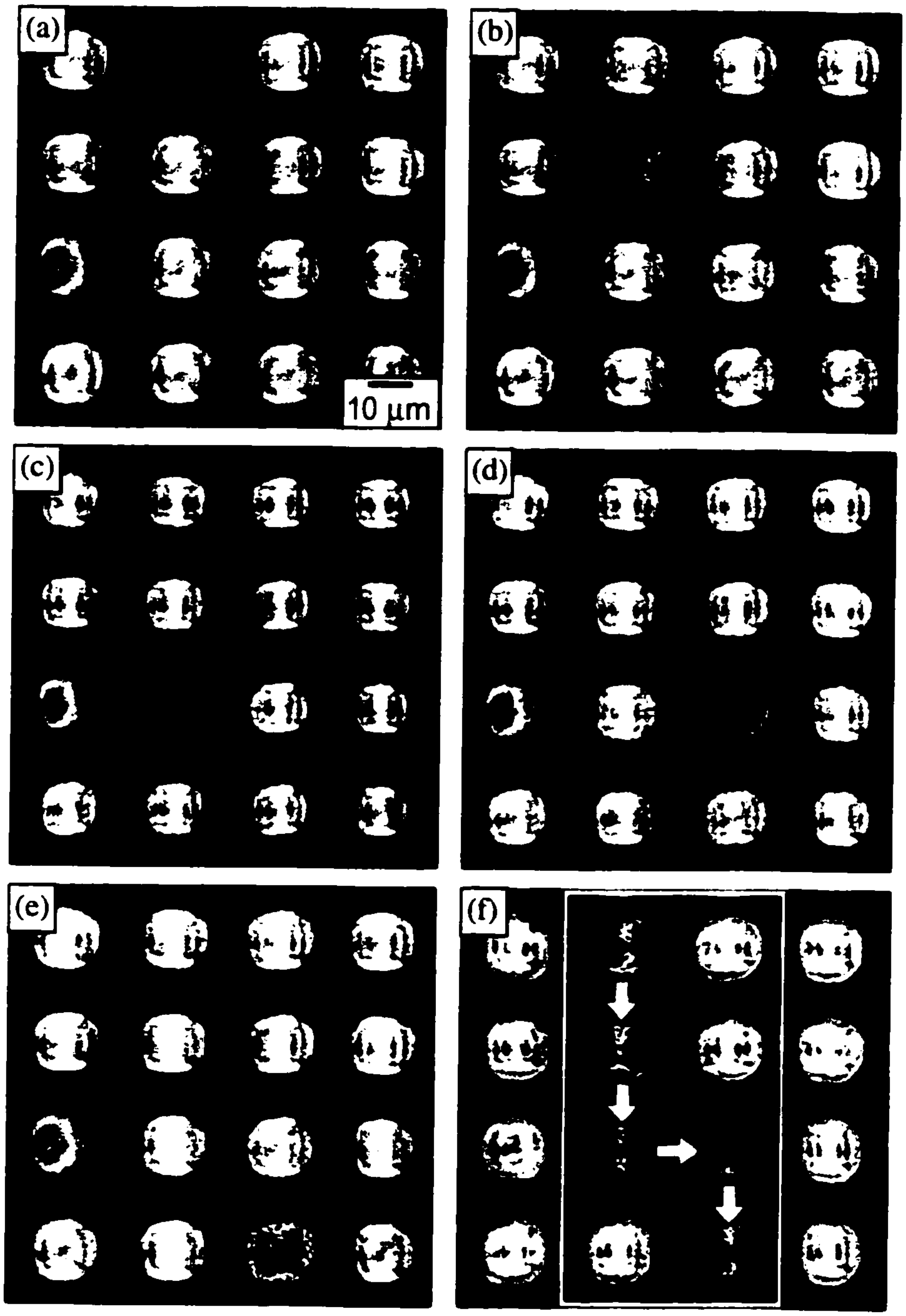

Figure 5.4. Demonstration of trapping and moving magnetotactic bacteria using a matrix. Single magnetic field peak is produced to trap a group of bacteria and then the location of the peak is slowly moved to change the location of bacteria. As a result, bacteria follow the field peak and moves down.

ability that can be used to manipulate biological systems and study interactions between them.

5.5. Summary

In summary, we have demonstrated the capability of micro-electromagnets to manipulate biological systems. As an example, we have demonstrated the manipulation of magnetotactic bacteria using micro-electromagnets. Using a ring trap and a channel, we have confined magnetotactic bacteria in one location or in a linear chain. Using a matrix, we have demonstrated the trapping of bacteria at any desired location and the continuous motion of bacteria in two dimensions. The versatility of matrix comes from the fact that it can manipulate magnetic objects without physical barriers or channels, because a virtual magnetic field barrier produced by a matrix can change its shape quickly with precise control.

Chapter 6

MANIPULATION OF SINGLE MAGNETIC NANOPARTICLES

In this Chapter, we discuss how we can use our micro-electromagnets to control the location of single magnetic nanoparticles in a fluid above a substrate. Submicron sized electromagnets are designed and fabricated for the purpose of manipulating single magnetic nanoparticles above a two-dimensional surface. Micro-electromagnets demonstrated in Chapters 4 & 5 had wire size of 10 μm. Micro-electromagnets discussed in this Chapter have wire size less than 1 μm. This experiment is currently being carried out in collaboration with Prof. Moungi Bawendi's group in MIT. Co nanoparticles are synthesized and characterized by one of his students, Joseph B. Tracy. The fabrication of the devices and the experiments to demonstrate particle manipulation are performed in our group.

We first give the overview of various nanoscale particles, especially Co nanoparticles in section 6.1. The fabricated nano-electromagnets are shown and described in section 6.2. Calculations will be shown in section 6.3 to determine the minimum size Co nanoparticles that can be trapped using a micro-electromagnet. Experimental setup and some preliminary observations will be shown in sections 6.4 and 6.5 respectively.

6.1. Introduction

Advanced techniques in the synthesis and growth of nanoscale particles in fluids have created many interests to study and control these nanoparticles. Nanoscale particles synthesized in solution include magnetic nanoparticles such as Co, magnetic nanowires such as Ni, and semiconductor crystals such as CdSe. Due to its small volume, typically few nm in diameter, CdSe crystals exhibit quantum dot like properties at room temperature [Brus L.E. 1991]. Magnetic Ni nanowires with the dimension of ~ 100 nm in diameter by ~ 100 μm in length can be easily grown by electroplating through nanopores in solution [Whitney T.M. *et al.*, 1993]. The Co nanoparticles display wealth of size dependent magnetic, electronic and catalytic properties, and they may be used for magnetic storage purposes.

Micro-electromagnets produce local magnetic field peaks in small regions and they may be used to control the location of these Co nanoparticles and Ni nanowires. With the precise control of Co nanoparticles and magnetic nanowires with a micro-electromagnet matrix, assembly of these nano objects into nano circuitry may be realized, which yields custom built magnetic nanoparticle structures.

In this Chapter, we focus our attention on Co nanoparticles. The Co nanoparticles have been synthesized in solution with excellent control [Puntes V.F. *et al.*, 2001] with sphere- and rod- shaped Co nanoparticles grown monodisperse as shown in Fig. 6.1. Figure 6.1 shows the TEM image of Co nanoparticles synthesized by Prof. Bawendi's group in MIT [personal communication]. The size of spherical Co particles can range

Figure 6.1. TEM image of Co nanoparticles by the courtesy of Prof. Bawendi's group in MIT. Both spherical and rod shaped particles are synthesized at the same time. They are superparamagnetic at room temperature. External magnetic field was applied to align these particles in one direction before the solution was dried.

from few nm to ~ 20 nm, where rod shaped particles can be synthesized to be as long as few hundred nm with few nm in diameter.

The Co nanoparticles are magnetic and they orient in the direction of the magnetic field when external magnetic field is applied. Because they are in nm range in size, they have single domain, i.e., all the atomic magnetic spins of the particles are coupled in the same direction, and the particle behaves as a single magnetic dipole. A Co nanoparticle can possess either superparamagnetic or ferromagnetic properties depending on its size, anisotropy and the ambient temperature. The relation between anisotropy energy and thermal energy given by $KV = k_B T$ determines the transition between the superparamagnetic and ferromagnetic regimes [Dorman J.L. *et al.*, 1997], where K is the anisotropy constant and V is the volume of the particle. An average magnetic moment of superparamagnetic particle is zero as the magnetic moment of the particle rotates freely due to the thermal energy. A ferromagnetic particle, on the other hand, has a permanent magnetic moment in a fixed orientation. The spherical Co nanoparticles shown in Fig. 6.1 have diameter of approximately 10 nm, making them superparamagnetic at room temperature. For spherical Co nanoparticles, superparamagnetic to ferromagnetic transitions occur when the diameter of the particle becomes larger than 12 nm at room temperature.

Because these particles are too small to be observed using an optical microscope or scanning electron microscope (SEM), Co nanoparticles are usually observed using transmission electron microscope (TEM). Particles are placed on a small TEM grid and dried out before being mounted inside the TEM. The TEM images of these particles are used for characterization of the particles, i.e., to study the size distribution and to monitor the quality of the particles.

For the experiment that we are currently working on, we are interested in observing the motion of Co nanoparticles in fluids in real time. Once particles are dried out, particles are stuck on the substrate and they do not move, making it impossible to manipulate them using micro-electromagnets. In order to observe the motion of these particles in fluids in real time, dye molecules are attached to the functionalized surface of Co nanoparticles by Bawendi's group. Laser fluorescence microscope has been built in our group to monitor the motion of dye molecules that are attached to Co nanoparticles, as will be discussed later.

6.2. Multi-layer Nano-Electromagnets

To control the location of single magnetic nanoparticles with nanometer spatial resolution, much finer micro-electromagnets are designed and fabricated. Figure 6.2 shows micrographs of multi-layer nano-electromagnets fabricated using e-beam lithography: array of single ring traps [Fig. 6.2(a)], double ring traps [Fig. 6.2(b)], and a matrix [Fig. 6.2(c)]. Fabrication procedures for these devices were described in detail in section 2.4. The images were photographed by Nikon Coolpix 850 digital camera under optical microscope because SEM did not yield good images because of the insulating layers on the devices. Figure 6.2(a) shows three ring traps connected in series, each with different radius and wire width. These ring traps have 5 μm, 3 μm and 2 μm in radius

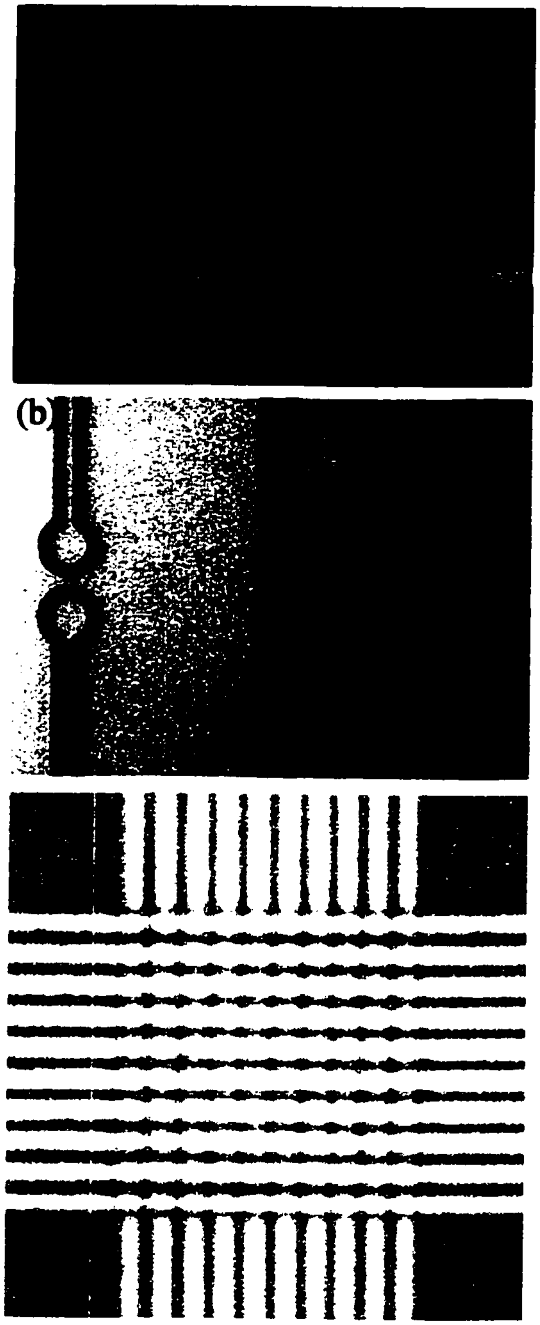

Figure 6.2. (a) Micrograph of fabricated ring traps. They have 5 μm, 3 μm and 2 μm in radius with 1μm, 500 nm and 500 nm in wire width, respectively from left to right. (b) Micrograph of double ring traps. Outer traps have radius of 5 μm and middle trap has radius of 2.5 μm. Each wire has width of 1 μm, height of 150 nm. (c) Micrograph of a fabricated matrix (10x10 wires). Each wire has width of 500 nm, height of 150 nm to 200 nm, and the center-to-center spacing between wires is 1 μm.

with 1μm, 500 nm and 500 nm in wire width, respectively from left to right. Figure 6.2(b) shows three pairs of double ring traps fabricated on a single substrate.

To demonstrate how much field magnitude we can achieve from these small ring traps, we calculate the magnetic field magnitude produced by the ring trap shown on far left. It has radius $r = 2.5$ μm, wire width $w = 1$ μm, wire height $h = 200$ nm, and thickness of insulating layer $t = 2$ μm. With a current $I = 100$ mA, which corresponds to current density $J = 5 \times 10^7$ A/cm^2, a field magnitude $B = 25$ mT at the center above the insulator surface, and $B = 0.1$ T on the surface of the wire can be produced.

Figure 6.2(c) shows a 10 x 10 wire sub-micron matrix, which has wire width $w = 500$ nm, wire height $h = 100$ nm for the first layer and $h = 200$ nm for the second layer, and the center-to-center spacing between adjacent wires of 1 μm. Two layers of wires are separated by a thin insulating layer, SiO_2, which has thickness of 150 nm. An insulating layer on the top has thickness of 200 nm. This matrix has 400 times smaller trapping area compared to the matrix fabricated by optical lithography, which was previously shown in Fig. 2.4(a) and demonstrated in Chapter 4. Using this matrix, a single particle or small number of particles can be controlled with 20 times better spatial resolution.

6.3. Calculations for Co Nanoparticles

As mentioned in section 6.1, Co nanoparticles can become either superparamagnetic or ferromagnetic depending on their size, anisotropy, and the ambient temperature. Once they become ferromagnetic, particles interact strongly due to the dipole-dipole interaction. The interaction energy E_{dd} is given by

$$E_{dd} \propto -\frac{(M_S V_{mcore})^2}{r^3},$$

where M_S is the saturation magnetization of the particle, V_{mcore} is the volume of the magnetic core and r is the center-to-center distance between neighboring particles. If the dipole-dipole interaction energy is bigger than thermal energy of the particle, i.e., $E_{dd} > k_B T$, particles can form a chain or a loop to minimize their magnetostatic energy. This results in the self assembly of magnetic particles without the presence of external magnetic field. For the superparamagnetic particles studied in Chapter 4, a thick polymer layer prevents particles from clumping, and the interactions between particles are small. In this case, the individual control of particles is possible. To avoid aggregation among particles and to control them individually, particles need to be in the superparamagnetic regime.

Figure 6.3 illustrates the magnetic moment of a superparamagnetic particle in the presence of an externally applied magnetic field. Without the magnetic field [Fig.6.3(a)], the direction of the magnetization freely fluctuates due to thermal agitation and the time average of magnetization of the particle is zero, i.e., $< M > = 0$. In the presence of the external magnetic field, the particle's magnetic moment rotates to align in the direction of the field, but fluctuates around it because of the thermal motion. Therefore, the average magnetization $<M>$ in the external magnetic field is given by

$$< M > = \frac{\int \cos\theta M \exp[MVB\cos\theta / k_B T] \sin\theta d\theta d\phi}{\int \exp[MVB\cos\theta / k_B T] \sin\theta d\theta d\phi},$$

(a) No applied B-field

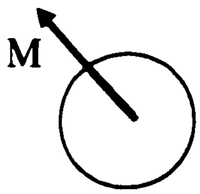

$<M> \ = 0$

(b) With B-field

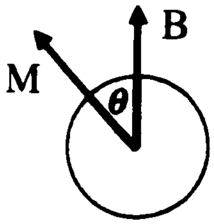

$<M> \ \neq 0$

Figure 6.3. Superparamagnetic particle (a) without external magnetic field. The time average of magnetization of the particle is zero. (b) in the presence of external magnetic field. Particle's magnetization fluctuates around the axis of the field.

where M is the magnetization of the particle, V is the volume of the particle, B is the magnitude of the external magnetic field, and θ is the angle between the external magnetic field and the magnetic moment of the particle. By simplifying the integral, we have found in Chapter 4 that

$$< M > \; = M\left[\coth\left(\frac{MVB}{k_B T}\right) - \frac{k_B T}{MVB}\right].$$

The size of Co nanoparticles that can be manipulated using micro-electromagnets can be estimated. Assuming a particle's magnetic moment as a dipole, magnetic moment, denoted by m, of a particle with single magnetic domain is given by $m = M_S V$. For Co, $M_S = 1.72\ \rho\mu_B$ [*Introduction to Solid State Physics*, 1986], where ρ is the mass density of Co, $\rho = 8900$ kg/m^3, and μ_B is the Bohr magneton. The condition for magnetic particle trapping is that the magnetic interaction energy is stronger than the thermal energy of the particle, i.e.,

$$U = mB = M_S V > k_B T.$$

By substituting $V = (4\pi r^3)/3$ for a spherical particle and $V = \pi r^2 l$ for a rod shaped particle, where r is the radius, and l is the length of the rod shaped particle, a relation can be obtained for the minimum size particle that can be trapped for a given field magnitude. At room temperature ($T = 300$ K), the trapping conditions for Co nanoparticles are:

$$\text{For a sphere with radius r in unit of nm:} \quad r \geq \frac{0.894}{\sqrt[3]{\mathrm{B[T]}}}$$

$$\text{For a rod with diameter(4 nm), length } l\text{:} \quad l \geq \frac{0.239}{\mathrm{B}}$$

For example, the minimum size particle that can be trapped with $B = 10$ mT at room temperature is $r = 4.1$ nm for a spherical particle, and for a rod with 4 nm diameter,

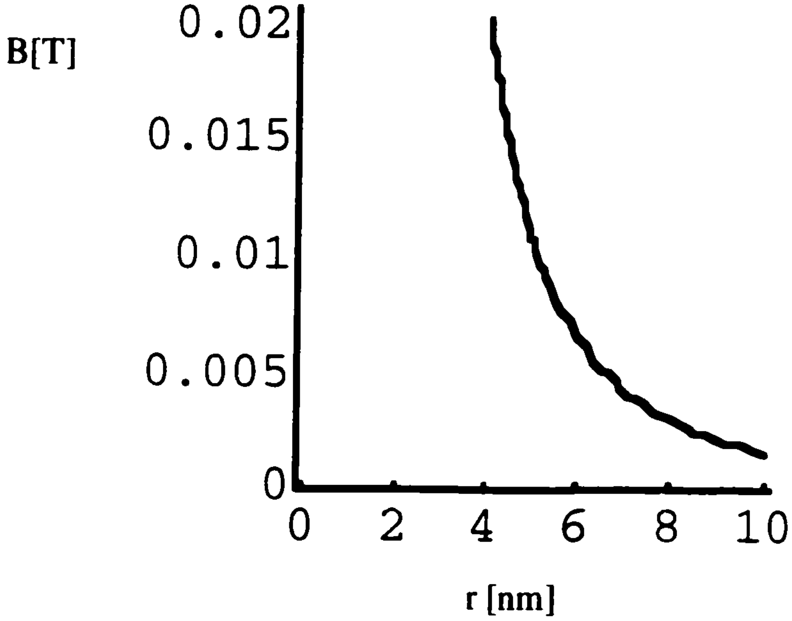

Figure 6.4. A calculated plot of magnetic field magnitude vs. the minimum radius of a spherical Co nanoparticle that can be trapped, assuming the particle is superparamagnetic. For B = 10 mT, a Co nanoparticle with r = 5 nm can be trapped using a micro-electromagnet.

$l = 24$ nm. Because these particles become superparamagnetic at these sizes, we replace M_S with $< M_S >$ and recalculate the minimum size in order to take into account of the thermal effect on the motion of particle's magnetic moment.

The plot in Fig. 6.4 shows the relation between the magnetic field and the minimum size of a spherical superparamagnetic Co particle that can be trapped at room temperature. The plot was calculated assuming that the particle is superparamagnetic. From this plot, we see that a particle with $r = 5$ nm can be trapped for $B = 10$ mT at room temperature. The difference is about 25 % in the size of the radius for the minimum size particle that can be manipulated between calculations assuming the particle is ferromagnetic and superparamagnetic.

6.4. Experimental Setup

In our experiment, dye molecules are attached to Co nanoparticles and observed by a laser fluorescence microscope that we have built. Because dye molecules attached to Co nanoparticles are fluorescent, not Co nanoparticles themselves, the motion of Co nanoparticles is studied by monitoring the motion of dye molecules. A schematic diagram of the experimental setup is shown in Fig. 6.5. Where a conventional optical microscope uses bright white light to illuminate the sample to produce a magnified image of the sample, a laser fluorescence microscope uses a high intensity laser light to illuminate the sample. A laser fluorescence microscope excites the samples with a laser beam and collects the secondary light emanating from the samples. The microscope mainly consists of laser, excitation filter, dichroic (or dichromatic) mirror, emission filter

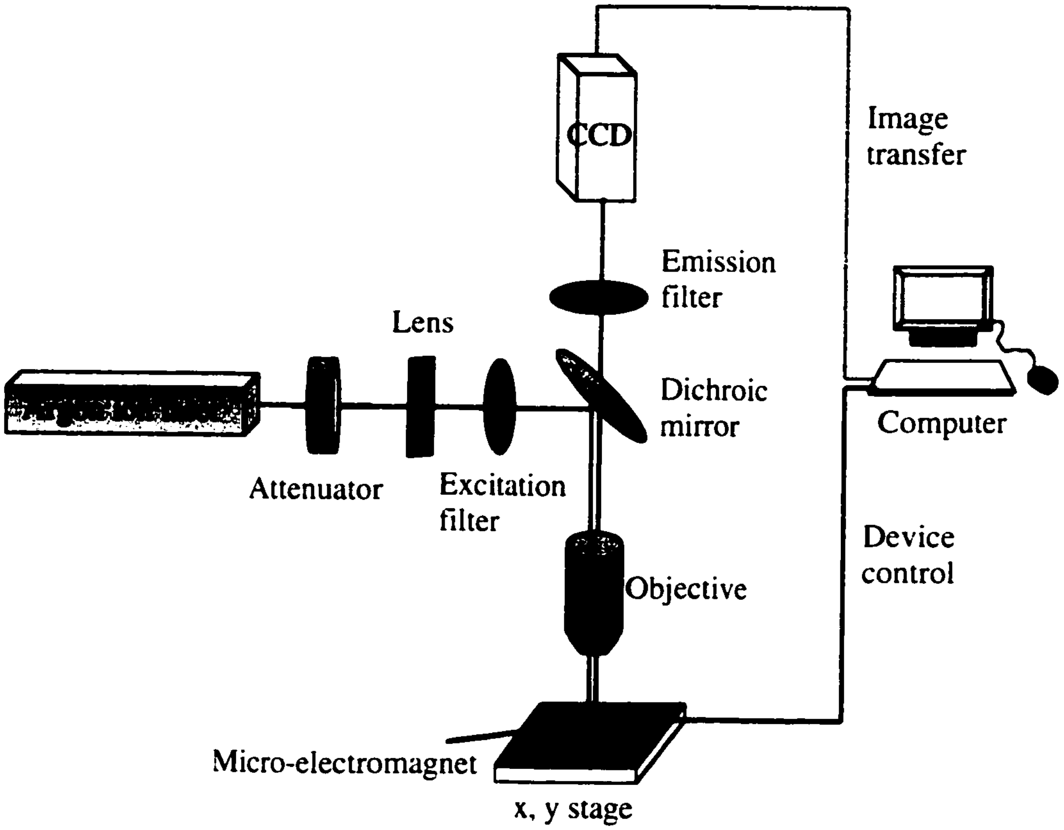

Figure 6.5. A schematic diagram of a laser fluorescence microscope setup. The microscope has three main parts: laser as excitation source, filters and dichroic mirror for separation of wavelengths of light, and charge coupled device (CCD) for imaging. Amount of current on micro-electromagnets is controlled by a computer, which also displays and stores images from CCD.

and imaging unit (charge coupled device). Fluorescent samples are excited by a laser, which then emit secondary light with longer wavelength.

For the excitation source, Air-cooled Argon ion laser[1] from Spectra physics (model 177G) was chosen because of its power (500 mW) and suitable wavelengths. It has three wavelength lines: 458 nm, 488 nm and 514 nm. Any of these lines can be used as excitation source depending on the excitation wavelength of the fluorescent samples.

Crucial parts in the fluorescence microscope are a dichroic mirror and two filters: excitation filter and emission filter. A dichroic mirror has specially coated surface, which can separate the excitation and emission light paths by reflecting the excitation light off the surface while passing the emission light through it. Each dichroic mirror has characteristic wavelength value called the transition wavelength value. The mirror reflects wavelengths of light below the transition wavelength value and transmits wavelengths above it. Ideally, this dichroic mirror would be all that needed to selectively filter the lights. However, because dichroic mirrors are not perfect, unwanted wavelengths of light can pass through the dichroic mirror and make the observation of samples difficult.

For this reason, two filters are used along with the dichroic mirror for precise separation of light. As shown in Fig. 6.5, an excitation filter is placed in the excitation path between the laser and the dichroic mirror and selectively passes through wavelengths of the light that correspond to the excitation wavelengths of the sample. An emission filter is placed between dichroic mirror and eyepiece (or camera) to selectively pass through light emitted from the sample and to block any other wavelengths of light.

---

[1] Laser was purchased from Spectra Physics. It is CW Argon ion laser with three wavelength lines (458, 488 and 514 nm). Spectra Physics, 1335 Terra Bella Avenue, Post Office Box 7013, Mountain View, CA 94039. Tel. 650-961-2550. http://www.spectraphysics.com.

Filters were purchased from Omega Optical[2], where the characteristic wavelengths of each filter are shown in Fig. 6.6. Figure 6.6(a) shows the wavelength characteristics of an excitation filter, model XF 1018. It is a narrow bandpass filter that is centered at 515 nm with ~ 2 nm bandwidth. This filter lets only 514 nm line from the laser to pass through. Figure 6.6(b) shows the wavelength characteristics of a dichroic mirror, model XF 2030. It reflects wavelengths of light between 480 and 500 nm, and transmits wavelengths that are shorter than 480 nm or longer than 500 nm. Figure 6.6(c) shows the wavelength characteristics of an emission filter, model XF 3082. Wavelengths longer than 530 nm are transmitted while anything shorter than 530 nm is reflected.

Images are taken with Roper scientific Coolsnap fx charge coupled device[3] (CCD) digital camera and downloaded to a computer. This CCD has 1300 x 1030 pixels, where each pixel has 6.7 μm^2 area. Its features include fast image readout, 12 bits @ 20 MHz digitization, which yields 94 ms/frame, with low read noise, < 15 e rms @ 20 MHz. It is thermoelectrically cooled down to - 30 °C to reduce the dark noise (noise arising in electronic devices in the absence of light, which is strongly temperature dependent). Dark current for this CCD is 0.01 e/pixel/sec at - 30 °C. We used software called Winspec from Roper scientific to monitor and acquire the images taken by CCD in real time. Figure 6.7 shows the Quantum efficiency of the CCD for different wavelengths. Quantum efficiency measures the efficiency with which incident photons are detected, i.e., Quantum efficiency = Number of detected electrons / Number of incident photons.

---

[2] Omega Optical, Inc. 210 Main Street, Brattleboro, VT 05301. Tel. 866-488-1064. http://www.omegafilters.com

[3] Thermoelectrically cooled Coolsnap fx CCD was purchased from Roper scientific, 3440 East Britannia Drive, Tucson, AZ. 85706. Tel: 520-889-9933, Fax: 609-587-1970. http://www.roperscientific.com

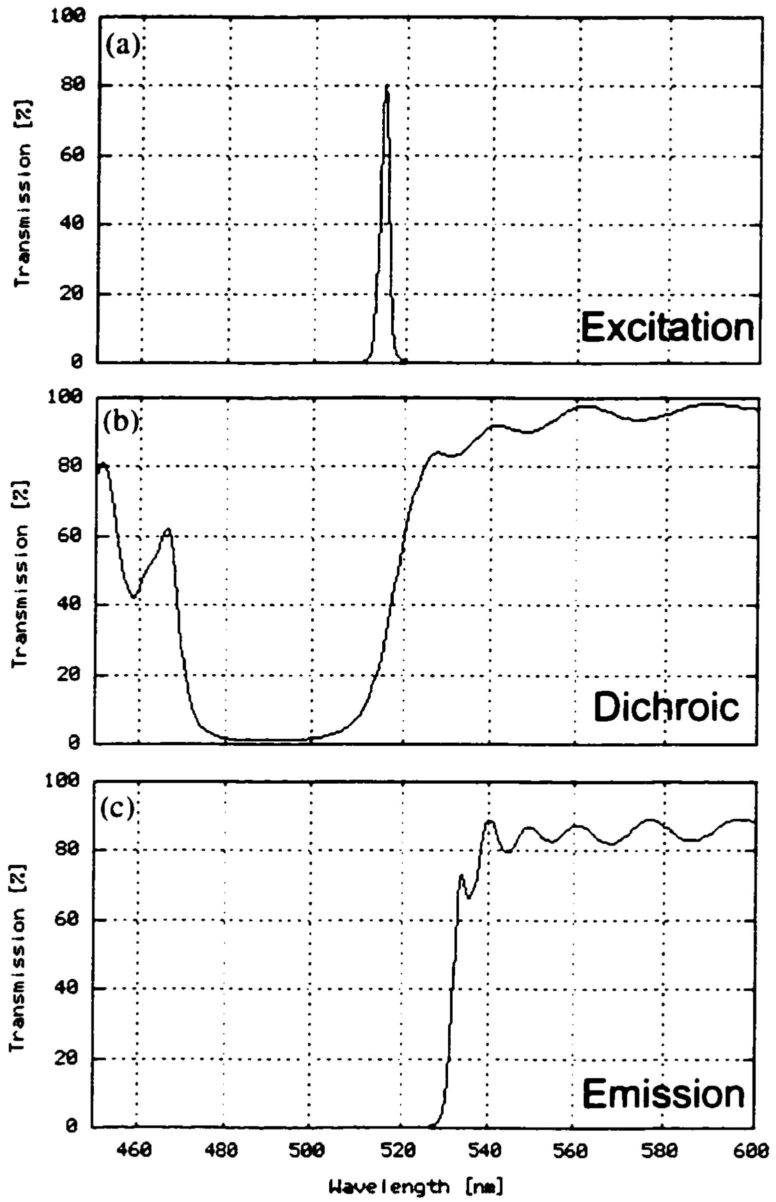

Figure 6.6. Wavelength characteristics of (a) an excitation filter, model XF 1018. It is a narrow bandpass filter that is centered at 515 nm with ~ 2 nm bandwidth. This filter lets only 514 nm line from the laser to pass through. (b) a dichroic mirror, model XF 2030. It reflects wavelengths of light between 480 and 500 nm, and transmits wavelengths that are shorter than 480 nm or longer than 500 nm. (c) an emission filter, model XF 3082. Wavelengths longer than 530 nm are transmitted while anything shorter than 530 nm is reflected. The transmission data are taken from the Omega Optical website.

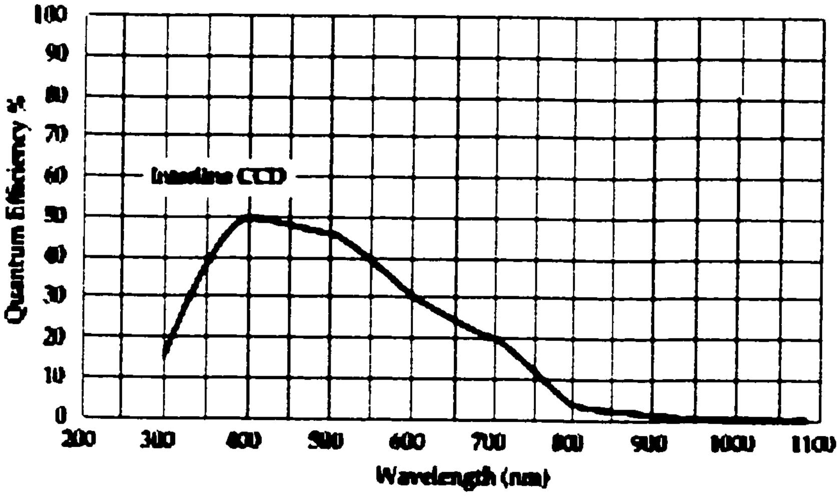

Figure 6.7. Wavelength response of Quantum efficiency of Coolsnap fx CCD from Roper Scientific. Its sensitivity peaks at 400 - 500 nm and decreases for higher wavelengths. Quantum efficiency goes below 10 % for wavelength higher than 750 nm. The graph was taken from specification sheet from Roper scientific.

6.5. Preliminary Observations

We have tested the newly built laser fluorescence microscope by examining fluorescent particles. Note that micro-electromagnets were not used for this observation. For this observation, a drop of solution containing fluorescent particles was dispersed over a sapphire substrate, and a cover slide was placed on the top. The sapphire substrate was placed on the microscope and the images were taken with CCD, which is attached to the microscope. Figure 6.8 shows the optical images for two different particles: 2 μm fluorescent particles [Fig. 6.8(a)], and 5 ~ 10 nm CdSe nanoparticles [Fig. 6.8(b)]. The CdSe nanoparticles were prepared by Prof. Bawendi's group in MIT, and 2 μm fluorescent particles were purchased from Bangs Lab [Product number: FS05F/2920].

As one can see from Fig. 6.8, it is difficult to resolve each particle's location when many particles are close to each other. For example, when two objects are closely located, physically resolvable separation between two objects is given by Rayleigh's resolution criterion

$$D = 0.61\ (\lambda / N.A.),$$

where $N.A.$ is numerical aperture of an objective. The resolution is limited by diffraction. For $\lambda = 530$ nm, with 100 X magnification objective with $N.A. = 0.95$ (dry objective), $D = 340$ nm. Therefore, for this condition, the smallest distance of two particles that can be resolved is 340 nm, which is much larger than the size of Co nanoparticles that we plan to manipulate. However, we can resolve two closely located particles with much better resolution than the diffraction limit shown above. Because the images are the display of intensity (accumulated photons converted to electrons) on each pixel, by fitting

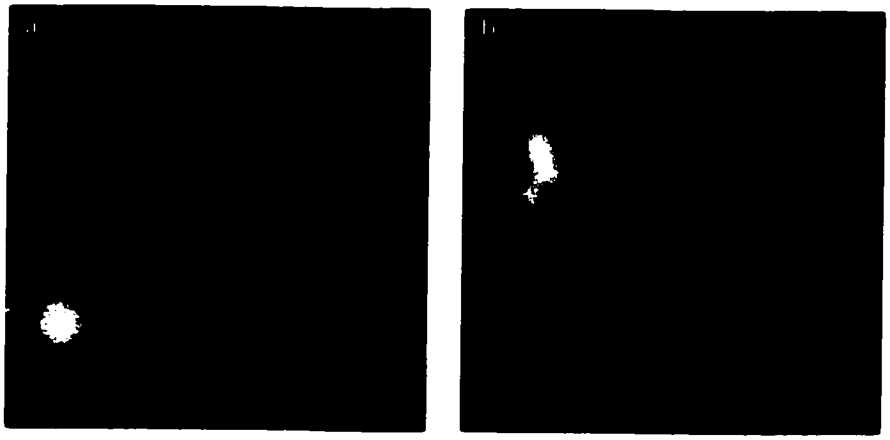

Figure 6.8. Images taken with CCD for (a) 2 μm fluorescent particles via objective with 20 times magnification (b) CdSe nanoparticles via objective with 50 times magnification.

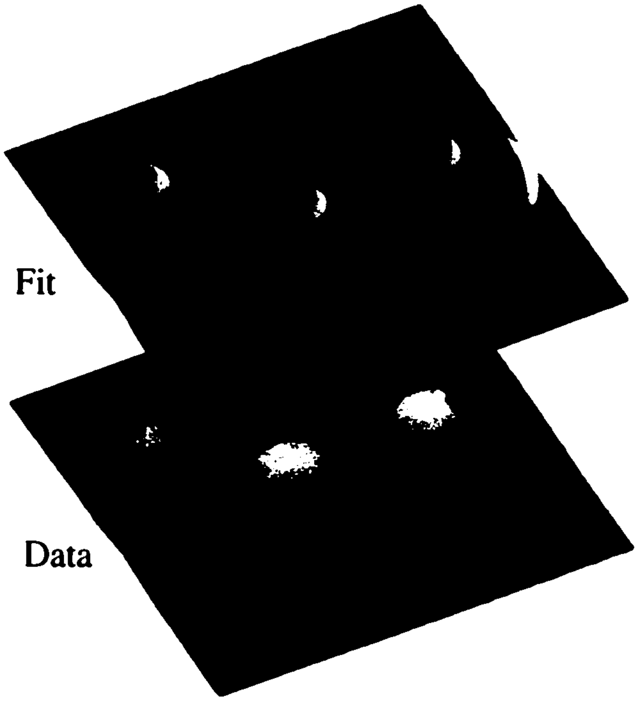

Figure 6.9. Image of 2 μm fluorescent particles and its fit. The location of single particle's peak can be deduced from the fitted data with spatial resolution better than few tens of nm.

the data, we can precisely locate the center on each particle's image. Figure 6.9 shows the overlay of 3D plot of fitted data with the raw image from 2 μm particles. By fitting the data, the peak of single particle can be located with high precision.

6.6. Summary

We are currently developing ways to manipulate Co nanoparticles using sub-micron electromagnets. Calculations show that Co nanoparticles as small as 10 nm in diameter can be manipulated with B = 10 mT at room temperature. The nano-electromagnets have been fabricated and laser fluorescence microscope has been built in our group. Prof. Bawendi's group in MIT has attached dye molecules to Co nanoparticles so that real time observation of these particles can be possible using our laser fluorescence microscope setup.

Chapter 7

CONCLUSIONS AND FUTURE DIRECTIONS

In this Chapter, we summarize the major results described in previous chapters, and present some ideas for future work. The major result of this Thesis is the extended applications of micro-electromagnets [Drndic M. *et al.*, 1998] for the control and manipulation of magnetic nanoparticles and biological systems in a fluid [Lee C.S. *et al.*, 2001], and manipulation of cold neutral atoms in ultra high vacuum [Dekker N.H. *et al.*, 2000]. Micro-electromagnets consist of single or multiple layers of microfabricated current carrying wires on a substrate. They can generate many different magnetic field profiles to reflect, trap and guide atoms as well as to position, move and rotate magnetic particles and magnetotactic bacteria. Manipulation of magnetic objects using micro-electromagnets is based on the magnetic dipole interaction between the particle's magnetic moment and the magnetic field produced by current carrying wires.

In this Thesis, we have described the design, fabrication and properties of micro-electromagnets: a ring trap, a matrix and an array of traps for the manipulation of magnetic nanoparticles in fluids, and a guide for the manipulation of cold neutral atoms in ultra high vacuum. In general, micro-electromagnets used in atom manipulation consist of single layer of wire patterns, and micro-electromagnets used in magnetic particle manipulation consist of multiple layers of wire patterns with the same number of insulating layers to separate the wires and to cover the top.

In Chapter 2, we describe the fabrication, and the electrical and thermal properties of micro-electromagnets. The multi-layer micro-electromagnets used in Chapters 4 and 5 are summarized below with key results from both Chapters.

(1) A ring trap consists of a single circular current-carrying wire with an insulating layer on top. A single magnetic field peak is produced at the center of the circular wire above an insulating layer as current flows through the device. When a current is applied through the device, magnetic particles are immediately pulled in and trapped to the center of the ring trap. Using this device, we have trapped both magnetic microspheres (Chapter 4) and magnetotactic bacteria (Chapter 5).

(2) A micro-electromagnet matrix can trap, move and rotate magnetic nanoparticles by producing sharp magnetic field peaks in magnitude that can easily change their positions on a two-dimensional surface. A matrix consists of two layers of current-carrying Au wires, separated by an insulating layer, with an additional insulating layer on top. A matrix is a versatile device and it can operate in many different modes. The first thing it can do is to generate single magnetic field peak at any position above the surface and to move its peak from one position to another with a spatial resolution much less than the spacing between two adjacent wires. A matrix can produce two or multiple peaks simultaneously and move their peak positions independently from each other. By applying AC currents through the matrix, it can rotate magnetic particles on the surface of a substrate. Using a matrix, we have demonstrated to trap and move a group or groups of magnetic microspheres (Chapter 4) and magnetotactic bacteria (Chapter 5). We have also rotated iron particles on a surface using a matrix (Chapter 4). The versatility of matrix comes from the fact that it can manipulate magnetic objects

without physical barriers or channels because a virtual magnetic field barrier produced by a matrix can change its shape fast with precise control.

(3) An array of magnetic traps can be produced to assemble magnetic particles into a periodic structure. An array of traps consists of two serpentine pattern wires stacked up perpendicular to each other separated by an insulating layer and another insulating layer on top. Unlike a matrix, where each wire is individually connected to a current supply and carries a different amount of current, for an array of traps, the same amount of current flows through each layer of serpentine array because all the wires in a same layer are connected. The resulting potential has alternating maxima and minima that resemble a shape of an egg carton. Two types of magnetic particles were shown to form periodic arrays using this device: magnetic microspheres and iron particles (Chapter 4).

In Chapter 3, we describe the design and magnetic field calculations for a micro-electromagnet atom guide, and present an experimental demonstration of guiding atoms [Dekker N.H. *et al.*, 2000]. A micro-electromagnet atom guide consists of an array of current carrying wires, which produces a region of magnetic field minimum, where weak field seeking atoms can be guided above the surface of a substrate. Using a micro-electromagnet atom guide, we experimentally demonstrate the guiding of atoms. We have also fabricated a nano-electromagnet guide/interferometer/beam splitter, all in one device by utilizing time dependent feature of the device. By changing the current distribution, we show in magnetic field simulations that the path of atoms can be precisely controlled.

In Chapter 4, we describe the design and magnetic field calculations for multi-layer micro-electromagnets including a ring trap and a matrix, and experimentally demonstrate the ability of micro-electromagnets to trap, move and rotate magnetic particles in fluids [Lee C.S. *et al.*, 2001].

In Chapter 5, we describe how multi-layer micro-electromagnets may be used to manipulate biological systems such as cells and DNA. As an example, we demonstrate to trap and move magnetotactic bacteria with microscopic spatial resolution.

In Chapter 6, we propose the use of multi-layer nano-electromagnets for the control and manipulation of single Co nanoparticles and Ni nanowires. The ultimate goal is by precisely controlling Co nanoparticles and magnetic nanowires with a micro-electromagnet matrix, to assemble these nano objects into nano circuitry, and to build custom designed magnetic nanoparticle structures. This experiment is being carried out in collaboration with Prof. Moungi Bawendi's group in MIT. Micro-electromagnets produce local magnetic field peaks in a small region and they may be used to control the location of Co nanoparticles and Ni nanowires.

Multi-layer micro-electromagnets can be used to manipulate cells or DNA. Hakho Lee is currently working on manipulating DNA using micro-electromagnets. Unlike magnetic tweezers, which use macroscopic magnets to manipulate the magnetic bead that is attached to a strand of DNA, micro-electromagnets can produce microscopic magnetic field peaks to precisely control the location of magnetic beads. In order to manipulate DNA using micro-electromagnets, DNA samples are prepared by attaching magnetic beads to both ends of a DNA strand. Using a matrix, two magnetic particles attached to DNA are initially trapped to two field peaks, and by moving the positions of these peaks, magnetic particles may be moved around on a two dimensional surface. By stretching and bending the DNA, mechanical properties of DNA may be studied. Even though there are several experimental issues to be surmounted in order to carry out these experiments, I find these works to be exciting future directions.

Appendices

A.1. Raith 150 (Basement) Procedure

1. Load samples (10 min.)
2. From Project, open file.
3. Open SEM Control panel and set the parameters. Aperture = 30 μm
4. After loading, Signal A to TV
5. User position to Faraday cup
6. Beam ON & SEM to INTERNAL
7. Signal A to SE2
8. EHT ON (If it doesn't turn on, then go to Tool and Airlock)
9. From control panel Detectors, Auto BC = BC, then back to OFF
   (For Mouse, Middle: Focusing, Left: Magnification)
10. Focus around the Faraday cup
11. Apertures: Focus Wobble and aperture align
12. Press GUN ALIGN
13. Go to inside Faraday cup and Mag = 1000K
14. From Window 4, measure Beam current and record.
15. Go to sample (change to TV and beam OFF first)
16. User position: Clip 2
17. Beam On & Signal A= SE2
18. Find the edge and set the origin: Adjust UV (0,0) Adjust
19. Find the second position and press READ.
20. Angle correction. Red changes to Green
21. Find silver paint & focus
22. Find a small silver paint and open FILE: New positionlist
23. Open FILTER: Match Writefield
24. Set U, V: 10 μm, 25 % and press Create & Scan Marks
25. Next, Set U,V: 1 μm, 35 % and press Create & Scan Marks

26. Ready to write!
27. Set Expose parameters : Stepsize: 20 to 50 nm, Set Beam current and Dosage, then calculate Dwell time.
28. Open FILE: New positionlist
29. Open Structure: Load DXF and bring in the file to work on
30. To turnoff: EHT OFF then UNLOAD (10 min.)

A.2. New Thermal Evaporator (Basement) Procedure

1. Close high vacuum valve if open.
2. Vent the chamber.
3. Lift up the chamber. It takes few minutes.
4. After the chamber is open, stop venting.
5. Install samples on a sample holder provided and metals (Au, Cr, Pt, etc) to evaporate.
6. Lift down and close the chamber.
7. Turn on roughing pump.
8. When the pressure reaches less than 200 mTorr, turn off the roughing pump, and open the high vacuum valve.
9. Wait till the pressure in vacuum chamber drops to 2 ~ 4 x 10^{-7} Torr. It takes about 30 minutes.
10. While pumping down, set the parameters for the metals to evaporate. Parameters include density, z-ratio, final thickness of the metal, and tooling factor.
11. When the pressure reaches 2 ~ 4 x 10^{-7} Torr, it is time to evaporate.
12. Select a metal to evaporate. Turn on the power supply for the metal evaporation and slowly increase the current (turn a knob clockwise) while monitoring the x-tal monitor. Stop when the desired rate is reached (typically 1 Å /s for Cr, and 2 ~ 3 Å /s for Au).
13. Open the shutter after evaporating ~ 70 Å of metal.

14. The monitor will reset itself and start counting the thickness of metal that has been evaporated.
15. When the desired thickness is reached as set before, the shutter closes itself.
16. Decrease the current, turn off the power supply and choose other metal to evaporate and repeat steps from 11 – 14.
17. When the evaporation is done, wait for about 3 minutes for samples to cool down.
18. Turn off the high vacuum valve.
19. Vent the chamber.
20. Lift up the chamber.
21. Unload samples and take out the metals.
22. Close the chamber.
23. Stop venting.
24. Turn on the roughing pump.
25. Turn off the roughing pump when the pressure reaches ~ 200 mTorr.
26. Turn on high vacuum valve.
27. In about a minute, turn off high vacuum valve.

A.3. New E-beam Evaporator (2nd floor) Procedure

1. Turn on roughing pump.
2. Close high vacuum valve. Hear a loud 'click' sound.
3. Turn on mechanical pump; make sure cooling water is on.
4. Vent; turn on two valves; turn on regulator.
5. When the pressure reaches 1 atm., the door pops open automatically.
6. Install metals/crucibles into e-beam hearth; mark on position lever.
7. Install substrate in holder.
    a. Mount substrate to holder with clips.
    b. Places holder on top of chamber.
    c. Turn on shutter actuator to cover substrate.
8. Pump down chamber

  a. Close regulator, start roughing pump for several seconds, close vent valves and then pump down to <200 mtorr.
  b. Close roughing pump and turn on high vacuum pump.
  c. Turn on emission gauge, degas about 1 minutes when the pressure drops to 10-6 torr.
  d. Turn on high voltage and filament power.
  e. Wait for about 1~2 hours to pump down to 5 10^-7 torr before evaporation

9. Set up x-tal monitor
  a. Change the density and Z-ratio to the specified values of the target metals.
  b. Hit the zero button to remove offset.
10. Evaporate
  a. Turn off emission; turn on AC/DC sweep control.
  b. Turn up filament and high voltage; slowly adjust the voltage to 8 kV.
  c. Turn up the filament current to reach the desired rate.
  d. Let it warm up a bit to get a smooth deposition going.(~100A on X-tal monitor)
  e. Turn shutter actuator to uncover substrate.
  f. When desired thickness is reached, turn shutter actuator to cover substrate, turn down current, turn down voltage and turn off filament, high voltage and filament power supply.

     DON'T turn off the high voltage power supply.
  g. Wait for e-beam hearth to cool down.(~5 min)
11. Close high vacuum valve; vent.
12. Unload substrate and the target material.
13. Close vent; pump down.
14. Turn off high voltage power supply.
15. Turn off mechanical pump.

References

Adams C.S., Sigel M., and Mlynek J. (1994), Phys. Rep. **240**, 143, and references therein.

Alivisatos A.P., general review, (1996), J. Phys. Chem. **100**, 13226.

Ashkin A., Dziedzic J.M., Bjorkholm J.E., Chu S., (1986), Optics Letters, **11**, 288.

Ashkin A., Dziedzic J.M., (1987), Science, **235**, 1517.

Ashkin A., Dziedzic J.M., Yamane T., (1987), Nature, **330**, 769.

Barbic M., Mock J.J., Gray A.P., Schultz S., (2001), Appl. Phys. Lett. **79**, 1399.

Bergeman T.H., McNicholl P., Kyacia J., Metcalf H., Balaz N.L., (1989), J. Opt. Soc. Am. B **6**, 2249.

Blakemore R., Science, (1975), **190**, 377.

Brus L.E., Appl. Phys. A., (1991), **53**, 465, and references therein.

Cassettari D., Chenet, A., Folman, R., Hasse, A., Hessmo, B., Kruger, P., Maier, T., Schneider, S., Calarco, T., Schmiedmayer, (2000), J., Appl. Phys. B **70**, 721.

Cognet L., Savalli V., Featonby P., Westbrook N., Westbrool C., Helmerson K., Phillips W.D., Zabow G., Drndic M., Lee C.S., Westervelt R.M., Prentiss M. (1999), Europhys. Lett. 47 (5), 538.

Dalibard J., Cohen-Tannoudji C., (1989), J. Opt. Soc. Am. B **6**, 2023.

Dekker N.H., Lee C.S., Lorent V., Thywissen J.H., Smith S.P., Drndic M., Westervelt R.M., Prentiss M. (2000), Phys. Rev. Lett. **84**, 1124.

Deng T., Whitesides G.M., Radhakrishnan M., Zabow G, and Prentiss M., (2001), Appl. Phys. Lett. **78**, 1775.

Denschlag J., Cassettari D., Chenet A., Schneider S., Schmiedmayer J., (1999), Appl. Phys. B. **69**, 291.

Dinega D.P., and Bawendi M.G., (1999), Angew. Chem. Int. Ed. **38**, 1788.

Dorman J.L., Fiorani D, Tronc E., (1997) Adv. Chem. Phys. **98**, 283.

Drndic M. (2000), PhD Thesis, Harvard University.

Drndic M., Johnson K.S., Thywissen J.H., Westervelt R.M., Prentiss M. (1998), Appl. Phys. Lett. **72**, 2906.

Drndic M., Lee C.S., and Westervelt R.M., (2001), Phys Rev. B. **63**, 085321.

Drndic M., Zabow G., Lee C.S., Thywissen J.H., Johnson K.S., Prentiss M., Westervelt R.M., Featonby P.D., Savalli V., Cognet L., Helmerson K., Westbrook N., Westbrook C. I., Phillips W.D., Aspect A., (1999) Phys. Rev. A. **60** (5).

Fabry B., Maksym G.N., Butler J.P., Glogauer M., Navajas D., Fredberg J.J., (2001), Phys. Rev. Lett. **87**, 148102.

Folman R., Krüger P., Cassettari D., Hessmo B., Maier T., Schmiedmayer J. (1999), quant-ph/9912106.

Frankel R.B., Bazylinski D.A., Hyperfine Interact. (1994), **90**, 135.

Fortagh J., Grossmann A., Zimmermann C., Hansch T.W., (1998), Phys. Rev. Lett. **81**, 5310.

Haber C., and Wirtz D., (2000), Rev. Sci. Inst., **71**, 4561.

Hansel W., Hommelhoff P., Hansch T.W., Reichel J., (2001), Nature, **413**, 498.

Hinds E.A., Vale C.J., Boshier M.G., (2001), Phys. Rev. Lett. **86**, 1462.

Hinds E.A., Hughes I.G., Review article, (1999), J. Phys. D: Appl. Phys. **32**, R119.

Introduction to solid sate physics, 2nd edition, (1986), Kittel C., John Wiley & Sons, Inc.

Johnson K.S., Drndic M., Thywissen J.H., Zabow G., Westervelt R.M., Prentiss M. (1998), Phys. Rev. Lett. **81**, 1137.

Kim J.A., Lee K.I., Nha H., Noh H.R., Jhe W., (1997), J. Korean Phys. Soc. **30**, 387

Klimov V.I., Mikhailovsky A.A., Su Xu, Malko A., Hollingsworth J.A., Leatherdale C.A., Eisler H.-J., and Bawendi M.G., (2000), Science, **290**, 314.

Krauss T.D., and Brus L.E., (1999), Phys. Rev. Lett. **83**, 4840.

Lee C.S., Lee H., Westervelt R.M., (2001), Appl. Phys. Lett. **79**, 3308.

Metcalf H., van der Straten P. (1994), Phys. Rep. **244**, 203.

Micro Total Analysis Systems, (1994), A. van den Berg, P. Bergveld, eds., Kluwer, Dortrecht, the Netherlands.

Micro Total Analysis Systems '98, (1998), D. J. Harrison, A. van den Berg, eds., Kluwer, Dortrecht.

Mueller D., Anderson D.Z., Grow R.J., Schwindt P.D.D., Cornell E.A. (1999), Phys. Rev. Lett. **83**, 5194.

Mueller D., Cornell E.A., Prevedelli M., Schwindt P.D.D., Anderson D.Z. (2000), physics/0003091.

Ott H., Fortagh J., Schlotterbeck G., Grossmann A., Zimmermann C., (2001), Phys. Rev. Lett. **87**, 230401.

Physics for Scientists and Engineers, (1990), Serway R.A., Saunders College Publishing.

Puntes V.F., Krishnan K.M., Alivisatos., Science (2001) **291**, 2115.

Reichel J., Hansell W., Hansch T.W. (1999), Phys. Rev. Lett. **83**, 3398.

Roach T.M., Abele H., Boshier M.G., Grossman H.L., Zetie K.P. and Hinds E.A. (1995), Phys. Rev. Lett. **75**, 629.

Rosenblatt C., Flavio F., Torres de Araujo, Frankel R. B., (1982), Biophys. J. **40**, 83.

Schuler D., Frankel R.B., Appl. Microbiol. Biotechnol. (1999) **52**, 464.

Schuler D., J. Molec. Microbiol. Biotechnol. (1999) **1**, 79.

Sidorov A.I., McLean R.J., Rowlands W.J., Lau D.C., Murphy J.E., Walkiewicz M., Opat G.I., and P. Hannaford P. (1996), Quant. Semiclass. Opt. **8**, 713.

Smith S.B., Finzi L., Bustamante C., (1992), Science, **258**, 1122.

Strick T.R., Allemand J.F., Bensimon D., Croquette V., (1998), Biophysical Journal, **74**, 2016.

Sukumar C.V., Brink D.M., (1997), Phys. Rev. A. **56**, 2451.

The Feynman Letures on Physics, Vo. 2, (1966), Feynman R.P., Leighton R.B., Sands M., Addison-Wesley publishing company.

Thywissen J.H., Olshanii M., Zabow G., Drndic M., Johnson K.S., Westervelt R.M., Prentiss M. (1999a), Eur. J. Phys. D **7** (3), 361.

Thywissen J.H., Westervelt R.M., Prentiss M. (1999b), Phys. Rev. Lett. **83**, 3762.

Van Wees B.J., Van Houten H., Beenakker C.W.J., Williamson J.G., Kouwenhoven L.P., Van der Marel D., Foxon C.T., (1988), Phys. Rev. Lett. **60**, 848.

Weinstein J.D. and Libbrecht K.G. (1995), Phys. Rev. A **52** (5), 4004.

Whitney T.M., Jiang J.S., Searson P.C., Chien C.L., (1993), Science, **261**, 1316.

Zabow G., Drndic M., Thywissen J.H., Johnson K.S., Westervelt R.M., Prentiss M. (1999), Eur. Phys. J. D **7**(3), 351.